UNIVERSITY OF OKLAHOMA

GRADUATE COLLEGE

NOVEL PHENOMENA IN CONFINED ELECTRONIC SYSTEMS

A DISSERTATION

SUBMITTED TO THE GRADUATE FACULTY

in partial fulfillment of the requirements for the

Degree of

DOCTOR OF PHILOSOPHY

By

BAHMAN ROOSTAEI

Norman, Oklahoma

2007

Downloaded from SHAREOK. Persistent Handle URL: https://hdl.handle.net/11244/1281

UMI Number: 3291240

Copyright 2007 by
Roostaei, Bahman

All rights reserved.



UMI Microform 3291240
Copyright 2008 by ProQuest Information and Learning Company.
All rights reserved. This microform edition is protected against
unauthorized copying under Title 17, United States Code.

ProQuest Information and Learning Company
300 North Zeeb Road
P.O. Box 1346
Ann Arbor, MI 48106-1346

NOVEL PHENOMENA IN CONFINED ELECTRONIC SYSTEMS

A DISSERTATION APPROVED FOR THE
HOMER L. DODGE DEPARTMENT OF PHYSICS AND ASTRONOMY

BY

Prof. Kieran J. Mullen

Prof. Michael Morrison

Prof. Matthew Johnson

Prof. Bruce Mason

Prof. Patrick J. McCann

©Copyright by BAHMAN ROOSTAEI 2007
All Rights Reserved.

To my late father who always believed in me
and to my mother who I truly love.

Acknowledgements

I am grateful to my advisor Prof. Kieran Mullen for all his support. I learned more science and scientific thinking during my years with Kieran than rest of my life. Kieran, not only was my advisor but generously supported me to connect to the scientific community and taught me how to do that. I was also very lucky to have the constant collaboration and support of Prof. Herbert A. Fertig from Indiana University without whom this research work would have been incomplete. I would also like to thank Prof. René Côté and Jérôme Bourassa from University of Sherbrook, Canada for their collaboration throughout this work. I also wish to thank Kavli Institute for Theoretical Physics at University of California, Santa Barbara (KITP) where part of this research work was performed through their Graduate Fellowship. Finally I acknowledge US National Science Foundation for their financial support.

Contents

iii

Acknowledgements **iv**

List Of Tables **vii**

List Of Figures **viii**

Abstract **xvi**

1 Introduction **1**

2 Two Dimensional Electron Gas Under Strong Magnetic Field **6**
2.1 Overview of Integer Quantum Hall Effect 6
2.1.1 Integer Quantum Hall Edge States 11
2.1.2 Percolation 13
2.2 Quantum Hall Ferromagnets 14
2.2.1 Coulomb Exchange 15
2.2.2 Charge-Spin Entanglement 16
2.2.3 The Effective Action 20
2.2.4 Topological Spin Excitations 22
2.2.5 Detecting Skyrmions 28
2.2.6 Skyrmion Dynamics 28
2.2.7 Skyrme Lattice 33

3 Double Layer Quantum Hall Systems **36**
3.1 Quantum Coherence in Bilayer Quantum Hall Systems 36
3.2 Bilayer Effective Action 42
3.3 Pseudo-spin Topological Excitations 44
3.4 Microscopic Calculation of Texture Lattices 46
3.5 Numerical Results 55
3.6 Spin Investigations in Bilayers 62
3.6.1 NMR Experiment 62
3.6.2 Parallel Magnetic Field 65
3.7 CP3 Skyrmions 68
3.7.1 Numerical Results 71

3.7.2 Effect of interlayer bias 77

4 Activated Transport in Bilayer Systems **83**
4.1 Introduction 83
4.2 Excitonic Superfluid 84
4.3 Role of Disorder 88
4.4 Chern-Simon Theory for Quantum Hall Systems 91
4.5 Dynamics of Merons in Bilayer System 95
4.6 Model of Activation Barrier For Merons 100
4.7 Future Work 105
4.8 Meron-Edge Theory, An Alternative? 105

5 Nanoring Arrays **111**
5.1 Phase Coherence 112
5.2 Model of Interacting Rings 114
5.3 Classical Charges 115
5.4 Quantum Charges 118
5.5 Hartree Approximation 119
5.6 Monte Carlo simulation 120
5.7 Finite size scaling of the 1+1D system 124
5.8 Universality Class 125
5.9 Effect of Magnetic Flux 130
5.10 Two Dimensional Array 134

6 Conclusion **137**
6.1 Spin in bilayer quantum Hall systems 137
6.2 Activated dissipation in bilayer quantum Hall systems 140
6.3 Nano-ring arrays 141

List Of Tables

3.1 Comparison between two representations of a bimeron. 46

4.1 Electrostatic charge of each type of meron in units of e. ν_U, ν_L are the upper and lower filling factors respectively. s and p are vorticity and dipole moment respectively. 97

List Of Figures

2.1 Integer and fractional quantum Hall effect: Hall(transverse) and longitudinal resistance v.s. magnetic field. The numbers indicate the filling factor of the Landau levels. After ref.[51] 7
2.2 Schematic profile of band structure at the junction of GaAs-AlGaAs. 8
2.3 Schematic picture of a Hall bar experiment. The magnetic field is perpendicular to the plane and the contacts are made to edges of the bar. 9
2.4 Illustration of a smooth confining potential varying in the x direction. The horizontal dashed line indicates the equilibrium Fermi level. Electrons head into the page on the left edge state and out of the page on the right. The magnetic field is perpendicular to the lines. 12
2.5 Contour map of a smooth disorder landscape. close lines indicate valleys. The yellow filled areas are the increasing sea level whole shore lines finally percolate from one end of the system to the other end. . . 14
2.6 Schematic diagram of Landau level splitting due to Zeeman coupling in (a) vacuum (b) in GaAs host. 15
2.7 Illustration of magnetic translation and phase factor. When an electron travels around a parallelogram (generated by $\tau_q\tau_k\tau_{-q}\tau_{-k}$) perpendicular to the magnetic field it picks up a phase $\phi = 2\pi\phi/\phi_0 = q \times k$. 17
2.8 The spin of electrons in a skyrmion gradually rotate from the minority direction at the center to the majority direction at the boundaries. Unlike a U(1) vortex, a skyrmion does not have any singularity at the center. Figure taken from [22] 23
2.9 Illustration of insertion of an imaginary flux tube into QH state. . . . 24
2.10 Energy of a skyrmion and anti-skyrmion compared to single spin flip energy v.s. g-factor (Zeeman coupling). After ref.[24]. 27
2.11 NMR Knight shift measurement of the electron spin polarization near filling factor $\nu = 1$. Circles are data of Barret *et. al.*[28]. the dashed line is just connecting the circles. The solid line is the prediction for polarization of non-interacting electron gas. 29
2.12 NMR nuclear spin relaxation rate $1/T_1$ v.s. filling factor. After Tyco *et. al.* [30] 29

3.1 Schematic representation of the heterostructure containing the double quantum well (DQW) where the electron bilayers are confined. 36

3.2 Typical tunneling conductance observed in 2D-2D tunneling experiments when quantum wells are balanced, at various temperatures and zero magnetic field. The inset shows the quantum well band diagrams. After [43]. 38
3.3 Tunneling current v.s. interlayer voltage for three different samples with three tunneling strengths at B=8 T and T=0.6 K. Zero bias suppression is due to gapped excitations of the 2D electron fluid. After [46] 39
3.4 Tunneling conductance v.s. interlayer voltage at $\nu_T = 1$ at T=40 mK for four different total densities N_T (in units of 10^10cm^{-2}) and thus three different layer separation d/ℓ. The first three in the left column show regular Coulomb gap behavior while the one in the right column shows a zero bias resonance. After [49]. 39
3.5 A schematic diagram of an ideal double quantum well. The first two eigenstates are symmetric and antisymmetric. 40
3.6 Splitting of the Landau levels for $\Delta_{SAS} < \Delta_Z$. 41
3.7 Four typical convergence factors for the last 50 iteration for densities of a meron-meron lattice at $d/\ell = 0.8$ and zero tunneling. 54
3.8 Contour plot of a bimeron at interlayer separation $d/\ell = 0$(The SU(2) symmetry of the Coulomb potential is not yet broken) and zero tunneling at $\nu_T = 1.02$. The contour labels are values of density in units of $1/2\pi\ell^2$ 54
3.9 (a) In-plane components of a bimeron in (S,A) basis at $\nu_T = 1.02$, zero tunneling and zero layer separation. The length of the vectors is proportional to the magnitude of $|\rho_{SA}|$ at each point. (b)Z-component of the same bimeron in (S,A) basis: $\rho_{SS} - \rho_{AA}$ in units of $1/2\pi\ell^2$. The colors do not have a physical interpretation. 56
3.10 (a)In-plane components of the pseudo-spin of a bimeron in (U,L) basis at $\nu_T = 1.02$, zero tunneling and zero layer separation. The length of the vectors is proportional to the magnitude of $|\rho_{UL}|$ at each point. The plot shows the two merons bound together in this excitation. (b) The In-plane pseudo-spin field (vectors) and Z-component of the same set of vectors(contour). (c) Z-component of the same bimeron in (U,L) basis: $\rho_{UU} - \rho_{LL}$ in units of $1/2\pi\ell^2$. (d) 3D plot of the excess density of the bilayer system due to the same bimeron in units of $1/2\pi\ell^2$. . . 57
3.11 (a) Contour plot of a bimeron charge density at interlayer separation $d/\ell = 0.2$(the SU(2) symmetry of the Coulomb potential is broken) and zero tunneling at $\nu_T = 1.02$. The contour labels are values of density in units of $1/2\pi\ell^2$. (b) In-plane components of the same bimeron. The length of the vectors is proportional to the magnitude of $|\rho_{SA}|$ at each point. 58

3.12 (a) In-plane components of the pseudo-spin of a bimeron in the (U,L) basis at $\nu_T = 1.02$, zero tunneling and $d/\ell = 0.2$. The length of the vectors is proportional to the magnitude of $|\rho_{UL}|$ at each point. (b) The In-plane pseudo-spin field (vectors) and Z-component of the same set of vectors(contour). (c) Z-component of the same bimeron in (U,L) basis: $\rho_{UU} - \rho_{LL}$ in units of $1/2\pi\ell^2$. (d) 3D plot of the excess density of the bilayer system due to the same bimeron in units of $1/2\pi\ell^2$. The colors do not have a physical interpretation. 59
3.13 (a) Contour plot of a bimeron at interlayer separation $d/\ell = 0.8$ and zero tunneling at $\nu_T = 1.02$. The contour labels are values of density in units of $1/2\pi\ell^2$. (b) In-plane components of the same bimeron. The length of the vectors is proportional to the magnitude of $|\rho_{SA}|$ at each point. 60
3.14 (a)In-plane components of the pseudo-spin of a bimeron in (U,L) basis at $\nu_T = 1.02$, zero tunneling and layer separation $d/\ell = 0.8$. The length of the vectors is proportional to the magnitude of $|\rho_{UL}|$ at each point. (b)The In-plane pseudo-spin field (vectors) and Z-component of the same set of vectors(contour). (c) Z-component of the same bimeron in (U,L) basis: $\rho_{UU} - \rho_{LL}$ in units of $1/2\pi\ell^2$. (d) 3D plot of the excess density of the bilayer system due to the same bimeron in units of $1/2\pi\ell^2$. 61
3.15 Hartree-Fock energy per electron for two different lattice states v.s. total filling factor of the bilayer system at zero tunneling. 62
3.16 (a)In-plane components of pseudo-spin vectors of a meron lattice in (U,L) basis at $\nu_T = 1.02$, layer separation $d/\ell = 0.8$ and zero tunneling. The length of the vectors is proportional to the magnitude of $|\rho_{UL}|$ at each point. (b) Z-component of the same meron lattice state in (U,L) basis: $\rho_{UU} - \rho_{LL}$ in units of $1/2\pi\ell^2$. (c) 3D plot of the excess density of the bilayer system due to the same meron lattice in units of $1/2\pi\ell^2$. 63
3.17 (a) Resistively detected NMR. Solid dots: Equilibrium longitudinal resistance Rxx near $\nu_T = 1$. Open dots: Fractional change in R_{xx} in response to ^{71}Ga NMR pulses. Solid lines are guides to the eye. (b) NMR T_1 relaxation time vs inverse filling factor. (c) T_1 v.s. d/ℓ at $\nu_T = 1$. All data at T=35 mK. After [50]. 64
3.18 The energy gap as a function of tilt angle in a weakly tunneling bilayer sample $\Delta_{SAS} = 0.8K$. The solid circles are for $\nu_T = 1$. The triangles for $\nu_T = 2/3$. The dashed line is the predicted behavior of $\frac{\Delta_{SAS}}{\Delta(\theta=0)}$. After [47]. 65
3.19 Schematic diagram of two parallel 2DEG in presence of a parallel magnetic flux Φ_0. The arrows show the path of a typical tunneling electron. 66
3.20 (a) The angular dependence of the activation energy of a bilayer sample for $\Delta_{SAS} = 11K$ and different layer imbalances $\sigma = \Delta\nu/\nu_T$. The arrows indicate a combination of both real spin and pseudo-spin behavior at $\sigma = 0.6$. (b)The same for $\Delta_{SAS} = 1K$. The effect of tilt angle is greatly reduced due to reduced tunneling. After [40]. 67

3.21 (a) Charge density $\rho(\mathbf{r}) - \frac{\mathbf{1}}{\pi\ell^2}$ of a CP3 skyrmion lattice at $\nu_T = 0.97$, $d/\ell = 1.0$, zero tunneling and $\Delta_Z = 0.002(e^2/\ell)$ in unit cell. (b) Energy per electron of the same kind of lattice relative to that of a meron lattice at $\nu_T = 0.8$ at zero tunneling v.s. layer separation. (c) Z-component of psudo-spin in units of $1/2\pi\ell^2$ of the same lattice in (a). (d) Z-component of the real spin in the same state. Colors do not have a physical interpretation. 72
3.22 In plane component of the (a) spin in upper layer (b) spin in lower layer (c) pseudo-spin in up spin band (d) pseudo-spin in lower spin band of CP3 skyrmion lattice at $d/\ell = 1.0$, zero tunneling, $\Delta_Z = 0.002(e^2/\ell)$ and $\nu_T = 0.97$. All four distributions are associated with one single quantum state of the bilayer system. 73
3.23 (a) Total spin polarization of a CP3 skyrmion lattice state of bilayer system at $\nu_T = 0.8$ and zero tunneling v.s. layer separation for different Zeeman couplings. (b) Energy per electron of the same state relative to the meron state. 74
3.24 (a) Excess of total charge density of the symmetric skyrmion lattice state at $d/\ell = 0.8$, $\Delta_{SAS} = 0.04(e^2/\ell)$ and $\Delta_Z = 0.003(e^2/\ell)$ at filling factor $\nu_T = 1.04$.(b) The contour plot of the same state. (c) In-plane component of the spin distribution of the same state. The size of vectors are proportional to $|\rho_{S\uparrow S\uparrow}|$ at each point. (d) Z-component of the spin $\rho_{S\uparrow S\uparrow} - \rho_{S\downarrow S\downarrow}$. 76
3.25 (a) 3D plot (b) contour plot of the excess of the total charge density of a bilayer system in an HCP3 lattice state at $\nu_T = 1.2$, $d/\ell = 0.1$, $\Delta_{SAS} = 0.04(e^2/\ell)$ and $\Delta_Z = 0.002(e^2/\ell)$. 77
3.26 In-plane component of the (a) spin in the symmetric band $|\rho_{S\uparrow S\downarrow}|$ and (b) in the antisymmetric band $|\rho_{A\uparrow A\downarrow}|$. (c) pseudo-spin in the up spin band $|\rho_{S\uparrow A\uparrow}|$ and (d) pseudo-spin in down spin band $|\rho_{S\downarrow A\downarrow}|$. All these distributions are associated with a single HCP3 state at $\nu_T = 1.2$, $d/\ell = 0.1$, $\Delta_{SAS} = 0.04(e^2/\ell)$ and $\Delta_Z = 0.002(e^2/\ell)$. 78
3.27 (a) Energy difference between the HCP3 crystal or SS crystals and the meron state as a function of tunneling for $\nu_T = 1.2$,$\Delta_Z = 0.0015(e^2/\ell)$ and $d/\ell = 0.1$. (b) Spin and pseudo-spin polarization as a function of tunneling for the HCP3 and SS states. (c) Spin polarization as a function of interlayer separation in the SS state for different values of the Zeeman coupling and filling factors. Here $\Delta_{SAS} = 0.04(e^2/\ell)$ and $\nu_T = 1.04$. 79
3.28 (a) Energy difference between the CP3 or SS states and the SPB state. (b) Spin polarization per electron as a function of bias for $\nu_T = 0.8$,$\Delta_{SAS} = 0.0002(e^2/\ell)$ and $\Delta_Z = 0.01(e^2/\ell)$. (c) Filling factor in the right and left wells in the CP3 state. 80
3.29 Average in-plane spin polarization in the CP3 crystal state as a function of applied bias for $\nu_T = 0.8$,$\Delta_{SAS} = 0.0002(e^2/\ell)$ and $d/\ell = 1.0$. . 81

4.1 A schematic picture of a double quantum well heterostructure. The metallic gates are used to deplete the electron gases in top and bottom wells (green). The contacts are used to make electrical contact to each electron gas. The red layer is the barrier layer. 84
4.2 A schematic picture of a counterflow in a double quantum well. Arrows show the direction of electron (red) movement. The counterflow will move electron-hole (red-white) pairs. 85
4.3 Hall and longitudinal resistances (solid and dotted traces, respectively) in a low density double-layer 2DES at T=50 mK. (a) Currents in parallel in the two layers. (b) Currents in counterflow configuration. Resistances determined from voltage measurements on one of the layers. After [53] 86
4.4 Temperature dependencies of various resistances and conductivities at $\nu_T = 1$ and $d/\ell = 1.48$. (a) Parallel current flow. Open dots: $R^{||}_{xx}$; closed squares: $R^{||}_{xy}$. (b) Counterflow. Open dots R^{CF}_{xx} , closed squares R^{CF}_{xy} . (c) Parallel and counterflow longitudinal conductivities, $R^{||}_{xx}$ and R^{CF}_{xx} , respectively. After [53] 86
4.5 Conventional and Coulomb drag resistances of a low density double layer 2DES. Trace A: Conventional longitudinal resistance R_{xx} measured with current in both layers. Trace B: Hall drag resistance $R_{xy,D}$. Trace C: Longitudinal drag resistance $R_{xx,D}$; sign reversed for clarity. Trace D: Hall resistance R^*_{xy} of the single current-carrying layer (displaced vertically by 5 kV for clarity). Trace B reveals the quantization of Hall drag in the $\nu_T = 1$ excitonic QHE. Insets schematically illustrate the measurement configurations: Current is injected and withdrawn at the open dots; voltage differences between the solid dots are recorded. Traces A, B, and D obtained at $T = 20mK$; trace C at 50 mK. Layer densities: $N1 = N2 = 2.6\times10^{10}$ cm^{-2}, giving $d/\ell = 1.6$ at $\nu_T = 1$. After [55]. 88
4.6 Activation energies of the $\nu_T = 1$ state vs density imbalance. Squares correspond to the activation energy determined from the longitudinal resistance in the lower and upper layer, respectively. Triangles denotes the activation energy obtained from the longitudinal drag. After [56]. 89
4.7 Schematic picture of two neighboring puddles inside a $\nu_T = 1$ bilayer system. Red objects are merons with vectors indicating their dipole moment direction (which is perpendicular to the plane of puddles) and signs indicating their electric charge. The white objects are anti-merons. 90
4.8 Operation of exchange of two indistinguishable particles is equivalent to half the rotation of one around the other. 91
4.9 (a)Finite reciprocal lattice vector construction of a checkerboard strip bias potential with a width $\sim 1.04\ell$ for $\nu_T = 1.02$ lattice. The length of each strip is $\sim 10\ell$.(b) Unit cell of a lattice of merons for layer separation $d/\ell = 1$ at $\nu_T = 1.02$ and zero tunneling. 99

4.10 (a)Charge density of a meron at $d/\ell = 1$, $\nu_T = 1.02$ and zero tunneling. (b) The applied bias strip potential with a width of $\sim 1.04\ell$. (c) Charge density of meron after applying the bias strip potential that creates an imbalance of $\Delta\nu \sim \%4.8$. 101
4.11 (a) The same potential as in figure 4.10(b) . (b) Difference of charge density of a meron after applying the potential with strength $v = 0.01e^2/\ell$ creating an imbalance of $\sim \%4.8$ at $d/\ell = 1.0$, $\nu_T = 1.02$ and zero tunneling. 102
4.12 (a) The same potential as in figure 4.10(b) . (b) Difference of charge density of a meron after applying the potential with strength $v = 0.003e^2/\ell$ creating an imbalance of $\sim \%4.6$ at $d/\ell = 0.5$, $\nu_T = 1.02$ and zero tunneling. 104
4.13 The energy barrier for a meron crossing a strip bias of width $\sim 1.04\ell$ as a function of layer separation for three different imbalances. 106
4.14 Energy barrier for a meron crossing a strip bias of width $\sim 1.04\ell$ as a function of layer imbalance for three different three different layer separations. 106
4.15 Energy barrier for a meron crossing a strip bias as a function of layer imbalance for three different strip widths $\Delta\xi$ at $d/\ell = 0.8$. 107
4.16 Schematic picture of one possible process through which a meron driven toward edge can be absorbed by edge current follwed by emission of a meron with opposite vorticity. The dashed drawing on the right is the image of the meron (vortex). 107

5.1 SEM Images of Ni Nano-Rings a patterned perpendicular recording media. Fabricated using bottom-up Alumina Templates with top-down fabrication techniques. Courtesy of Prof. Johnson's Lab, Department of Physics, University of Oklahoma. 112
5.2 Schematic picture of the possible electron path through a semi-circular circuit threaded by a magnetic flux. 114
5.3 A schematic picture of the groundstate of classical point electrons for 1D array of rings. The ring radius is R and the separation is D. The 1D ordering is antiferroelectric and thus has a double degenerate groundstate. 117
5.4 Normal modes of the 1D ring array with gaps of (a) $2\sqrt{2}\omega_0$ and (b) $2\sqrt{6}\omega_0$. 117
5.5 A plot of the second fourier amplitude of the classical charge distribution on a ring in a 1D horizontal array. The circles are numerical results, the solid line is a scaled plot of eq.(5.7). Scaling is required since the analytic result neglects all higher fourier modes. Inset: a sketch of the charge distribution that corresponds to this Fourier mode. Note that the symmetry of the array is not broken by the charge distribution. 117

5.6 A comparison of numerical and analytical calculations of the staggered polarization and energy as a function of δ in a 1D quantum ring array obtained in the Hartree approximation. The numerical results are for the case include Fourier modes $|m| \leq 1$ (triangles) and $|m| \leq 6$ (boxes). The solid line is the analytic result assum- ing $|m| \leq 1$. The quantity δ is a measure of the competition between the Coulomb interaction and the quantum kinetic energy 120
5.7 Monte Carlo results of the $C_v = \overline{\Delta E}^2$ for different system sizes. The system is a 1+1D classical equivalent of 1D quantum ring array at zero temperature. 123
5.8 Plot of critical coupling $K_c(L)$ at different system sizes taken from the C_v plots.The solid line is a linear fit to the data indicating $K_c(\infty) \approx 0.699$. 124
5.9 Extrapolation of the total magnetization density of the 1+1D classical system to infinite size at couplings $K/K_c(\infty)$=1.45(empty boxes), 1.32(triangles), 1.03(polygons), 0.74(filled boxes), 0.45(stars) and 0.16 (crosses). The solid lines are linear fit to each set of data. 125
5.10 Plots of Binder ratio for different system sizes. The behavior is sharper at larger sizes. 126
5.11 Collapse of Binder plots at the critical region.The best collapse is obtained for $\nu = 1 \pm 0.01$. 126
5.12 Standard deviation of the set of scaled plots of Binder ratio for different exponents.The case for $\nu = 1$ is the best choice which is plotted in Fig.(5.11). 126
5.13 Monte Carlo results of average magnetization of the 1+1D classical system for different system sizes. The change of magnetization tends to be sharper as the system size grows. 127
5.14 Collapse of scaled magnetization data sets for $\nu = 1$ and $\beta = 1/8$ in the critical region. 127
5.15 Standard deviation of the set of scaled plots of magnetization for fixed $\nu = 1$ and different exponent β. The case for $\beta = 1/8$ is the best choice which is plotted in Fig.(5.14). 127
5.16 Plot of the energy of an interacting quantum ring array when all the wavefunctions are constant around the ring (dashed) or all are in the form of $\psi_d = a + b\cos 2\theta$(solid).The points are the actual results coming out of the numerical Hartree calculation indicating that ψ_d is the selected behavior for $\delta < \delta_c \approx 8$. 128
5.17 Plot of the $\cos 2\theta$ potential around a ring (the thick solid line), the ground and first excited state of this potential (thin solid lines) coming out of a simple numerical Schrodinger equation solver and the up and down states (dashed lines) constructed from the two eigenstates(see appendix).The scale of the potential is exaggerated for easier comparison. 129
5.18 Plots of ground state energy of the interacting quantum ring array in the external magnetic flux threading each ring for different couplings δ. The physics is periodic because of Aharanov-Bohm induced phase that is proportional to the flux. 130

5.19 Plot of the two-body potential function in Eq.5.40. The interacting rings in magnetic field select the minimum of this potential for their ground state wavefunction at low couplings. The potential is in units of $\delta\epsilon^2$. 131
5.20 Results of numerical Hartree calculations of the polarization of a 1D quantum ring array threaded by half-flux quantum $\phi/\phi_0 = 1/2$.At $\delta < \delta_c$ before staggered polarization (P_s) starts to develop a finite transverse total polarization(P_x) appears in the system. 131
5.21 Schematic picture of the ground state of a 2D array of singly charged rings. 134
5.22 Staggered polarization as a function of δ in a 2D quantum ring square array obtained in the Hartree approximation. The numerical results are for the case include Fourier modes $|m| \leq 6$. 135

Abstract

Modern experimental methods have made it possible for physicists to investigate matter in extreme conditions. Two of the most extreme conditions are low temperature and low dimensionality. Fabricated semiconductor or metal nano-ring arrays and narrow quantum wells in semiconductor heterostructures at low temperatures provide such an extreme environments for electrons. I will explain these systems in this dissertation.

Quantum Wells: In a closely spaced double quantum well (DQW), electrons are thought to form an interlayer coherent state when a perpendicular magnetic field is applied such that the total Landau level filling factor $\nu_T = 1$. The low energy topological excitations of the electron gas in these structures includes charged pseudo-spin vortices and anti-vortices. By calculating the energy per electron and the electron densities in the Hartree-Fock approximation, we show that there are new excited states with interwoven spin and pseudo-spin and that their presence in the system can explain new experimental results. The excitations of DQW's (called merons) also have important effects on transport in these systems. These objects carry charge, vorticity, and electric dipole moment. Disorder is likely to unbind them and allow them to diffuse through the system independently. Due to their different dipole moments, the various types of merons may then in principle be distinguished in transport activation energies by an interlayer bias potential. We explore the dynamics of merons using Chern-Simon theory for quantum Hall systems. We numerically estimate their energies in various circumstances and compare them to the recent experiments.

Nano-rings: In this dissertation we also fully analyze the possible phases of a model of singly charged one and two dimensional arrays of rings each having a diameter ~ 100 nm. Using the Hartree approximation and Monte-Carlo simulations we demonstrate that the electrostatic polarization of these arrays undergoes a quantum phase transition due to quantum mechanical fluctuations. Using a complete finite size scaling analysis for a one dimensional array we show that this phase transition is in the universality class of the transverse field Ising model. Also we will show that an external magnetic field changes the polarization behavior from anti-ferroelectric to ferroelectric due to the Aharanov-Bohm effect.

Chapter 1

Introduction

One of the most beautiful aspects of physics is the collective phenomena that arise in condensed matter. Systems containing many atoms, molecules or electrons can show completely different behavior than systems containing few particles. For example, interacting manybody systems can display superfluidity and superconductivity as well as a variety of other phase transitions. At the same time, these many particle systems are among the hardest systems to deal with. In classical physics (at high temperatures) it is rarely possible to solve for observables analytically and one has to approach the problem numerically or through simulations. In quantum mechanical systems (low temperatures) the situation becomes even harder: not only we must deal with interactions, but particle interference plays a very important role in the behavior of the system as well. During the past few decades physicists have devised various techniques for dealing with such problems. Although complicated, most of these systems can be classified by two properties that play an essential role in their behavior: their *Symmetries* and *Dimensionality*. Using these common properties physicists are able to analyze manybody systems in various circumstances and make predictions about their behavior or explain the observed phenomena.

Throughout this work the role of dimensionality is crucial. By changing the dimensionality of a system we have actually confined the particles in that system to a different environment than the everyday three dimensional world. This changes the range of quantum and classical fluctuations which in turn affects the collective phenomena in systems leading to behaviors not seen in three dimensions. In particular in quantum mechanics, the solution to the Schrödinger's equation changes. These changes have dramatic effects on the observables of the system depending on the environmental conditions.

But how can one control the dimensionality of a manybody system? Quantum mechanics naturally provides us with an answer: The characteristic energy of fluctuations of a quantum mechanical particle in a specific direction in its host structure, like a crystal or a quantum dot, is nothing but the energy level separation between the particle's ground state and its excited state associated with that direction. To reduce dimensionality we must change the host and environment so that the particle can not access the excited level. This can be done for example, in narrow structures like *quantum rings* and *quantum wells*. In these types of systems the energy level separation is usually $\Delta E \sim \hbar^2/(2m^*W^2)$ in which W is a characteristic length of the system (e.g. the width of the quantum well or the radius of the quantum ring) and m^* is an effective mass of the particle. By reducing the temperature to lower than this energy gap so that $k_BT < \Delta E$ we can prevent the particle from being excited to higher levels thus confining one of its degrees of freedom. As long as the inter-particle interaction is smaller than this energy gap we can assume the particles are confined.

But what about interactions? The inter-particle interaction is usually Coulombic depending on the inverse of the inter-particle separation $E_c = q^2/r$. The inter-particle separation can be controlled by controlling the density, n. For example in two dimensions $r \sim 1/\sqrt{n}$. Thus by controlling the density we control the interactions and can ensure that the system acts in a two (or one) dimensional fashion!

The main work in this dissertation is the study of charged topological excitations of bilayer quantum Hall systems. With today's advancement in semiconductor technology physicists are able to grow almost perfect crystalline layers of semiconductors. By varying the composition of these layers they produce heterostructures (growth techniques will not be discussed in this text as it is out of the scope of the dissertation and we refer the reader to the literature[2; 44]). Electrons in these heterostructures move to regions where they have lowest energy. If the bandgap of the adjacent layers is chosen carefully, it is then possible to confine electrons in a plane only a few atomic layers thick. Such a two dimensional electron gas is not only essential to modern microelectronics, it has led to fundamental new physical systems. For example, under a strong magnetic field (~ 10 T) a two dimensional electron gas's (2DEG) response to external drives is extremely unusual[51]. The longitudinal resistivity of the 2DEG is zero and the transverse conductivity is an integer multiple of an elementary constant. The discovery of this phenomena known as the *Quantized Hall Effect* by Klaus von Klitzing was awarded the 1985 physics Nobel prize. The physics of the 2DEG became the subject of intense research after this discovery. It

soon turned out that this system is more like a liquid than a gas. At low enough densities the electrons are localized by the strong magnetic field and their kinetic energy is frozen out at low enough temperatures ($\ll$ 100 Kelvin). This liquid can become dissipationless and incompressible.

By varying the magnetic field and lowering the temperature, even more surprising results were discovered. For example the system can, at certain field strengths, appear perfectly metallic, as if no magnetic field were applied. At other field strengths still more quantized levels were observed[51]. These highly non-linear results were later explained by works of Robert B. Laughlin who along with Horst L. Störmer and Daniel Tsui won Nobel prize for physics in 1998.

Rich new phases were discovered later when such quantum wells were grown close together. In a typical double quantum well structure, two GaAs quantum wells are separated by an AlAs barrier layer. The tunneling conductance between the two layers can then be studied. The results of these studies strongly indicated that the two electron gasses have become coherent and selected a new type of ground state[49]. This is now a well established description of the ground state of this system[27]. In this state they behave as though they are together in a single layer. One is able to change the tunneling strength between these two layers or change the separation between them and study various responses of the system.

The most prominent property of a double well system is the existence of a new degree of freedom for electrons. In a quantum mechanical picture each electron can be in one layer or in a superposition of layer states. This degree of freedom is isomorphic to spin. The spin of an electron can either be up or down or be in a superposition of up and down so that it is pointing in a perpendicular direction. This new degree of freedom, called *pseudo-spin* changes the spectrum of the excitations of the electron gas in a bilayer system. However the nature of the excitations will still remain similar to the spin excitations in single layers. A valid interpretation of the data from different responses of the bilayer system is still not well known.

In this dissertation we will focus on nuclear magnetic relaxation time (NMR) and activation energy measurement data. We will show that new types of excitations exist in bilayer systems that include both spin and pseudo-spin. Some of these excitations that are very important in explaining experimental results are *topological*. A topological excitation is a particular kind of smoothly varying spatial (or sometimes temporal) distribution in charge or spin density of electrons. This distribution can not be deformed to a uniform distribution by a continuous set of transformations.

It will turn out that these excitations can be responsible for the unexpected NMR results. We will also show how the topological pseudo-spin excitations of bilayer system can dissipate energy in these systems and that the dissipation is activated, with activation energy behavior consistent with experiments.

In the second chapter we will review physics of an electron gas in a two dimensional quantum well under a strong magnetic field. We will explain how the integer quantum Hall effect arises. However our emphasis will be on topological spin excitations, their dynamics and the measurements by which we can detect them. This chapter is a review of the works done in late 80's and early 90's to explain the integer quantum Hall effect. For more detailed review we refer the reader to the literature[18; 22]. In the third chapter we will review the physics of the coherent state of the electrons in double quantum wells and try to explain how the same kind of excitations exists in bilayer systems but this time of pseudo-spin nature. In this chapter the fundamental theory was developed following references[24; 27]. In this chapter we will also explain the microscopic Hartree-Fock approximation used to calculate the densities of the bilayer system. The numerical results and all the plots presented are the works of the author. We will then extend the theory presented in this chapter to include the spin of electrons and explain the microscopic Hartree-Fock calculations with spin and pseudo-spin and present our numerical results. In the fourth chapter we will introduce two different theoretical approaches mainly to explain the results of an activation energy measurement performed on double quantum wells[56].

In the fifth chapter we will introduce our model of interacting quantum ring arrays. In this model, the Coulomb interaction between electrons confined in each ring can induce a *phase transition* in the electrostatic polarization of the system. The polarization suddenly changes from zero to a finite value in this system as one changes the inter-ring separation. The geometry in which the electrons are confined and the Coulomb interaction are crucial for occurrence of this transition. In a true second order phase transition the observables of the system diverge in the thermodynamic limit when the system size diverges[1]. The first signal for this behavior is the increase of the value of an observable of the system as the size of the system increases. This signal is observed in Monte Carlo simulations as we will see in this chapter. We will explain the approximate analytic calculations of the polarization in this system. Then we will present our more precise numerical results that demonstrates novel quantum phase transitions in their electrostatic polarization. These numerical results include Hartree iterative calculation and Monte-Carlo simulation.

Finally in chapter six I will summarize my new results and discuss possible future directions of this research.

Chapter 2

Two Dimensional Electron Gas Under Strong Magnetic Field

In this section I will first discuss the physics of the integer quantum Hall effect. I will then present a detailed discussion of the ferromagnetism and topological spin excitations at a specific range of densities called filling factor $\nu = 1$ following references [22; 27]. At the end following references [22; 48] I will discuss two very important characteristics of these spin excitations that can be detected in experiments.

2.1 Overview of Integer Quantum Hall Effect

Transport in a two dimensional electron gas under strong magnetic field displays a completely different behavior than many other two dimensional systems at low temperatures. The basic experimental observation is that at sufficiently low temperatures and high magnetic fields the system becomes dissipationless in the longitudinal direction(Fig. 2.1):

$$\rho_{xx} \to 0 \tag{2.1}$$

and the conductance in the transverse direction, called the Hall conductance, becomes quantized:

$$\sigma_{xy} = \nu \frac{e^2}{h} \tag{2.2}$$

in which ν is a constant integer called the filling factor and will be defined later. This ratio depends on the density and magnetic field strength. Surprisingly this behavior is material and geometry independent. This kind of transport does not happen at higher temperatures (higher than few Kelvins depending on the host semiconductor).

How are electrons confined in two dimensions? There has been tremendous effort during past few decades to fabricate layered semiconductor structures to host two

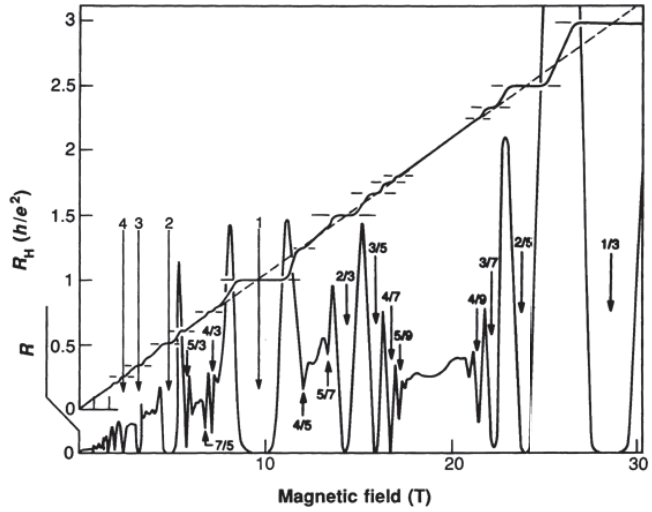

Figure 2.1: Integer and fractional quantum Hall effect: Hall(transverse) and longitudinal resistance v.s. magnetic field. The numbers indicate the filling factor of the Landau levels. After ref.[51]

dimensional electron gases. Progress in Molecular Beam Epitaxy (MBE) has allowed for the possibility of growing epitaxial crystal structures that have high enough mobility to show the quantum Hall effect.[18] Von Klitzing and collaborators did their experiments on a silicon metal-oxide-semiconductor field effect transistor (MOSFET) whereas Tsui, Stormer and Gossard did their experiment on a two dimensional electron gas (2DEG) formed at the interface of a GaAs/AlGaAs heterojunction for which the mobility is much higher. GaAs/AlGaAs heterojunctions have since become the standard system on which quantum Hall effect experiments are performed.

In GaAs the band gap is 1.5 eV and $Al_xGa_{1-x}As$ has a larger gap that depends on the concentration, x, of aluminum. In a modulation-doped heterojunction $Al_xGa_{1-x}As$ is n-doped with silicon away from the interface to minimize the disorder potential caused by the donor ions. Because of the band mismatch electrons move from the $Al_xGa_{1-x}As$ to the GaAs. Once in the GaAs, the electrons feel the Coulomb attraction due to the positive ions left behind and as a consequence the bands are bent near the interface as shown in Fig.2.2. Once equilibrium is reached the electrons at the interface will occupy the narrow quantum well created by the bent bands. Here they are free to move in the directions parallel to the junction but see a random potential that has contributions from the remote ionized donors and imperfections in the interface. If the subband spacing due to the confinement in the direction perpendicular to the interface is much bigger than all relevant energy scales

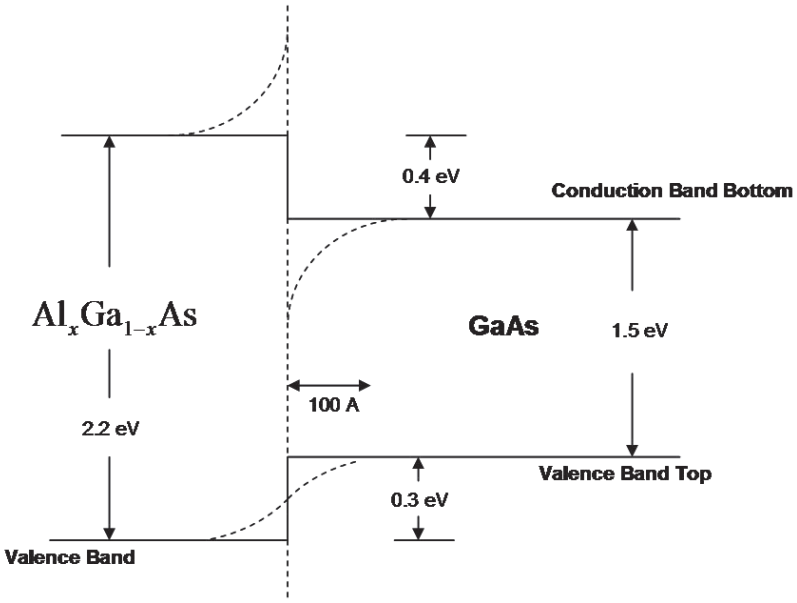

Figure 2.2: Schematic profile of band structure at the junction of GaAs-AlGaAs.

then the electron gas in the quantum well is, for all practical purposes, a 2DEG. In simple words, electrons in these narrow structures move to the layer with the lowest energy band gap. This way electrons are trapped in the lowest level of the quantum well and at low enough temperatures their third spatial degree of freedom is frozen, so that they are effectively living in two dimensions.

Since the presented work here is not an experimental research we will not go into the experimental details of fabrication of these structures. The density of trapped electrons in the GaAs host can be controlled by dopants like Si or Ge. The densities of these gases are typically on the order of 10^{10} cm^{-2} . Today samples are of very high quality with very low disorder, with mobilities up to 600000 cm^2/Vs. These samples are cooled in dilution refrigerators usually down to around 30 mK .

We will first review the two dimensional transport of a non-interacting electron gas in the classical regime. When a current flows into a thin conducting material under a perpendicular magnetic field (Fig.2.3) a voltage drop develops perpendicular to the direction of current flow due to the Lorentz force.

Consider a 2DEG, in the absence of any disorder. The electron gas is translationally invariant, and as a result we can make a Gallilean transformation to a frame moving with velocity $-\mathbf{v}$ relative to the lab frame. In this frame the electron moves at a velocity $+\mathbf{v}$ and carries a current density:

$$\mathbf{J} = -ne\mathbf{v} \tag{2.3}$$

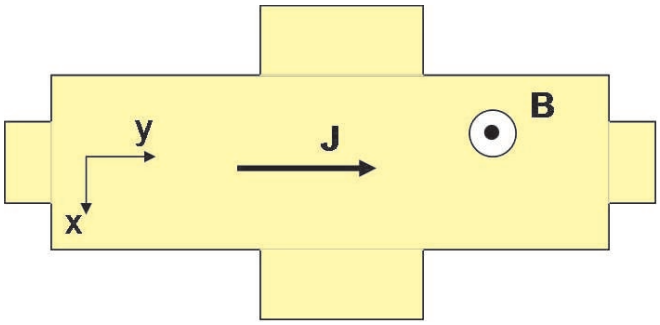

Figure 2.3: Schematic picture of a Hall bar experiment. The magnetic field is perpendicular to the plane and the contacts are made to edges of the bar.

where n is the density of electrons. In the lab frame the electric field is zero, $\mathbf{E} = 0$ and magnetic field $\mathbf{B} = B\hat{z}$. In the moving frame to lowest order in v/c :

$$\begin{aligned} \mathbf{E} &= \frac{-1}{c}\mathbf{v} \times \mathbf{B} \\ \mathbf{B} &= B\hat{z}. \end{aligned} \tag{2.4}$$

The transformation above is nothing but the Lorentz force. We can then write the electric field in eq.(4.30) as:

$$\mathbf{E} = \frac{B}{nec}\mathbf{J} \times \mathbf{B} \tag{2.5}$$

The resistivity tensor is defined as:

$$E^{\mu} = \rho_{\mu\nu} J^{\nu} \tag{2.6}$$

so we can identify the resistivity tensor for a disorder-free classical 2DEG as:

$$\underline{\rho} = \frac{nec}{B} \begin{pmatrix} 0 & -1 \\ +1 & 0 \end{pmatrix} \tag{2.7}$$

The conductivity tensor is then:

$$\underline{\sigma} = \underline{\rho}^{-1} = \frac{B}{nec} \begin{pmatrix} 0 & +1 \\ -1 & 0 \end{pmatrix} \tag{2.8}$$

Note that the above argument was purely based on Lorentz covariance so that the same argument can be made for a quantum system. As we can see in two dimensional translationally invariant systems no matter what kind the charge carrier is (since only the density entered here) and whether it is classic or quantum there is no quantization of the Hall effect and no dissipationless behavior. This result clearly shows that the quantum Hall effect as seen in the transport data (Fig.2.1) does not occur in

translationally invariant systems! and some level of disorder is needed to destroy this invariance.

To analyze the quantum dynamics of 2DEG under strong magnetic field we have to first choose a gauge. Because the experimental set up is a Hall bar (fig. 2.3) it is more convenient to use the Landau gauge:

$$\mathbf{A} = xB\hat{y} \tag{2.9}$$

which obeys $\nabla \times \mathbf{A} = B\hat{z}$. The Hamiltonian of an electron in two dimensions is then:

$$H = \frac{1}{2m}\Big[p_x^2 + \Big(p_y + \frac{eB}{c}x\Big)^2\Big]. \tag{2.10}$$

Because of the translational invariance in the y direction we can write the eigenfunction of the above Hamiltonian as:

$$\psi_k(x, y) = e^{iky} f_k(x) \tag{2.11}$$

in which f_k is eigenfunction of the Hamiltonian:

$$\begin{aligned} h_k &= \frac{1}{2m}p_x^2 + \Big(\hbar k + \frac{eB}{c}x\Big)^2 \\ &= \frac{1}{2m}p_x^2 + \frac{1}{2}m\omega_c^2(x + k\ell^2)^2. \end{aligned} \tag{2.12}$$

which is the Hamiltonian of a one dimensional oscillator with frequency $\omega_c = eB/mc$, (called the *cyclotron frequency*) and central position $X_k = -k\ell^2$. The parameter $\ell = \sqrt{\frac{\hbar c}{eB}}$ is called the *magnetic length*, and is the characteristic length for variation of the electron's wave function in the x-direction. The energy spectrum of the electron then will be:

$$E_{nk} = (n + \frac{1}{2})\hbar\omega_c. \tag{2.13}$$

Each of these levels $n = 0, 1, 2, ...$ is called a Landau level. As we can see, the energy levels are independent of quantum number k and consequently each Landau level is degenerate. Assuming periodic boundary conditions in the y direction in a rectangular sample with dimensions L_x and L_y, the momentum quantum number k will be quantized as $k_n = 2\pi n\ell^2/L_y$. On the other hand each k_n is associated with the center of the wave function at $X_n = -k_n\ell^2$. This center can be anywhere on the x axis. The degeneracy, N of a Landau level will then be:

$$N\Delta X = N\frac{2\pi\ell^2}{L_y} = L_x \Rightarrow N = \frac{L_x L_y}{2\pi\ell^2} = N_\Phi \tag{2.14}$$

in which $N_\Phi = BL_xL_y/\Phi_0$ and $\Phi_0 = hc/e$ is the flux quantum. The eigenfunction of the Hamiltonian for the n-th Landau level is then

$$\psi_{nX}(\mathbf{r}) = \frac{1}{\sqrt{L_y}} e^{iXy/\ell^2} H_n(x+X) e^{-(x+X)^2/(2\ell^2)}, \tag{2.15}$$

where the guiding center parameter is $X = -k\ell^2$ and H_n is the n-th Hermite polynomial.

Consider the case where electrons fully occupy an integer number of Landau levels at the ground state. We introduce the filling factor:

$$\nu = N/N_\Phi \tag{2.16}$$

in which N is the total number of electrons and N_Φ is the order of Landau level degeneracy. In this case the filling factor ν is an integer number. When the perpendicular magnetic field is strong enough to make the degeneracy of the Landau levels macroscopic and their spacing $\hbar\omega_c$ high enough so that their mixing due to disorder or interaction can be seen as small perturbation, we are in the *quantum Hall regime*.

2.1.1 Integer Quantum Hall Edge States

Now we consider the problem of electrons in a Hall bar of finite width. Assuming translational invariance in the y direction, the wavefunction of the states inside this region still look like $\psi(x,y) = \frac{1}{L_y} e^{iky} f_k(x)$ but the function $f_k(x)$ is the eigenfunction of the Hamiltonian:

$$h_k = \frac{p_x^2}{2m} + \frac{1}{2} m\omega_c^2 (x + X_k)^2 + V(x) \tag{2.17}$$

in which $V(x)$ is the disorder potential confining the bulk extended states. Assuming this confining potential is smooth enough (i.e. it varies on scales longer than a magnetic length ℓ) the peak of this wavefunction is still near the point $X_k = -k\ell^2$. The eigenvalues ϵ_k will no longer be exactly linear in k but will still reflect the kinetic energy of the cyclotron motion plus the local potential energy $V(X_k)$. We then see that the group velocity:

$$\mathbf{v}_k = \frac{1}{\hbar} \frac{\partial \epsilon_k}{\partial k} \hat{y} \tag{2.18}$$

has opposite signs on the two edges. This means in the ground state there are edge currents of opposite signs flowing in the sample. The semi-classical interpretations of these currents is that they represent *skipping orbits* in which the circular cyclotron motion is interrupted by collisions with the walls at the edges.

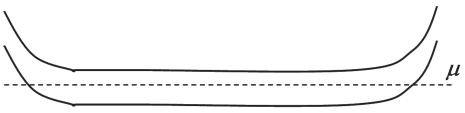

Figure 2.4: Illustration of a smooth confining potential varying in the x direction. The horizontal dashed line indicates the equilibrium Fermi level. Electrons head into the page on the left edge state and out of the page on the right. The magnetic field is perpendicular to the lines.

Using an argument quite analogous to the Landauer picture of transport in narrow wires [15; 16] we can calculate the Hall conductance in this Hall bar (Fig. 2.3). The skipping orbits only travel in one direction to the left on the upper edge and to the right on the lower edge. If the Fermi energy is the same on the two edges these currents cancel out. To get a net current we need a difference in the chemical potential of the two edges. The Hall voltage drop is basically this electrochemical potential difference between the two edges. We will show later on that there are gapless excitations only at the edges of the Hall bar (Fig. 2.4) and that means we can ignore any changes in the electrostatic potential in the bulk and take the electrochemical potential difference between the two edges in the form of a chemical potential difference. To calculate the Hall current we have to add up the group velocities of the occupied states:

$$I = -\frac{e}{L_y}\int_{-\infty}^{+\infty} dk \frac{L_y}{2\pi}\frac{1}{\hbar}\frac{\partial \epsilon_k}{\partial k} n_k \tag{2.19}$$

in which we have assumed at the moment that only a single Landau level has been occupied and n_k is the probability of the state k of the Landau level being occupied. At zero temperature we will have then:

$$I = -\frac{e}{h}\int_{\mu_R}^{\mu_L} d\epsilon = -\frac{e}{h}[\mu_L - \mu_R] \tag{2.20}$$

By definition the Hall voltage drop is:

$$+eV_H = +e[V_R - V_L] = \mu_R - \mu_L. \tag{2.21}$$

Hence:

$$I = -\nu\frac{e^2}{h}V_H \tag{2.22}$$

where we have considered the possibility that ν different Landau levels are occupied in the bulk which means there are ν separate edge channels contributing to the current. So the final result is:

$$\sigma_{xy} = -\nu\frac{e^2}{h}. \tag{2.23}$$

For a single channel in a one dimensional wire in the Landauer picture a disordered region will reduce the conductivity to:

$$I = \frac{e^2}{h}|T|^2, \tag{2.24}$$

where $|T|^2$ is the probability for an electron to be transmitted through the disordered region. The reduction in transmitted current is due to *backscattering*. However in our quantum Hall problem in the Hall bar scattering into the backward moving states is impossible because all the electrons in the channels of one edge move in the same direction. This property is called *chirality*. As long as the disorder in the bulk is smooth enough to preclude any charge transfer from one edge to the other the backscattering does not occur in the edge states and therefore the edge currents are dissipationless. Disorder might scatter an electron at one edge from one channel to the other but still it will not reduce the current as long as they are moving in one direction. This is why the chirality of the edge keeps the Hall conductance quantized independent of disorder.

Disorder will broaden the Landau levels in the bulk and provides a reservoir of (localized) states which will allow the chemical potential to vary smoothly with density. These localized states will not contribute to the transport and so the Hall conductance will be quantized over a plateau of finite width in density. However if all the states in the bulk were localized then it would not be possible to have a transition from one plateau to the other. This transition can be explained qualitatively using a semiclassical percolation picture.

2.1.2 Percolation

Remote dopants like Si ions in donor layers along with other impurities make up a spatially random but smoothly varying potential landscape. Because the kinetic energy is quantized, the electron in a Landau level can not continuously increase its kinetic energy, so energy conservation restricts its motion to regions of constant potential. This argument means that the electronic wave functions in our landscape potential will be localized on equipotential lines. At very low densities in the ground state the electrons are living in deep valleys while at very high densities the electrons are localized on mountain tops (Fig.2.5). From very low densities by increasing density the valleys fill up gradually until when they can percolate and make up new wider regions. This process continuous until a percolation transition reaches across the system and electrons can travel from one end to the other, which means the Fermi

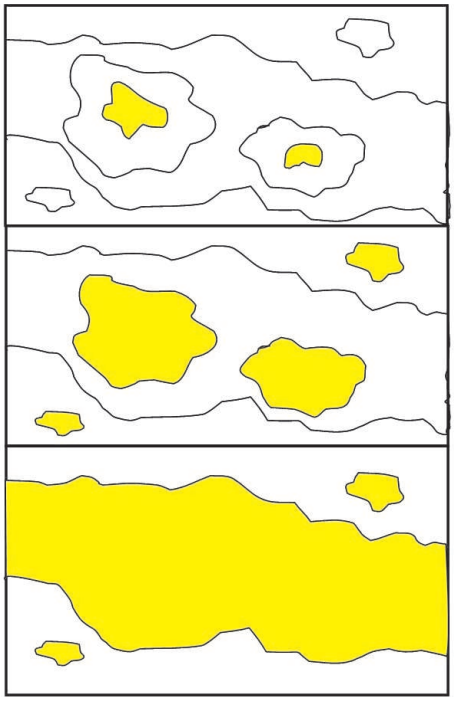

Figure 2.5: Contour map of a smooth disorder landscape. close lines indicate valleys. The yellow filled areas are the increasing sea level whole shore lines finally percolate from one end of the system to the other end.

surface is now in a region extended states. This percolation transition corresponds to the transition between quantized Hall plateaus (fig. 2.1). To see why note that below the percolation point the electrons are localized in the valleys so the system is insulating but above the percolation point the electrons have occupied some extended states and they can carry a quantized Hall current. Another way to see this is that above the transition the confining potential will make a shoreline along the edge of the system and the edge states will carry current from one edge of the system to the other.

2.2 Quantum Hall Ferromagnets

For a 2DEG one might imagine that electrons in the quantum Hall regime have their spin dynamics frozen out by the Zeeman splitting $g\mu_B B$. In free space with $g = 2$ the Zeeman splitting is exactly equal to the cyclotron splitting $\hbar\omega_c \sim 100K$ as illustrated in Fig.2.6(a). Thus at low temperatures we would expect for filling factors $\nu \leq 1$ all the spins would be fully aligned. It turns out that this naive expectation is incorrect in GaAs for two reasons. First, the small effective mass (m^*=0.08) in the conduction

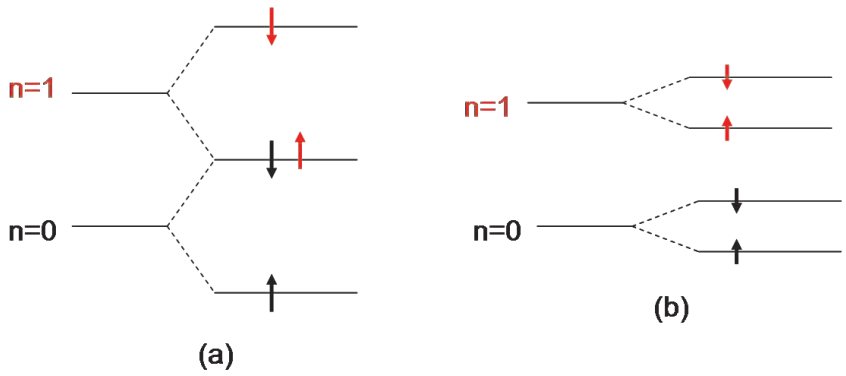

Figure 2.6: Schematic diagram of Landau level splitting due to Zeeman coupling in (a) vacuum (b) in GaAs host.

band of GaAs increases the cyclotron energy by a factor of m/m^* ∼14. Second, spin-orbit scattering effects reduces the effective coupling to the external magnetic field by a factor of -5 making the g factor -0.4. The Zeeman energy is thus some 70 times smaller than the cyclotron energy and typically has a value of about 2 Kelvin as indicated in Fig.2.6(b).

This decoupling of the scales of the orbital and spin energies means that it is possible to be in a regime in which the orbital motion is fully quantized ($k_BT \ll \hbar\omega_c$) but the low-energy spin fluctuations are not completely frozen out ($k_BT \sim g^*\mu_B B$). The spin dynamics in this regime are unusual and interesting because the system is an itinerant magnet with a quantized Hall coefficient. As we shall see, this leads to some quite novel physical effects. The introduction of the spin degree of freedom means that we are dealing with the QHE in multicomponent systems. This subject has a long history going back to an early paper by Halperin [17] and has been reviewed extensively [19; 18]. In addition to the spin degree of freedom there has been considerable recent interest in other multicomponent systems in which spin is replaced by a pseudospin representing the layer index in double well QHE systems which will be the subject of next chapters in this dissertation. Experiments on these systems are discussed by Shayegan and J. Eisenstein in [18]. Our discussion will focus primarily on ferromagnetism near and at filling factor $\nu = 1$.

2.2.1 Coulomb Exchange

In the description of the integer quantum Hall effect in the previous sections the Coulomb interaction was ignored because disorder plays a much more important

role and the Coulomb force does not have any effect on the integer Hall plateaus as a perturbation. However in analyzing the spin fluctuations of this system the Coulomb interaction becomes important[20]. For the $\nu = 1$ system in its ground state one can imagine that all the electrons are in the majority(up) spin subband of the lowest Landau level and so the system is spin polarized. However it is the Coulomb exchange force that prevents the fluctuations from destroying this order. In other words, magnetism in a quantum Hall ferromagnet does not happen because of direct magnetic forces, but rather because of a combination of electrostatic forces and the Pauli principle.

In a fully ferromagnetic state all the spins are parallel and hence the spin part of the wave function is exchange symmetric:

$$|\psi\rangle = \Phi(z_1, ..., z_N)|\uparrow\uparrow\uparrow\uparrow ... \uparrow\rangle. \tag{2.25}$$

The spatial part Φ of the wave function must therefore be fully antisymmetric and vanish when any two particles approach each other. This means that each particle is surrounded by an exchange hole which thus lowers the Coulomb energy per particle. For filling factor $\nu = 1$ this Coulomb exchange energy is:

$$\frac{\langle V_{ex}\rangle}{N} = -\sqrt{\frac{\pi}{8}}\frac{e^2}{\epsilon\ell} \sim 200K \tag{2.26}$$

This energy scale is two orders of magnitude larger than the Zeeman splitting and hence strongly stabilizes the ferromagnetic state. Indeed at $\nu = 1$ the ground state is spontaneously fully polarized at zero temperature even in the absence of the Zeeman term. Ordinary ferromagnets like iron are generally only partially polarized because of the extra kinetic energy cost of raising the fermi level for the majority carriers. Here however the kinetic energy has been quenched by the magnetic field and all states in the lowest Landau level are degenerate. For $\nu = 1$ the large gap to the next Landau level means that we know the spatial wave function Φ essentially exactly. It is simply the single Slater determinant, representing the fully filled Landau level. This simple circumstance makes this perhaps the world's best understood ferromagnet.

2.2.2 Charge-Spin Entanglement

As was mentioned in the previous chapter the exchange energy prevents the spin fluctuations of electrons at $\nu = 1$ from destroying the ferromagnetic order. This high exchange energy cost then must be included when one adds an electron to this system.

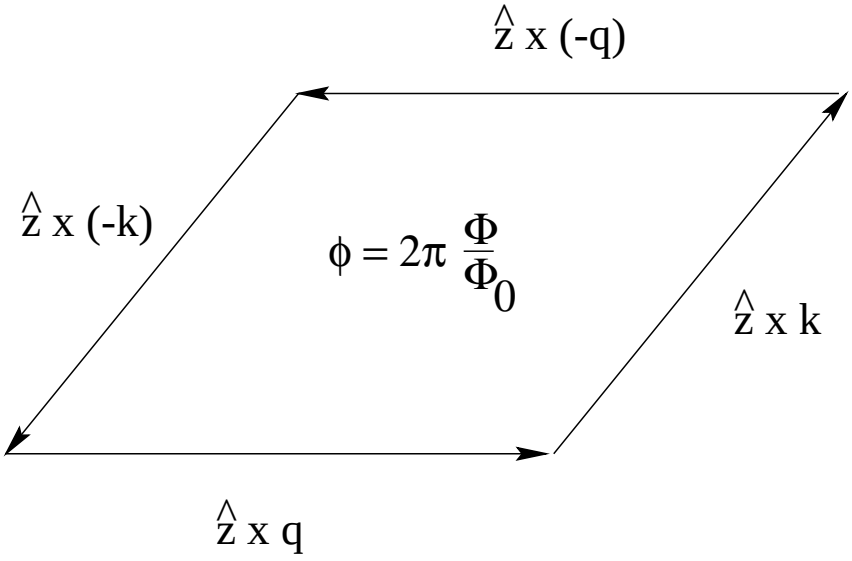

Figure 2.7: Illustration of magnetic translation and phase factor. When an electron travels around a parallelogram (generated by $\tau_q\tau_k\tau_{-q}\tau_{-k}$) perpendicular to the magnetic field it picks up a phase $\phi = 2\pi\phi/\phi_0 = q \times k$.

The extra electron has no choice but to be in the minority (down) spin level. In an ordinary (B=0) 2D electron system just like 3D systems the charged excitations are quasi-electrons according to Landau Fermi liquid theory[74], and the ground state is not spin polarized. The spin excitations are single spin flips or spin waves. However in quantum Hall ferromagnets the lowest Landau level dynamics of electrons changes this scenario.

In order to understand how spin dynamics effects the orbital motion in the lowest Landau level we start with understanding the dynamics of electrons confined in the lowest Landau level at $\nu = 1$ [21]. For this purpose we introduce a new gauge to represent the vector potential, called the *symmetric gauge*: $\mathbf{A} = B(-y, x, 0)$. In this gauge electrons are two dimensional symmetric oscillators with their frequency equal to the cyclotron frequency. Using the symmetric gauge the eigenfunction of the kinetic energy and angular momentum of a non-interacting electron in the lowest Landau level is:

$$\phi_m(z) = \frac{1}{(2\pi 2^m m!)^{1/2}} z^m \exp\Big(-\frac{|z|^2}{4}\Big) \tag{2.27}$$

in which m is the angular momentum quantum number and $z = (x+iy)/\ell$. Any wave function of an electron in the lowest Landau level (LLL) is then a linear superposition

of powers of z multiplied by an exponential weight. This is nothing but the space of all analytic functions:

$$\psi(z) = f(z) \exp\Big(- \frac{|z|^2}{4} \Big) \tag{2.28}$$

in which f is an analytic function of z. We define an inner product in this space between two analytic function as

$$(f, g) = \int d\mu(z) f^*(z) g(z) \tag{2.29}$$

where

$$d\mu(z) = (2\pi)^{-1} dx dy e^{-|z|^2/2}. \tag{2.30}$$

We can define bosonic ladder operators that connect ϕ_m to $\phi_{m\pm1}$ (which acts on the polynomial part of ϕ_m only):

$$a^\dagger = \frac{z}{\sqrt{2}} \tag{2.31}$$

$$a = \sqrt{2} \frac{\partial}{\partial z} \tag{2.32}$$

so that

$$\begin{aligned} a^\dagger \phi_m &= \sqrt{m+1} \phi_{m+1} \\ a \phi_m &= \sqrt{m} \phi_{m-1} \\ (f, a^\dagger g) &= (af, g) \\ (f, ag) &= (a^\dagger f, g) \end{aligned} \tag{2.33}$$

All operators that have nonzero matrix elements only within the lowest Landau level (LLL) can be expressed in terms of a and $a^\dagger$. It is essential to notice that the adjoint of $a^\dagger$ is not $z^*/\sqrt{2}$ but $a = \sqrt{2}\frac{\partial}{\partial z}$, because z^* connects states in the LLL to higher Landau levels. Actually a is the projection of $z^*/\sqrt{2}$ onto the LLL as seen clearly in the following expression:

$$(f, \frac{z^*}{\sqrt{2}} g) = (\frac{z}{\sqrt{2}} f, g) = (g^\dagger f, g) = (f, ag). \tag{2.34}$$

So we find:

$$\overline{z^*} = 2 \frac{\partial}{\partial z} \tag{2.35}$$

in which the overbar indicates projection onto the LLL. Since $\overline{z^*}$ and z do not commute, in order to project any function of z and z^* we have to first normal order z^*'s to the left of z's and then replace them with their corresponding LLL operators.

Now we are equipped to understand the dynamics in the LLL. Let's find out how the density is written in the LLL. The Fourier transform of the density operator $\rho(\mathbf{r}) = \sum_i \delta^2(\mathbf{r} - \mathbf{r}_i)$ is:

$$\rho_{\mathbf{q}} = \frac{1}{\sqrt{A}} e^{-i\mathbf{q}\cdot\mathbf{r}} = \frac{1}{\sqrt{A}} e^{-\frac{i}{2}qz^*} e^{-\frac{i}{2}q^*z} \tag{2.36}$$

where A is the area of the system and $q = q_x + iq_y$. Hence:

$$\overline{\rho_{\mathbf{q}}} = \frac{1}{\sqrt{A}} e^{-iq\frac{\partial}{\partial z}} e^{-\frac{i}{2}q^*z} = \frac{1}{\sqrt{A}} e^{-\frac{|q|^2}{4}} \tau_{\mathbf{q}} \tag{2.37}$$

where

$$\tau_{\mathbf{q}} = e^{-iq\frac{\partial}{\partial z} - \frac{i}{2}q^*z} \tag{2.38}$$

is a unitary operator satisfying the closed Lie algebra

$$\tau_{\mathbf{q}}\tau_{\mathbf{k}} = \tau_{\mathbf{q}+\mathbf{k}} \sin\left(\frac{\mathbf{q}\times\mathbf{k}}{2}\right) \tag{2.39}$$

$$[\tau_{\mathbf{q}}, \tau_{\mathbf{k}}] = 2i\tau_{\mathbf{q}+\mathbf{k}} \sin\left(\frac{\mathbf{q}\times\mathbf{k}}{2}\right) \tag{2.40}$$

where $\mathbf{q}\times\mathbf{k} = \ell^2(q_xk_y - q_yk_x)$ is scalar. We also have $\tau_{\mathbf{q}}\tau_{\mathbf{k}}\tau_{-\mathbf{q}}\tau_{\mathbf{k}}\tau_{-\mathbf{k}} = e^{i\mathbf{q}\times\mathbf{k}}$. These relations are familiar features of the group of translations in a magnetic field, because $\mathbf{q}\times\mathbf{k}$ is exactly the phase generated by the flux in the parallelogram generated by $\mathbf{q}\ell^2$ and $\mathbf{k}\ell^2$. Hence the τ's form a representation of a magnetic translation group (fig.2.7). In fact $\tau_{\mathbf{q}}$ translates the particle a distance $\ell^2\hat{z}\times\mathbf{q}$. This means that different wave-vector components of the charge density do not commute ! It is from here that the nontrivial dynamics arises even though the kinetic energy is totally quenched in the LLL subspace.

We can generalize this formalism for many electron systems

$$\overline{\rho_{\mathbf{q}}} = \frac{1}{\sqrt{A}} \sum_{i=1}^{N} \overline{e^{-i\mathbf{q}\cdot\mathbf{r}_i}} = \frac{1}{\sqrt{A}} \sum_{i=1}^{N} e^{-q^2/4} \tau_{\mathbf{q}}(i) \tag{2.41}$$

$$\overline{S^{\mu}_{\mathbf{q}}} = \frac{1}{\sqrt{A}} \sum_{i=1}^{N} \overline{e^{-i\mathbf{q}\cdot\mathbf{r}_i}} S^{\mu}_i = \frac{1}{\sqrt{A}} \sum_{i=1}^{N} e^{-q^2/4} \tau_{\mathbf{q}}(i) S^{\mu}_i \tag{2.42}$$

Where ρ and S are Fourier transforms of total density and spin of the electrons respectively. From the above we immediately see that

$$[\overline{\rho_{\mathbf{q}}}, \overline{S^{\mu}_{\mathbf{q}}}] \neq 0 \tag{2.43}$$

which means spin dynamics is entangled to the charge dynamics in the LLL. This is the origin of the fact that spin excitations in the quantum Hall ferromagnet change the charge density, which we will discuss more in the next sections.

2.2.3 The Effective Action

For a smooth spin distribution it is very useful to construct an effective action for the electron-electron interaction in the lowest Landau level. The technique of projection to lowest Landau level in the section 2.2.2 can be used here as a tool to derive the action directly from the microscopic Hamiltonian. Following previous works [27], the projection of the Hamiltonian in the LLL looks like

$$\overline{V} = \frac{1}{2}\sum_{\mathbf{q}} V_{\mathbf{q}}(\overline{\rho}_{\mathbf{q}}\overline{\rho}_{-\mathbf{q}} - Ne^{\frac{-q^2\ell^2}{2}}) \tag{2.44}$$

in which $V_{\mathbf{q}} = \int d^2r V(r)e^{-i\mathbf{k}\cdot\mathbf{r}}$. The ground state wave function of the $\nu = 1$ quantum Hall ferromagnet is represented as follows:

$$\Psi = \Psi_V|\uparrow\uparrow\uparrow\uparrow\uparrow\uparrow\cdots\uparrow\rangle \tag{2.45}$$

in which Ψ_V is a Vandermonde determinant wave function believed [26] to be the exact orbital ground state wave function of the $\nu = 1$ electron system

$$\Psi_V = \Pi_{i<j}(z_i - z_j)\Pi_k \exp(-|z_k|^2/4\ell^2) \tag{2.46}$$

in which $z = x + iy$ is the coordinate of an electron. One can create any spin distribution $\mathbf{m}(\mathbf{r})$ using the rotation operator

$$\mathcal{O} = \sum_{j=1}^{N} \mathbf{\Omega}(\mathbf{r}_j)\cdot\mathbf{S}_j = \sum_q e^{\frac{q^2\ell^2}{4}}\Omega^{\mu}_{\mathbf{q}}S^{\mu}_{-\mathbf{q}} \tag{2.47}$$

where $\mathbf{\Omega}(\mathbf{r}) = \hat{\mathbf{z}}\times\mathbf{m}(\mathbf{r})$ is the angle over which the spin is rotated. The rotated state then is as follows

$$|\psi[\mathbf{m}(\mathbf{r})]\rangle = e^{-i\mathcal{O}}|\psi_0\rangle \tag{2.48}$$

The change in expectation value of the energy of the rotated state will then be

$$\begin{aligned}\delta E &= \langle\psi_0 e^{i\mathcal{O}}[\overline{V}, e^{-i\mathcal{O}}|\psi_0\rangle \\ &= -i\langle\psi_0|[\overline{V},\overline{\mathcal{O}}]|\psi_0\rangle - \frac{1}{2}\langle\psi_0|[\overline{\mathcal{O}},[\overline{\mathcal{O}},\overline{V}]|\psi_0\rangle + \cdots\end{aligned} \tag{2.49}$$

in which we can keep the first few terms of the expansion if we assume that the spin rotates smoothly in space on a scale longer than a magnetic length (in other words $\Omega_{\mathbf{q}}$ is negligible when $q\ell > 1$). Since $\Omega^z = 0$, the first term of the expansion is zero (because the ground state is fully polarized in z-direction) so we will have

$$\begin{aligned}\delta E &= -\frac{1}{2}\langle\psi_0|[\overline{\mathcal{O}},[\overline{\mathcal{O}},\overline{V}]|\psi_0\rangle \\ &= -\frac{1}{4}\sum_k V_k\langle\psi_0|[\overline{\mathcal{O}},[\overline{\mathcal{O}},\overline{\rho}_k\overline{\rho}_{-k}]|\psi_0\rangle.\end{aligned} \tag{2.50}$$

The commutator in the above equation can be evaluated using

$$\begin{aligned}[\overline{\rho}_k, \overline{\mathcal{O}}] &= \frac{1}{\sqrt{A}} e^{-\frac{k^2}{4}} \sum_j [\tau_k(j), \sum_q \Omega^\mu_{\mathbf{q}} \overline{S}^\mu_{-\mathbf{q}}] \\ &= \frac{2i}{A} \sum_{j,q} e^{-\frac{k^2}{4}} \Omega^\mu_{\mathbf{q}} S^\mu_j \tau_{k-q}(j) \sin\Big(\frac{\mathbf{q}\times\mathbf{k}}{2}\Big). \end{aligned} \tag{2.51}$$

which can be used to calculate the energy as follows

$$\begin{aligned}\delta E &= -\frac{N}{2A^2} \sum_k V_k \sum_q (\Omega^x_{\mathbf{q}} \Omega^x_{-\mathbf{q}} + \Omega^y_{\mathbf{q}} \Omega^y_{-\mathbf{q}}) \frac{1}{4} (\mathbf{q}\times\mathbf{k})^2 h(k) \\ &= \frac{\rho^0_s}{2} \sum_q [(iq)\Omega^x_{\mathbf{q}} (-iq)\Omega_{-\mathbf{q}} + (iq)\Omega^y_{\mathbf{q}} (-iq)\Omega^y_{-\mathbf{q}}] \\ &= \frac{\rho^0_s}{2} \int d^2r [(\nabla\Omega^x)^2 + (\nabla\Omega^y)^2] = \frac{\rho^0_s}{2} \int d^2r (\nabla\mathbf{m})^2. \end{aligned} \tag{2.52}$$

in the above the spin stiffness ρ^0_s is implicitly defined as

$$\rho^0_s = -\frac{\nu}{32\pi^2} \int dk k^3 V_k h(k) \tag{2.53}$$

and $h(k) = -\exp(-k^2/2)$ is the pair correlation function. The physical origin of the stiffness is the loss of exchange and correlation energy when the spin orientation varies with position. For the Coulomb interaction, $\rho^0_s = e^2/(16\sqrt{2\pi}\epsilon\ell) \sim (e^2/\epsilon\ell) 2.49 \times 10^{-2}$ at $\nu = 1$.

The above calculation of spin stiffness is from a first-principle calculation which agrees with other types of numerical calculations [27]. The classical model defined by the Eq.(2.52) is called the O(3) *non-linear sigma model* and has been studied in great detail[25]. It is important to note that the quantum fluctuations will only correct the higher gradient terms. It turns out [27] that the next non-zero correction is of the fourth order and after a lengthy calculation [27] it has been shown that

$$\delta E^{(4)} \sim \frac{1}{2} \int d^2r d^2r' V(|\mathbf{r}-\mathbf{r}'|) \delta\rho(\mathbf{r}) \delta\rho(\mathbf{r}') \tag{2.54}$$

in which $\delta\rho = (\nu/8\pi)\epsilon_{\mu\nu}(\partial_\mu\mathbf{m}\times\partial_\nu\mathbf{m})\cdot\mathbf{m}$ is the Pontryangin index of the spin field [25]. We should emphasize that according to ref.[27] the above result is only true in long length scales where the Coulomb interaction is small.

From the above we conclude that the static part of the effective action for the $\nu = 1$ quantum Hall ferromagnet is

$$\mathcal{L}_{static} = \frac{\rho^0_s}{2} \int d^2r (\nabla\mathbf{m})^2 + \frac{1}{2} \int d^2r d^2r' V(|\mathbf{r}-\mathbf{r}'|) \delta\rho(\mathbf{r}) \delta\rho(\mathbf{r}') \tag{2.55}$$

To find the dynamical part we write down the equation of motion for the spin. The Fourier transform of the spin polarization density with the appropriate weight factor is

$$\begin{aligned}\frac{dm^{\mu}_{\mathbf{q}}}{dt} &= \frac{4\pi}{\nu}e^{\frac{q^2}{4}}\langle\frac{dS^{\mu}_{\mathbf{q}}}{dt}\rangle = -\frac{4\pi i}{\hbar\nu}\langle\tilde{\psi}|[e^{\frac{q^2}{4}}S^{\mu}_{\mathbf{q}},\overline{V}]|\tilde{\psi}\rangle \\ &\simeq -\frac{4\pi}{\hbar\nu}\langle\psi_0|[\overline{O},[\overline{O},\overline{V}]]|\psi_0\rangle \\ &= \frac{4\pi}{\hbar\nu}\frac{\delta}{\delta\Omega^{\mu}_{-\mathbf{q}}}E[\mathbf{m}]. \end{aligned} \tag{2.56}$$

in which we have used the equation 2.50 in the last line and used the approximate series expansion for the exponential. Up to first order in $\mathbf{m}$ the above equation would be

$$\frac{d\mathbf{m}_{\mathbf{q}}}{dt} = \frac{4\pi\rho^0_s q^2}{\hbar\nu}\hat{z}\times\mathbf{m}_{\mathbf{q}}. \tag{2.57}$$

The above equation can be derived from a Lagrangian like

$$L_{dynamical} = \frac{\nu}{4\pi}\int d^2r\mathcal{A}[\mathbf{m}]\cdot\partial_t\mathbf{m} \tag{2.58}$$

in which

$$\nabla_{\mathbf{m}}\times\mathcal{A} = \mathbf{m} \tag{2.59}$$

This dynamical term is exactly the Berry phase for the spin [14]. So from the whole discussion in this chapter the effective Lagrangian for the quantum Hall ferromagnet is as follows

$$\begin{aligned}\mathcal{L} &= \frac{\nu}{4\pi}\int d^2r\mathcal{A}[\mathbf{m}]\cdot\partial_t\mathbf{m} - \frac{\rho^0_s}{2}\int d^2r(\nabla\mathbf{m})^2 + \\ &- \frac{1}{2}\int d^2r d^2r' V(|\mathbf{r}-\mathbf{r}'|)\delta\rho(\mathbf{r})\delta\rho(\mathbf{r}') - \Delta_z\int d^2r\ m_z(r). \end{aligned} \tag{2.60}$$

in which the last term is the Zeeman coupling.

2.2.4 Topological Spin Excitations

There are various types of low lying excitations in the quantum Hall ferromagnet including collective mode charge density excitations just like in superfluid ^{4}He. However unlike in ^{4}He this *magnetophonon* is gapped[22] as observed in Raman scattering[23]. Another kind of excitation is spin waves which are also gapped with a minimum energy gap equal to the Zeeman energy[22]. These excitations are neutral and do not take part in transport. The main focus of this section is however the charged excitations which will affect the transport experiments.

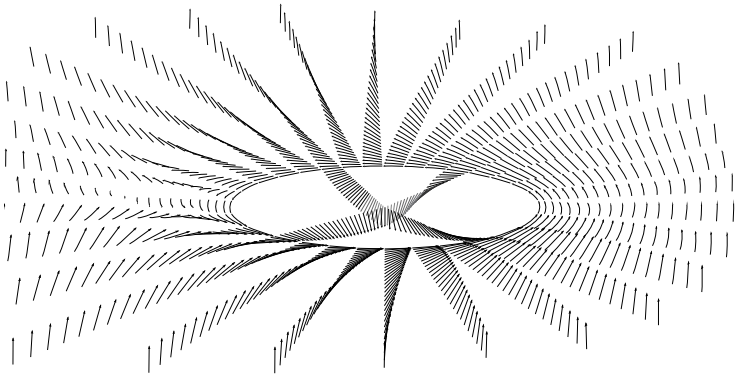

Figure 2.8: The spin of electrons in a skyrmion gradually rotate from the minority direction at the center to the majority direction at the boundaries. Unlike a U(1) vortex, a skyrmion does not have any singularity at the center. Figure taken from [22]

.

The lowest lying charged excitations of the QHF turns out to have an exotic nature. The main features of these excitations are

- *They are of a spin nature and can be expressed solely in terms of the electron spin field.*
- *They are topological, which means they carry topological number, and they are stable against normal perturbations.*
- *They are not localized but spread over a finite area.*

We will explain all of these below. Before we start going into details about these features we should realize a very important connection in two dimensional quantum Hall systems[22]:

Adiabatic insertion of a flux quantum changes the state of the system by pulling in (or pushing out) a quantized amount of charge.

This statement is always true for a *dissipationless* system with *quantized Hall conductivity*. To see why, imagine we insert a thin long solenoid that carries magnetic flux into a QH system (fig. 2.9) and increase the magnetic flux in it slowly (adiabatically) from 0 to Φ_0. This adiabatic process is possible and reversible because the ground state is gapped so there is a time scale $\hbar/\Delta$ such that processes that take a

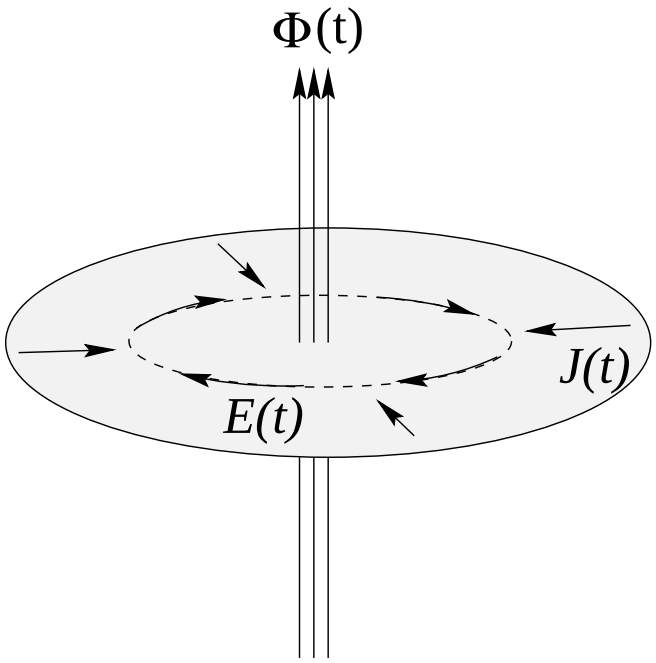

Figure 2.9: Illustration of insertion of an imaginary flux tube into QH state.

time longer than this can be considered adiabatic. Now according to Faraday's law the change of flux induces a rotating electric field in the 2DEG

$$\oint_C d\mathbf{r} \cdot \mathbf{E} = -\frac{1}{c}\frac{d\Phi}{dt} \tag{2.61}$$

This electric field does not have Fourier component with frequencies $\hbar\omega < \Delta$ so it will not cause any dissipation which means ρ_{xx} and ρ_{yy} stay zero. This electric field however induces a current density

$$\mathbf{E} = \rho_{xy}\mathbf{J} \times \hat{z} \tag{2.62}$$

so that

$$\rho_{xy} \oint_C \mathbf{J} \cdot (\hat{z} \times \mathbf{r}) = -\frac{1}{c}\frac{d\Phi}{dt}. \tag{2.63}$$

The integral on the left hand side represents the total current flowing into the region enclosed by the contour C (fig. 2.9). Thus the charge inside this region obeys

$$\rho_{xy}\frac{dQ}{dt} = -\frac{1}{c}\frac{d\Phi}{dt}. \tag{2.64}$$

After one quantum of flux has been added the final charge is

$$Q = \frac{1}{c}\sigma_{xy}\Phi_0 = \frac{h}{e}\sigma_{xy}. \tag{2.65}$$

Thus on the quantized Hall plateau at filling factor ν where $\sigma_{xy} = \nu e^2/h$ we have the result

$$Q = \nu e. \tag{2.66}$$

Reversing the sign of the total flux would reverse the sign of the charge. Note that addition of a quantum of flux does not have any effect on the wave function of the electrons because the induced Aharanov-Bohm phase for a quantum of flux is unity. So this shows that adding a quantum of flux to the QH system adiabatically means we have added a charge of νe. This is also true for each of the electrons in a QH system with filling factor ν: Each electron is localized in an area of $2\pi\ell^2$ which contains a magnetic flux of $\Phi = 2\pi\ell^2 B = h/ec = \Phi_0$.

Now let's examine the spin excitations. Let's start with the Lagrangian of a free electron traveling in the QHF. This electron has a velocity $\dot{x^\mu}$. If this electron is moving adiabatically (in other words if it is staying in the ground state of the QHF) then its spin should follow the local spin orientation $m^\mu(\mathbf{r})$ of the QHF. Consequently the rate of change of the electron spin orientation would be $\dot{m^\mu} = \dot{x^\nu}\frac{\partial m^\mu}{\partial x^\nu}$, this change of spin induces a Berry phase (see previous section). The Lagrangian of this electron then would be

$$\mathcal{L} = -\frac{e}{c}\dot{x^\mu}A_\mu + \hbar S\dot{m^\mu}\mathcal{A}_\mu[m] \tag{2.67}$$

where A_μ is the usual electromagnetic vector potential and $\mathcal{A}_\mu$ is the geometrical vector potential defined in Eq. (2.59). There should be other terms included in this Lagrangian, kinetic energy and Coulomb which we omit for now. Given $\dot{m}$ we can write the Lagrangian as follows

$$\mathcal{L} = -\frac{e}{c}\dot{x^\mu}(A_\mu + a_\mu) \tag{2.68}$$

where:

$$a_\mu = -\Phi_0 S(\partial_\mu m_\nu)\mathcal{A}^\nu. \tag{2.69}$$

This new vector potential represents the *Berry connection* which reproduces the Berry phase. This extra fake magnetic vector potential has a magnetic field $\mathbf{b}$:

$$\begin{aligned} b &= \epsilon^{\alpha\beta}\partial_\alpha a_\beta \\ &= -\Phi_0 S\epsilon^{\alpha\beta}\Big\{(\partial_\alpha\partial_\beta m^\nu)\mathcal{A}_\nu + (\partial_\beta m^\nu\partial_\alpha m^\gamma)\frac{\partial\mathcal{A}_\nu}{\partial m^\gamma}\Big\} \\ &= -\Phi_0 S\epsilon^{\alpha\beta}(\partial_\beta m^\nu\partial_\alpha m^\gamma)\frac{1}{2}F^{\nu\gamma} \end{aligned} \tag{2.70}$$

in which

$$F^{\nu\gamma} = \frac{\partial\mathcal{A}^\gamma}{\partial m^\nu} - \frac{\partial\mathcal{A}^\nu}{\partial m^\gamma} \tag{2.71}$$

and using the gauge $F^{\nu\gamma} = \epsilon^{\alpha\nu\gamma} m_\alpha$ we obtain

$$b = -\Phi_0 \tilde{\rho} \tag{2.72}$$

where

$$\tilde{\rho} = \frac{1}{8\pi} \epsilon^{\alpha\beta} \mathbf{m} \cdot \partial_\alpha \mathbf{m} \times \partial_\beta \mathbf{m}. \tag{2.73}$$

The above is a *topological density* called Pontryagin density. This is equivalent to the winding number of a vortex in a two dimensional field but here m is three dimensional [22]. The charge density here is determined by the two dimensional plane of the vector field $\mathbf{m}(\mathbf{r})$. Each point on the plane can also be mapped into a three dimensional unit vector determined by its location in the plane. For example, the point $\mathbf{r} = r(\cos\phi\hat{x} + \sin\phi\hat{y})$ could correspond to the 3D vector $\mathbf{v} = \sin\theta\cos\phi\hat{x} + \sin\theta\sin\phi\hat{y} + \cos\theta\hat{z}$ where

$$\theta = \frac{\pi r}{1 + r}. \tag{2.74}$$

Then the function $\mathbf{m}(\mathbf{r})$ can be written as $\mathbf{m}(\mathbf{v})$, which is a map of a unit 3-vector into a unit 3-vector. Such smooth mappings can be separated into different topological classes[25] by their Pontryagin index, the integral of 2.73 over the plane. It can be shown that for smooth maps this integral wit a uniform boundary conditions is an integer.

So far we have found out that any spin distribution is equivalent to an additional Berry phase or fake magnetic flux. According to our previous discussion, addition of a magnetic flux is equivalent to addition of an electric charge so our additional magnetic flux will be equivalent to an electrostatic charge density

$$\delta\rho = \nu e \frac{b(r)A}{\Phi_0} = -\nu e \tilde{\rho} \tag{2.75}$$

in other words a spin field distribution $\mathbf{m}(r)$ that has nonzero topological charge density $\tilde{\rho}$ carries an electrostatic charge density equal to $-\nu e\tilde{\rho}$. This remarkable result is telling us that in QHF the electrostatic potential can couple to the spin of the electrons! The most elementary topological spin texture($n = \pm 1$ vorticity) is a soliton called *Skyrmion*. At the center of a skyrmion (fig.2.8) spin of electron is down (in minority band) and it gradually rotates toward the boundary where it is pointing upward (majority direction). This smooth change of spin direction lowers the energy of the system. In fact it is possible to calculate the energy of a Skyrmion using an effective action for the quantum Hall ferromagnet. It is also possible to use a microscopic Hamiltonian with the Hartree-Fock approximation to numerically

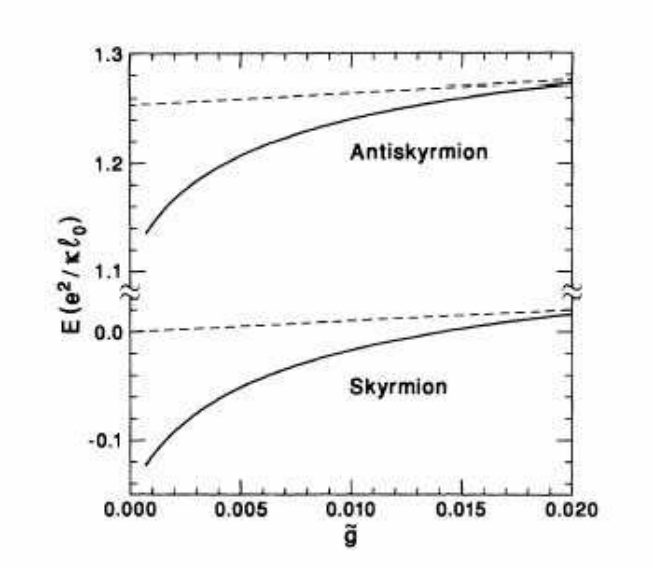

Figure 2.10: Energy of a skyrmion and anti-skyrmion compared to single spin flip energy v.s. g-factor (Zeeman coupling). After ref.[24].

estimate the energy of Skyrmions (Fig.2.10). The latter method is the main subject of this dissertation for this and other quantum Hall system excitations. Figure (2.10) shows the Hartree-Fock (HF) approximation for the energy of a skyrmion and an anti-skyrmion compared to energy of a spin particle-hole excitation. At low Zeeman energies it is seen that the cost of a spin flip is higher than (double) the skyrmion's cost [24]. This also has been confirmed by effective action calculations [20; 25].

A skyrmion in which the spin at the center is in minority direction has charge $-e$ while the spin at the center of an anti-skyrmion with charge $+e$ is in the majority direction. The number of flipped spins in a skyrmion is dependent on the size of the skyrmion. The charge of the skyrmion is sharply quantized but the size of the skyrmion depends on two parameters: the Coulomb interaction and the Zeeman coupling, the last two terms in the Lagrangian in Eq.2.60. The Coulomb interaction tries to make the spin distribution as smooth and uniform as possible and the Zeeman term tries to shrink the size to lower the Zeeman cost. The competition between the two terms determines the size of the skyrmion.

2.2.5 Detecting Skyrmions

Direct evidence for the existence of skyrmions was first observed by Barret *et. al.* [28] using a novel optically pumped NMR technique. The Hamiltonian for spin of a nucleus is [31]

$$H_N = -\Delta_N I_z + \Omega \mathbf{I} \cdot \mathbf{S} \tag{2.76}$$

where Δ_N is the nuclear Zeeman frequency about three orders of magnitude smaller than the electron Zeeman frequency, Ω is the hyperfine coupling and $\mathbf{S}$ is the electron spin density at the nuclear site. If, as a first (mean field) approximation we replace $\mathbf{S}$ by its value

$$H_N \approx (-\Delta_N + \Omega\langle S_z\rangle) I_z. \tag{2.77}$$

we can see that due to coupling with electron spins the precession frequency of the nucleus will be shifted by an amount proportional to the magnetization of the electron gas. The magnetization deduced using the so called Knight shift is shown in fig. 2.11. The electron gas is 100% polarized at $\nu = 1$, but the polarization drops off sharply (and symmetrically) as charge is added or subtracted. This is in sharp disagreement with the prediction of the free electron model as shown in the figure. The initial steep slope of the data allows one to deduce that 3.5-4 spins reverse for each charge added or removed. This is in excellent quantitative agreement with Hartree-Fock calculations for the skyrmion model [24]. Other evidence for skyrmion comes from the large change in Zeeman energy with field due to the large number of flipped spins. This has been observed in transport [32] and in optical spectroscopy [33]. Spin-orbit effects in GaAs make the electron g factor -0.4. Under hydrostatic pressure g can be tuned towards zero which should greatly enhance the skyrmion size. Evidence for this effect has been seen [34].

2.2.6 Skyrmion Dynamics

In the last section I briefly discussed how it is possible to find evidence for existence of skyrmions. In this section we will discuss how the dynamics of skyrmions is investigated and related to another very important experimental signature for their existence namely *nuclear magnetic resonance* (NMR). Figure 2.12 shows the relaxation rate of the average nuclear spins[30]. This rate greatly reduces as it approaches the filling factor $\nu = 1$. This means that the nuclear spin relaxes more slowly: in other words it is not coupled to any external force. However at $\nu \neq 1$ the rate increases implying that the nuclear spin relaxes much faster (tens of minutes to many

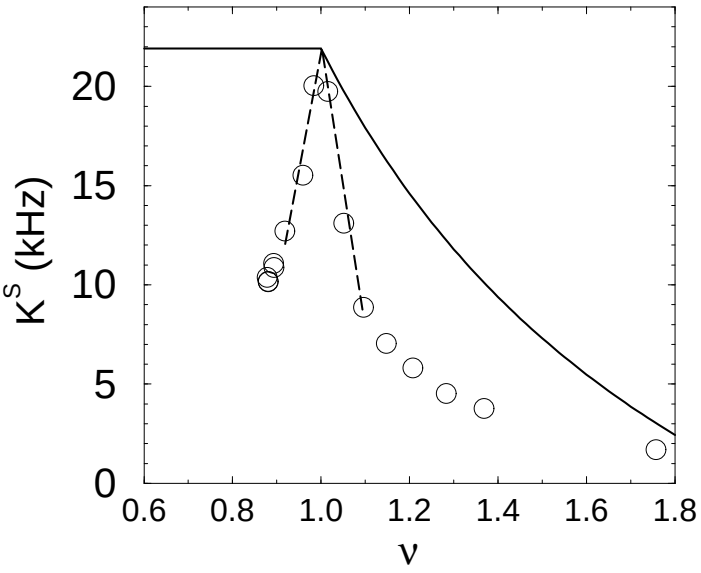

Figure 2.11: NMR Knight shift measurement of the electron spin polarization near filling factor $\nu = 1$. Circles are data of Barret *et. al.*[28]. the dashed line is just connecting the circles. The solid line is the prediction for polarization of non-interacting electron gas.

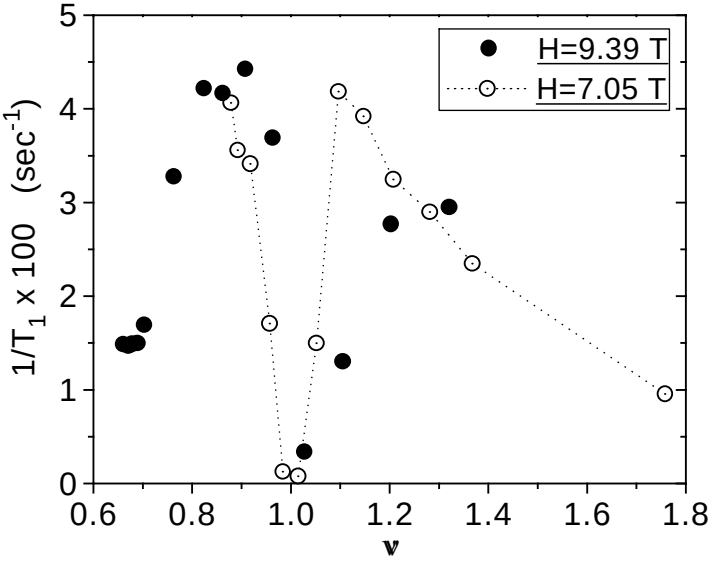

Figure 2.12: NMR nuclear spin relaxation rate $1/T_1$ v.s. filling factor. After Tyco *et. al.* [30]

hours depending on temperature). This suggests that at filling factors away from $\nu = 1$ the nuclear spin is coupled to an external field that carries angular momentum so it can randomize the nuclear spins. The lowest frequency spin wave excitations of the quantum Hall ferromagnet lies above 20-50 GHz [22] while the nuclear spin precession rate is at about 10-100 MHz [22]. On the other hand, based on a free electron model, it is impossible for nuclear and electron spins to undergo a mutual flip because the Zeeman energy would not be conserved. So spin wave excitations in an electron gas unlikely to be responsible for the long nuclear relaxation time. Hence one needs to look for another low energy mode (modes) to explain the data. One candidate is disorder: As was discussed in the section 2.2.2 a spin flip excitation in a QHF is always accompanied by a translation in space. This can provide a mechanism in which a disorder induced spin flipped electron is translated to a region with lower Zeeman and exchange energy cost, and this can be providing a mechanism for a low energy spin mode. However it turns out that this analysis will not predict the sharp feature in data [35].

Skyrmions have degenerate degrees of freedom that can provide low energy spin modes. A skyrmion is symmetric with respect to a global rotation in two dimensional space (U(1)) and also its energy is invariant with respect to translation of its center.

To investigate the dynamics of a single skyrmion [22] we will ignore the structural excitations of a single skyrmion and treat it as one solid object (this is approximately correct since all the spin wave excitations are gapped). Now we can consider a static distribution for the skyrmion, $\mathbf{m}_s(\mathbf{r})$. Then the spin configuration at time t is:

$$\mathbf{m}(\mathbf{r}, t) = \mathbf{m}_s(\mathbf{r} - \mathbf{R}(t)) \tag{2.78}$$

in which $\mathbf{R}(t)$ is the position degree of freedom of the skyrmion. From Eq.2.58 we find

$$L_0 = -\hbar S \int d^2 \dot{m}^\mu \mathcal{A}^\mu[\mathbf{m}] n(\mathbf{r}) \tag{2.79}$$

where

$$\dot{m}^\mu = -\dot{R}^\nu \frac{\partial}{\partial r^\nu} m_0^\mu(\mathbf{r} - \mathbf{R}) \tag{2.80}$$

and $n(\mathbf{r})$ is the density of the electron gas in the presence of the skyrmion

$$n(\mathbf{r}) = n_0 + \frac{1}{8\pi} \epsilon^{\mu\nu} \mathbf{m} \cdot \partial_\mu \mathbf{m} \times \partial_\nu \mathbf{m}. \tag{2.81}$$

The equation 2.79 then becomes

$$L_0 = \hbar \dot{R}^\nu a^\nu(\mathbf{R}) \tag{2.82}$$

where the vector potential

$$a^\nu(\mathbf{R}) = Sn_0 \int d^2 \partial_\nu m^\mu \mathcal{A}^\mu \tag{2.83}$$

and represents a magnetic field

$$\begin{aligned} b_s &= \epsilon^{\lambda\nu} \frac{\partial}{\partial R^\lambda} a^\nu = -Sn_0 \epsilon^{\lambda\nu} \int d^2 r \partial_\lambda (\partial_\nu m^\mu) \mathcal{A}^\mu \\ &= -\frac{Sn_0}{2} \int d^2 r \epsilon^{\lambda\nu} \partial_\nu m^\mu \partial_\lambda m^\gamma F^{\gamma\mu} \\ &= -2\pi n_0 Q_{top} \end{aligned} \tag{2.84}$$

in which we have taken the derivative inside the integral and changed variable to r^μ and in the second line used the equations 2.71 and 2.59.

The Lagrangian in Eq.2.82 is then the kinetic part of the Lagrangian of a massless particle of charge $-eQ_{top}$ moving in uniform magnetic field of strength $B = \frac{\Phi_0}{2\pi\ell^2}$ which is the skyrmion! We have ignored other high energy excitations in this analysis which lead to higher time derivatives because we are only interested in low frequency spin modes for the NMR.

Following the above discussion we can now quantize this Lagrangian. By ignoring the disorder and interaction with other skyrmions we can find the energy levels of the skyrmions which turn out to be Landau levels [22]. Because the skyrmion is massless it will be in the lowest Landau level with a large degeneracy and therefore capable of having very low energy modes that relax the nuclei.

The other free degree of freedom of the skyrmion is its global rotation. The standard analytic form for the skyrmion spin distribution that minimizes the gradient energy [25] is

$$\begin{aligned} m^x &= \frac{2\lambda r \cos(\theta - \phi)}{\lambda^2 + r^2} \\ m^y &= \frac{2\lambda r \sin(\theta - \phi)}{\lambda^2 + r^2} \\ m^z &= \frac{r^2 - \lambda^2}{\lambda^2 + r^2} \end{aligned} \tag{2.85}$$

in which (r, θ) are the polar coordinates in the plane, λ is a constant that controls the size scale, and ϕ is a constant that controls the XY spin orientation for which the energy is invariant. To find the dynamics of the skyrmion rotation one needs to use the Skyrmion Lagrangian and integrate over quantum fluctuations of all the other degrees of freedom of the skyrmion, which is a non-trivial task. Instead we can simply use the symmetries and some valid approximation to avoid this calculation[22].

The effective Lagrangian for the rotational degree of freedom of the skyrmion has to be a function of $\dot{\phi}$ The lowest order symmetry-allowed terms then would be

$$\mathcal{L}_\phi = \hbar K\dot{\phi} + \frac{\hbar^2}{2U}\dot{\phi}^2 + \cdots \tag{2.86}$$

The first order term is allowed because of the breaking of time reversal symmetry by the magnetic field. We can identify K using the fact that the first term must be coming from the Berry phase term. Under slow rotation of all the spins of the skyrmion by 2π the equation 2.79 yields

$$\int d^2rn(\mathbf{r})(-2\pi S)[1 - m_0^z(\mathbf{r})] = \frac{1}{\hbar}\int_0^T \mathcal{L}_\phi = 2\pi K. \tag{2.87}$$

in which the second term has been dropped because it vanishes for $T \to \infty$. The left hand side of the above equation is the value of the in-plane spin polarization of the skyrmion averaged which means the number of flipped spins in the skyrmion, consequently K is the total number of flipped spins in a skyrmion. This number is a classical estimate so it does not need to be integer. To understand more about the dynamics of the skyrmion rotation it is helpfull to derive the Hamiltonian from the Lagrangian Eq.2.86 and analyze the quantum fluctuations. It can be seen easily that the Hamiltonian corresponding to this Lagrangian is

$$H_\phi = \frac{U}{2}(-i\frac{\partial}{\partial\phi} - K)^2. \tag{2.88}$$

The above is the Hamiltonian of a charged XY quantum rotor with moment of inertia $\hbar^2/U$ circling a solenoid containing K flux quanta. From this point of view the Berry phase term is the Aharanov-Bohm term. The eigenfunctions of this Hamiltonian are

$$\psi_m(\phi) = \frac{1}{\sqrt{2\pi}}e^{im\phi} \tag{2.89}$$

and eigenvalues are

$$\epsilon_m = \frac{U}{2}(m - K)^2. \tag{2.90}$$

From the eigenfunction above we see that $|\psi_m|^2 = 1/2\pi$ which means that the global U(1) rotation symmetry broken in the classical solution is restored in the quantum solution because of quantum fluctuations in the coordinate ϕ. This analysis is consistent with the microscopic calculations[36] of the excitation energies in which near parabolic solutions with respect to K has been seen. The typical value is $K \sim 4$. Except for half integer values of K the spectrum of these excitations is non-degenerate and has an excitation gap of the order of U which is of the scale of Coulomb energy

scale $\sim$ 100K . In the absence of disorder even a gap of 1 K would make these excitations irrelevant to NMR. However there are other cases where one can deduce lower energy modes namely in the presence of many skyrmions.

2.2.7 Skyrme Lattice

At filling factors slightly away from $\nu = 1$ there will be a finite density of skyrmions or antiskyrmions in the ground state. The skyrmions interact via the Coulomb potential in Eq.(2.60) so one expects the lowest energy possible state to be a lattice. This lattice state will be a state with broken translational and rotational symmetry and it turns out that in the thermodynamic limit of an infinite number of skyrmions coupled together, it is possible for the global U(1) rotational symmetry breaking to survive quantum fluctuations [22]. If that is true then there would be gapless Goldstone modes for each broken symmetry even in presence of Zeeman field[38]. The mode associated with the broken translational symmetry is the ordinary magneto-phonon of the Wigner crystal.

On the other hand we should be careful that disorder can play an important role. The disorder potential is able to pin skyrmions or a finite density of skyrmions. Also NMR experiments have been performed at temperatures likely above the lattice melting point which suggests that the lattice may have been pinned by disorder and still can support the existence of some form of overdamped diffusive modes derived from Goldstone modes. In any case the essential physics is that the spin fluctuations have strong spectral density at frequencies far below the Zeeman gap.

Ignoring the coupling between magneto-phonon modes and U(1) modes we can capture the long wavelength physics of the Skyrmion lattice with a simple Hamiltonian[38]

$$H = \frac{U}{2}\sum_j (\hat{K}_j - K)^2 - J\sum_{\langle ij\rangle}\cos(\phi_i - \phi_j) \tag{2.91}$$

in which $\hat{K}_j = -i\partial/\partial\phi_j$ for the jth skyrmion. In the microscopic Hartree-Fock calculation that is one of the principal parts of this dissertation, we will see that the ground state of the skyrmion lattice is the one in which one skyrmion is rotated by π with respect to the neighboring one, consequently this antiferromagnetic order forces the coupling to be negative so J in the above Hamiltonian is positive.

This Hamiltonian is very close to the quantum XY rotor model and boson Hubbard model[11]. The angular momentum eigenvalue of the operator $\hat{K}_j$ represents the number of bosons on site j and the U term describes the charging energy cost when

this number deviates from the electrostatically optimal value of K. On the other hand K is the average number of overturned spins so we can assume that $K \gg 1$ i.e. the negative angular momentum states are very high in energy. This makes the boson number interpretation of m justified. A simple qualitative analysis of the boson-Hubbard Hamiltonian in the above will be very useful in understanding the skyrmion lattice dynamics [22]:

For $U \gg J$ the system of bosons are not interacting and so it is insulating with the wave function

$$\psi(\phi_1, \cdots, \phi_2) = \prod_j e^{im\phi_j} \tag{2.92}$$

where m is the nearest integer to K in the ground state. In this state every site has a definite angular momentum and the energy of the system has a gap

$$\Delta \approx U(1 - 2|m - K|) \tag{2.93}$$

justifying the state being insulating. In this phase $|\psi|^2 \approx 1$ and therefore the phases are spread which means the system is quantum disordered. On the other hand for $U \ll J$ the above wave function is no longer an eigenfunction. In this case a crude variational guess can be[39]

$$\psi(\phi_1, \phi_2, \cdots, \phi_N) = e^{\lambda \sum_{\langle ij \rangle} \cos(\phi_i - \phi_j)} \tag{2.94}$$

which is consistent with the invariance under $\phi_j \to \phi_j + 2\pi$ and λ is a variational parameter. In this phase all the phases on neighboring sites are coupled and the system is superconductor. For $\lambda \ll 1$ the wave function ψ is large when all the phases are the same. Expanding around this state gives the Goldstone mode of the superconductor phase. To find the frequency of this mode it is easier to write the Lagrangian of this system

$$\mathcal{L} = \sum_j [\hbar K \dot{\phi}_j + \frac{\hbar^2}{2U} \dot{\phi}_j^2] + J \sum_{\langle ij \rangle} \cos(\phi_i - \phi_j) \tag{2.95}$$

The first (Berry phase) term is a total time derivative and can be dropped. The expansion of the above Lagrangian gives

$$\mathcal{L} = \frac{\hbar^2}{2U} \sum_j \dot{\phi}_j^2 - \frac{J}{2} \sum_{\langle ij \rangle} (\phi_i - \phi_j)^2 \tag{2.96}$$

which is the Lagrangian for the phonons with a linearly gapless spectrum

$$\hbar\omega_q = \sqrt{UJ}(qa) \tag{2.97}$$

where a is a lattice constant. By fitting this spectrum to results of a microscopic calculation one can find the regime of filling factors and Zeeman energies in which the U(1) symmetry is broken. This broken U(1) symmetry state is a new kind of spin state in which the phase angle of the skyrmions is well defined but the number of their over-turned spin is uncertain. Consequently a flipped spin arising from interaction with a nuclear spin will be spread all over the system making the average Zeeman energy cost almost zero. That is why gapless spin fluctuations are possible in this electron gas. These low frequency spin fluctuations can couple to the nuclear spin.

Chapter 3

Double Layer Quantum Hall Systems

In this chapter I will discuss the physics of coherent quantum state of the electron gasses in double quantum well systems using a series of tunneling spectroscopy measurement results (see below for references). I will then explain how one can write an effective action for this system similar to a single layer system described in the previous chapter. Next, I will discuss the known topological excitations of bilayer systems and explain my method of calculations of these excitations following reference [24] and present the results. Finally I will present our theory for excitations that involve spin of electrons and discuss the results.

3.1 Quantum Coherence in Bilayer Quantum Hall Systems

Tunneling spectroscopy is one method of measuring the lifetime of electrons close to the Fermi surface[43]. To study the lifetime of electrons in two dimensional quantum

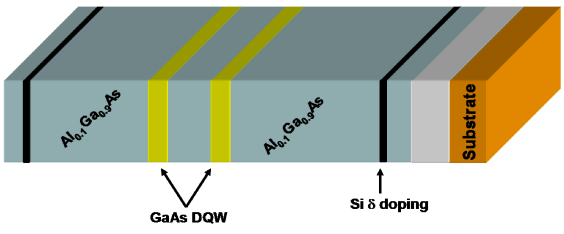

Figure 3.1: Schematic representation of the heterostructure containing the double quantum well (DQW) where the electron bilayers are confined.

wells, *double quantum well heterostructures* (DQW) have been used in which the densities of each well can be adjusted using gate electrodes deposited on the top and bottom of the sample[43] and each well is contacted separately (Fig. 3.1). In most of the experiments the heterostructures are GaAs layers separated by undoped $Al_xGa_{1-x}As$ barriers. The thickness of the wells are of the order of few hundreds of angstroms. The top and bottom gates can deplete the electron gas in either the nearest quantum well or in both the wells depending on the strength of the applied negative voltage. In this way it is possible to cut off the current flow selectively in each quantum well [44]. By cutting the current flow out of for example the upper well one can measure the interlayer tunneling conductance $G = dI/dV$ in terms of interlayer voltage V. The tunneling conductance reveals the single-particle density of states available for the addition of an electron from the other quantum well while the transport measurements provide information about the density of states available for excitation of an electron from the Fermi sea into a conducting state.

A qualitative understanding of some of the spectrums of the double quantum well systems will help us understand the physical importance of the phenomena of *double layer quantum Hall systems*. In strong perpendicular magnetic fields when all the electrons are accommodated in the lowest Landau level in the ground state, there is a Coulomb energy cost for addition of an extra tunneling electron into the electron liquid: $E_c = e^2/\langle a \rangle$ in which $\langle a \rangle$ is the mean inter-particle distance. The kinetic energy of electrons in the lowest Landau level at high magnetic fields is quantized and therefore it is almost impossible for the electrons to change their kinetic energy at very low temperatures($\sim$ 4K) compared to Landau level spacing($\sim$ 100K). In this situation the Coulomb interaction becomes very important and will make the ground state a highly correlated state. In figure (3.2) the zero field differential tunneling conductance are consistent with a simple single-particle picture [45] in which electrons are non-interacting. In this situation, because of energy and momentum conservation, the tunneling can only happen when $eV = E_F - E'_F$ in which E_F and E'_F are the Fermi energy of each quantum well. Consequently there is only a conductance peak at $V = 0$ when the layer densities are equal. On the other hand the zero bias tunneling conductance in the presence of a magnetic field , figure (3.3), is clearly suppressed at zero bias revealing the existence of a Coulomb barrier for tunneling electrons. At higher voltages however there is enough energy for the electron to go to the next Landau level which is followed by another suppression signalling the gap above the

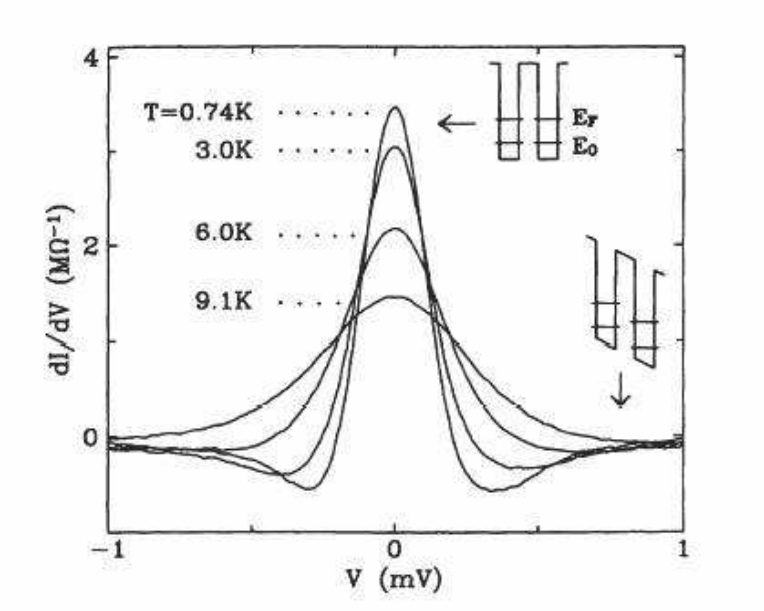

Figure 3.2: Typical tunneling conductance observed in 2D-2D tunneling experiments when quantum wells are balanced, at various temperatures and zero magnetic field. The inset shows the quantum well band diagrams. After [43].

next Landau level[46]. For further analysis of different tunneling data we refer the reader to the literature[45].

One parameter that will effect the I-V current is the interlayer separation d. For large enough separation it is expected that no tunneling can happen. When compared to the effective inter-particle separation in each well, the layer separation determines the order of intra-layer interaction. On the other hand the effective inter-particle distance in the presence of perpendicular magnetic field is the magnetic length $\ell = \sqrt{\hbar/eB}$. Hence for $d/\ell \ll 1$ we expect no tunneling to happen, for $d/\ell > 1$ the tunneling feature discussed in the figure (3.3) appears and it is expected that as d/ℓ is further reduced barrier to injection will grow. Surprisingly this is not what happens in experiment.

Figure (3.4) shows the tunneling conductance for different total densities[49] $N_T = 2eB\nu/h$, thus different magnetic field strengths in the double well system. Reduction of density (from A to D) corresponds to a reduction of the magnetic field which in turn means the reduction of d/ℓ. As d/ℓ decreases a peak at zero bias appears and eventually dwarfs all the other features in the data. The occurrence of a zero bias tunneling peak means that the electrons are finding a new lower energy state to accommodate the incoming electron.

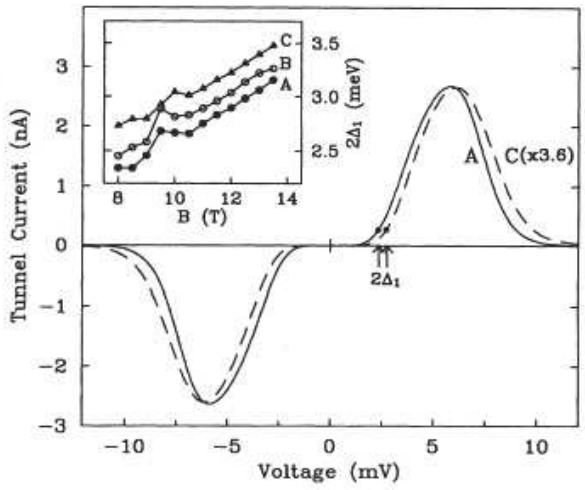

Figure 3.3: Tunneling current v.s. interlayer voltage for three different samples with three tunneling strengths at B=8 T and T=0.6 K. Zero bias suppression is due to gapped excitations of the 2D electron fluid. After [46]

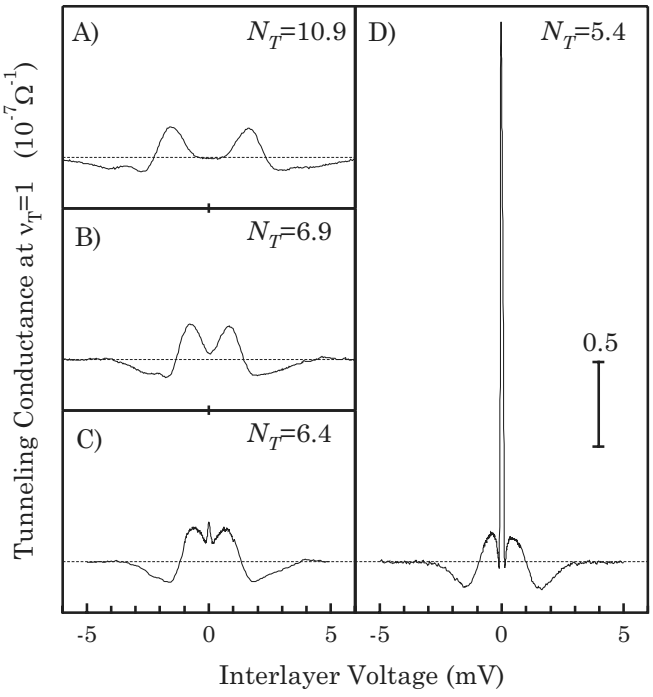

Figure 3.4: Tunneling conductance v.s. interlayer voltage at $\nu_T = 1$ at T=40 mK for four different total densities N_T (in units of 10^10cm^{-2}) and thus three different layer separation d/ℓ. The first three in the left column show regular Coulomb gap behavior while the one in the right column shows a zero bias resonance. After [49].

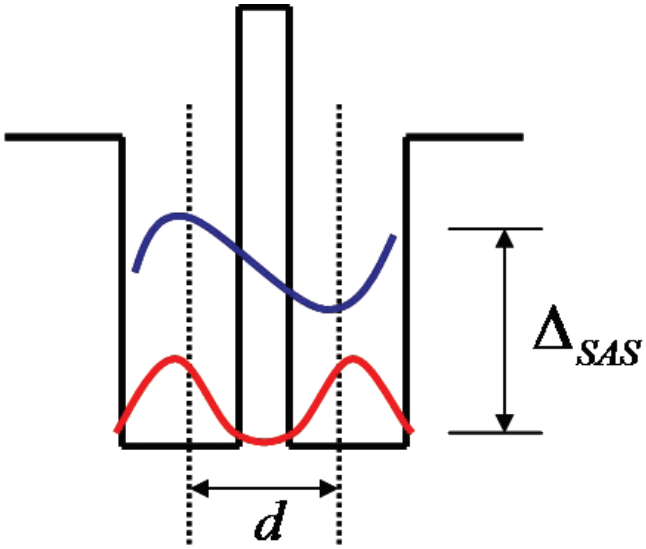

Figure 3.5: A schematic diagram of an ideal double quantum well. The first two eigenstates are symmetric and antisymmetric.

This remarkable feature can be explained by remembering the very important quantum mechanical characteristic of electrons: electrons can have a finite probability amplitude to be in both layers at the same time. The single particle wave function for electrons in a double quantum well system in the ground state has two solutions: a symmetric amplitude and an asymmetric amplitude.(Fig.3.5). The energy separation between the two states (Δ_{SAS}) is nonzero for nonzero tunneling samples. In fact $\Delta_{SAS} = 2t$ where t is the tunneling amplitude through the barrier. By including this *new degree of freedom* for each electron it is understandable that when all electrons are in the symmetric state, the tunneling of an electron from one well to the other does not make any change in the many-body state and thus *leaves the ground state unchanged*. This explains why a peak appears at the zero bias.

Introducing this new degree of freedom of the electrons in double layer systems opens a new path for investigating different properties and new ideas for the many-body electronic states. We can create a group of rotations of the electron state that rotates the electronic wave function from one particular state (like a symmetric combination of the two wells) to another state (like antisymmetric one). This group is mathematically isomorphic to the group of rotations in two dimensional complex space, SU(2) equivalent to that of the spin of an electron. This new degree of freedom therefore is called *pseudo-spin*:

$$|S\rangle = \frac{1}{\sqrt{2}}(|U\rangle + |L\rangle)$$

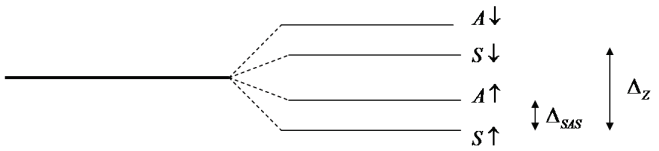

Figure 3.6: Splitting of the Landau levels for $\Delta_{SAS} < \Delta_Z$.

$$|A\rangle \;=\; \frac{1}{\sqrt{2}}(|U\rangle - |L\rangle) \tag{3.1}$$

in which the S(A) refers to symmetric(antisymmetric) combination and U(L) refers to electron being in the upper(lower) layer. If we denote the direction of the state $|U\rangle$ as $+\hat{z}$ (or psudo-spin *up*) and $|L\rangle$ as $-\hat{z}$ (or pseudo-spin *down*) the symmetric state would be parallel to $+\hat{x}$ and antisymmetric state parallel to $-\hat{x}$. An electron with pseudo-spin *up* means an electron is totally in the upper layer and an electron with pseudo-spin in $+\hat{x}$ direction means the electron is both in upper layer and lower layer.

The real spin of electrons is another degree of freedom which was the subject of discussion in the last chapter. In this section we first assume that the Zeeman energy is higher than tunneling gap, $\Delta_Z \ll \Delta_{SAS}$ so that in this situation the spins are frozen and we only include the pseudo-spin fluctuations.

When the total filling factor $\nu_T = \nu_U + \nu_L = 1$ all electrons occupy the symmetric sub-band of the lowest Landau level (Fig.3.6), this will reduce the charging energy cost from a capacitive point of view. A trial wave function exhibiting this *interlayer phase coherence* can be written as follows[37]

$$|\psi\rangle = \prod_k [\cos(\theta/2)c^\dagger_{kU} + \sin(\theta/2)e^{i\varphi}c^\dagger_{kL}]|0\rangle \tag{3.2}$$

in which $c^\dagger_{k\sigma}$ creates an electron with guiding center momentum k (eq. 2.15) in the layer $\sigma = U, L$. The amplitude to find an electron in upper layer in this state is $\cos(\theta/2)$ and in the lower layer it is $\sin(\theta/2)e^{i\varphi}$. This state can represent the ground state of the bilayer system even if there is no tunneling between the layers. This is possible from a quantum mechanical point of view where we can not say for certain that the electron is in a given layer. In the above state θ and φ are then the azimuthal and polar angles of the pseudo-spin vector respectively.

3.2 Bilayer Effective Action

A bilayer system in which the true electron spin is frozen is similar to a quantum Hall ferromagnet in which spins are replaced by pseudo-spin. An important difference is in Coulomb interaction. For non-zero d/ℓ the inter-layer and intra-layer Coulomb interactions are different and thus the Coulomb potential depends on the pseudo-spin direction, unlike the quantum Hall ferromagnets where Coulomb potential is spin independent. In order to correctly include the interactions in the effective action we define[27]

$$V_k^S = \frac{1}{2}(V_k^a + V_k^e) \tag{3.3}$$

$$V_k^A = \frac{1}{2}(V_k^a - V_k^e) \tag{3.4}$$

in which $V_k^a = 2\pi e^2/k$ is the inter-layer Coulomb potential and $V_k^e = \exp(-kd)V_k^a$ is the intra-layer Coulomb potential in Fourier space. The symmetric potential V^S then is pseudo-spin independent unlike the antisymmetric potential V^A. We now define the pseudo-spin dependent densities

$$\hat{\rho}_{\alpha\beta}(X, X') = c^\dagger_{\alpha X} c_{\beta X'} \tag{3.5}$$

in which $\alpha, \beta = U, L$ and X, X' are the guiding center indices. Throughout this chapter we use the Landau gauge (eq. 2.9). We then define the pseudo-spin operators

$$\begin{aligned} P^z(X) &= \rho_{UU}(X, X) - \rho_{LL}(X, X) \\ P^x(X) + iP^y(X) &= \rho_{UL}(X, X) \end{aligned} \tag{3.6}$$

Using the above we can write the antisymmetric part of the Coulomb potential in the lowest Landau level as(see section 2.2.2)

$$\overline{V_A} = 2\sum_k V_k^A \overline{P}_k^z \overline{P}_{-k}^z \tag{3.7}$$

because the coefficients V_k^A are positive this term forces the pseudo-spins to lie in the plane, so the bilayer system is an *easy-plane pseudo-ferromagnet*. This term breaks the SU(2) invariance of the Hamiltonian to U(1). Excluding the antisymmetric part of the Coulomb term the effective action of the bilayer system will be the same as the quantum Hall ferromagnet. To add the antisymmetric part we use the same technique of projection as in section (2.2.2)[27]. The energy change associated with

small deviation of the pseudo-spin vector from $\hat{x}$ direction vanishes at the first order of approximation (as seen in the section 2.2.2). The second order term is

$$\begin{aligned}\delta E^A &= -\sum_k V_k^A \langle\psi_0|2[\overline{O},\overline{P}_k^z][\overline{O},\overline{P}_{-k}^z] \\ &+ \overline{P}_{-k}^z[\overline{O},[\overline{O},\overline{P}_k^z]] + [\overline{O},[\overline{O},\overline{P}_k^z]]\overline{P}_{-k}^z|\psi_0\rangle \end{aligned} \tag{3.8}$$

The first term on the right hand side for $\nu = 1$ yields

$$\begin{aligned}&- 2\sum_k V_k^A \langle\psi_0|[\overline{O},\overline{P}_k^z]|\psi_0\rangle\langle\psi_0|[\overline{O},\overline{P}_{-k}^z]|\psi_0\rangle \\ &= \frac{\nu^2}{2A^2}\sum_k V_k^A e^{-\frac{k^2}{2}}\Omega_k^y\Omega_{-k}^y \\ &= \frac{\nu^2}{2A^2}\sum_k V_k^A e^{-\frac{k^2}{2}} m_k^y m_{-k}^y \\ &= \frac{N^2}{2A^2}\int d^2r d^2r' \tilde{V}^A(\mathbf{r}-\mathbf{r}')m^z(\mathbf{r})m^z(\mathbf{r}'), \end{aligned} \tag{3.9}$$

in which $\tilde{V}^A(r)$ is Fourier transform of $V_k^A e^{-k^2/2}$. This term is the Hartree-like charging energy of the bilayer. In the limit of smooth texture of the pseudo-spin field we can expand this term and obtain

$$\beta\int d^2r(m^z)^2 \tag{3.10}$$

where

$$\beta = \frac{\nu^2}{8\pi^2}\int d^2r\tilde{V}^A(r). \tag{3.11}$$

This term is a symmetry breaking term which will force the vector $\mathbf{m}$ to lie in the plane in the ground state.

The second part of the energy in Eq.(3.8) requires a lengthy calculation so we just quote the final result for the antisymmetric Coulomb term[27]

$$\begin{aligned}\delta E^A &= \int d^2r\Big\{\beta_m(m^z)^2 + C[\mathbf{m}] + \frac{\rho_s^z}{2}(\nabla m^z)^2 \\ &- \frac{\rho_s^z}{2}[(\nabla m^x)^2 + (\nabla m^y)^2]\Big\} \end{aligned} \tag{3.12}$$

in which β_m is like a mass for out of plane fluctuations

$$\beta_m = \frac{-\nu}{8\pi^2}\int_0^\infty dk[V^A(k=0) - V^A(k)]kh(k), \tag{3.13}$$

and

$$\rho_s^z = \frac{-\nu}{32\pi^2}\int_0^\infty V^A(k)h(k)k^3 \tag{3.14}$$

and

$$C[\mathbf{m}] = -\frac{e^2 d^2}{16\pi\epsilon}\int \frac{d^2q}{(2\pi)^2}|\mathbf{q}|m^z_{-\mathbf{q}}m^z_{\mathbf{q}}. \tag{3.15}$$

where $h(k) = -e^{-k^2/2}$. Including all the other terms in Eq.(2.60) we obtain[27]

$$\begin{aligned} E_{bilayer}[\mathbf{m}] &= \int d^2r\Big\{\beta_m(m^z)^2 + C[\mathbf{m}] + \frac{\rho_A}{2}(\nabla m^z)^2 \\ &+ \frac{\rho_E}{2}(\nabla m^x)^2 + (\nabla m^x)^2]\Big\} - \frac{\Delta_{SAS}}{4\pi\ell^2}\int d^2r m^x(\mathbf{r}) \\ &- \frac{1}{2}\int d^2r d^2r' V(|\mathbf{r}-\mathbf{r}'|)\delta\rho(\mathbf{r})\delta\rho(\mathbf{r}'). \end{aligned} \tag{3.16}$$

in which

$$\rho_A = \frac{-\nu}{32\pi^2}\int_0^\infty dk V^a(k)h(k)k^3 \tag{3.17}$$

and

$$\rho_E = \frac{-\nu}{32\pi^2}\int_0^\infty dk V^e(k)h(k)k^3. \tag{3.18}$$

The first term, as discussed before, is the inter-layer Hartree energy preferring $m^z = 0$. The second term C vanishes at $d = 0$, this term is an inter-layer exchange energy which tries to align the pseudo-spins in the z-direction. The other two terms are in-plane exchange energies. The next term is the tunneling term which is not derived here but can be easily derived using the tunneling hamiltonian[27]

$$\hat{H}_T = -t\sum_X (c^\dagger_{LX}c_{UX} + c^\dagger_{UX}c_{LX}). \tag{3.19}$$

The tunneling term forces electrons to be in both layers which means it tries to line their pseudo-spin in $\hat{x}$ direction. The last term is the interaction between *pseudo-spin textures*. Pseudo-spin textures similar to skyrmions are present in the bilayer system and because of their electrostatic charge can be detected. In the next section we will explain the details of these objects.

We should note that this effective action can be used to explain the properties of bilayer system at large wavelengths. The quantum fluctuations will redefine the effective parameters and can have dramatic effects for $d/\ell \gg 1$ where a likely phase transition happens into a decoupled system. This transition has indeed been observed in experiment[47].

3.3 Pseudo-spin Topological Excitations

For very small tunneling ($\Delta_{SAS} \ll \Delta_Z$) the real spin of the electrons does not fluctuate and the lowest energy excitations of the bilayer systems are in the pseudo-spin

subband of the lowest Landau level. These excitations are of two types, the neutral pseudo-spin waves and charged topological textures just like spin waves and skyrmions in the quantum Hall ferromagnets. The neutral excitations and topological excitations are gapped. Since only charged excitations can contribute to the conductivity the low-temperature transport coefficients will be activated. We will address the transport in bilayers and its theory in the following chapters.

A very important observation in bilayer systems at total filling factor $\nu_T = 1$ is that the bilayer system exhibits quantized Hall effect[47]. This is expected to be true because from a coherence point of view the electrons in both layers have formed a single coherent state just like when they are in a single layer. This expectation is in fact confirmed by experiments[47]. We can use this fact to set up the same argument as in section 2.2.4 that adiabatic insertion of a flux quantum to the system is equivalent to addition of a quantized amount of charge. On the other hand a pseudo-spin texture would induce a Berry phase in each electron, and this additional Berry phase can be seen as coming from an additional fake magnetic flux which, as we proved in section 2.2.4 is equivalent to an electrostatic charge density. In other words any pseudo-spin texture will have a charge density associated with it :

$$\delta\rho = \frac{-\nu e}{8\pi}\epsilon^{\alpha\beta}\mathbf{p}\cdot\partial_\alpha\mathbf{p}\times\partial_\beta\mathbf{p} \tag{3.20}$$

in which $\mathbf{p}$ is the pseudo-spin vector.

To go further in analogy with quantum Hall ferromagnets, we need to redefine directions: Let's define pseudospin in symmetric state as being in $+\hat{z}$ direction and pseudo-spin in antisymmetric state being in $-\hat{z}$ direction. Using this convention the ground state of the bilayer system is pseudo-spin polarized in the $+\hat{z}$ direction just like spin of quantum Hall ferromagnet. Therefore the topological spin texture will have to be a *pseudo-spin skyrmion*. In a pseudo-spin skyrmion the pseudo-spin in the center is in antisymmetric($-\hat{z}$) state and it smoothly changes its direction toward the boundaries and finally turns into the symmetric($+\hat{z}$) direction which is the lower energy region. In a more systematic way we can define

$$\begin{aligned}\tilde{p}_z &= \rho_{SS} - \rho_{AA}\\ \tilde{p}_x + i\tilde{p}_y &= \rho_{SA}\end{aligned} \tag{3.21}$$

in which $\rho_{\alpha\beta} = \langle c^\dagger_\alpha c_\beta\rangle$. The vector field $\tilde{\mathbf{p}}$ then has the distribution of a skyrmion. On the other hand it will be more useful in the future to work in the (U,L) basis

$$\tilde{\mathbf{c}}^\dagger = \mathbf{M}\cdot\mathbf{c}^\dagger \tag{3.22}$$

State	Basis	Vector Representation	Topology
Bimeron	$\|U\rangle$,$\|L\rangle$	$p_x + ip_y = \rho_{UL}$, $p_z = \rho_{UU} - \rho_{LL}$	ZY-plane vorticity
Pseudo-spin Skyrmion	$\|S\rangle$,$\|A\rangle$	$\tilde{p}_x + i\tilde{p}_y = \rho_{SA}$, $\tilde{p}_z = \rho_{SS} - \rho_{AA}$	XY-plane vorticity

Table 3.1: Comparison between two representations of a bimeron.

in which

$$\tilde{\mathbf{c}}^\dagger = \begin{pmatrix} c_S^\dagger \\ c_A^\dagger \end{pmatrix}, \mathbf{M} = \begin{pmatrix} \frac{1}{\sqrt{2}} & \frac{1}{\sqrt{2}} \\ \frac{1}{\sqrt{2}} & \frac{-1}{\sqrt{2}} \end{pmatrix}, \mathbf{c}^\dagger = \begin{pmatrix} c_U^\dagger \\ c_L^\dagger \end{pmatrix}. \tag{3.23}$$

The densities are defined as

$$\underline{\rho} = \mathbf{c}^\dagger \cdot \mathbf{c} \tag{3.24}$$

Now we can rotate the pseudo-spin vectors to the (U,L) basis by rotating the densities

$$\underline{\rho} = \mathbf{M}^\dagger \cdot \underline{\tilde{\rho}} \cdot \mathbf{M}. \tag{3.25}$$

Note that $\mathbf{M}$ is a unitary matrix. Using the fact that $\rho_{\alpha\beta} = \rho^*_{\beta\alpha}$ and Eq.(3.6) we can see that

$$\begin{aligned} p_z &= \tilde{p}_x \\ p_x &= \tilde{p}_z \\ p_y &= -\tilde{p}_y \end{aligned} \tag{3.26}$$

This rotation of pseudo-spin vectors will change the field distribution to a new one that does not have in-plane vortex symmetry (Fig.3.10) however it is still the same state as pseudo-spin skyrmion and possesses the same vorticity number. Most of the time this topological excitation is called a *Bimeron*. Only later on it will turn out that this object can split up under special circumstances into two topological objects called *merons*. In order to study merons it is necessary to use the (U,L) basis.

We can summarize the pseudo-spin skyrmion and bimeron representation of a charged topological excitation of a bilayer system as in table 3.1.

3.4 Microscopic Calculation of Texture Lattices

Similar to quantum Hall ferromagnets for total filling factors slightly away from $\nu_T = 1$, the ground state of the bilayer system will have a finite density of charged

topological objects. Because of the interaction between these objects the lowest energy configuration will be a square lattice[48]. To study the various properties of these states including charge and spin density in each layer, it is necessary to perform microscopic calculations. Also, as we will see in the next sections, it will turn out that a pure pseudo-spin analysis of the excitations of bilayer systems is not sufficient to explain all the experimental observations and a full spin and pseudo-spin analysis is needed for more investigation. Evidently such an analysis requires a more microscopic calculation than just the effective action method. The most important investigation performed in this dissertation is the numerical calculation of the energy of the electrons and excitations and also the spin and charge density of the 2DEG in the lattice states of bilayer systems slightly away from $\nu_T = 1$ using the Hartree-Fock approximation. In this section we will explain the method and the basic microscopic theory for calculating the energy and charge density of electrons in pseudo-spin texture lattices. In the next section we will use the same technique to calculate the real spin density of electron gas in other texture lattice states of bilayer system.

In the limit of clean bilayer system at total filling factors close but not equal to $\nu_T = 1$ we assume the lowest energy state of the bilayer system is a square lattice of topological textures. It will turn out that there is more than one type of pseudo-spin texture lattices depending on the number of extra electrons chosen per unit cell(density) and depending on the important parameters of the system including tunneling gap Δ_{SAS}, layer separation d/ℓ, interlayer bias Δ_b and total filling factor. Because of the interaction between these textures only one type of lattice has the lowest energy per electron in various parts of parameter space.

Following previous works[24] we start by finding the equation of motion for the Green's function in Hartree-Fock approximation. Throughout this calculation we use the Landau gauge $\mathbf{A} = (0, Bx, 0)$ for which the wave function of the free electron in the lowest Landau level is

$$\psi_X(\mathbf{r}) = \frac{1}{\sqrt{L_y \ell \pi^{1/2}}} e^{iXy/\ell^2} e^{-(x-X)/2\ell^2}. \tag{3.27}$$

The Green's function is defined as

$$G_{\alpha\beta}(XX', \tau) = -\hat{T}\langle c_{\alpha X}(\tau) c^\dagger_{\beta X'}(0)\rangle \tag{3.28}$$

in which $c^\dagger_{\alpha X}$ is the creation operator that creates an electron in the lowest Landau level with guiding center X in the subband α, and τ is the imaginary time. For pure pseudo-spin excitations $\alpha = U, L$ for upper and lower layers.

The equation of motion for the Green's function is obtained using the Hamiltonian of the interacting electron system in the lowest Landau level:

$$\begin{aligned}\hat{\mathcal{H}} &= \frac{1}{2S}\sum_{\mathbf{q}}\sum_{\{X\}}\sum_{\alpha'\beta'} V_{\alpha'\beta'}(\mathbf{q}) M^{\alpha'}_{\mathbf{q}}(X_1|X_4) M^{\beta'}_{-\mathbf{q}}(X_2|X_3) c^{\dagger}_{\alpha' X_1} c^{\dagger}_{\beta' X_2} c_{\beta' X_3} c_{\alpha' X_4} \\ &- \frac{\Delta_{SAS}}{2}\sum_{X,\sigma}(c^{\dagger}_{U,X}c_{L,X} + c^{\dagger}_{L,X}c_{U,X}) \end{aligned} \tag{3.29}$$

in which

$$M^{\alpha}_{\mathbf{q}}(X'|X) = e^{iq_x(X+X')/2}\delta_{X',X+q_y\ell^2} \tag{3.30}$$

and the Coulomb interaction is represented by

$$\begin{aligned} V_{\alpha\beta}(q) &= \frac{2\pi e^2}{q} e^{-q^2\ell^2/2} \qquad \alpha,\beta = \text{same layer} \\ &= \frac{2\pi e^2}{q} e^{-qd-q^2\ell^2/2} \qquad \alpha,\beta = \text{different layer} \end{aligned} \tag{3.31}$$

by finding the time derivative as follows

$$\frac{\partial G_{\alpha\beta}}{\partial\tau} = -\hat{T}\langle\frac{\partial}{\partial\tau}c_{\alpha X}(\tau)c^{\dagger}_{\beta X'}(0)\rangle - \delta_{\alpha\beta}\delta_{XX'}\delta(\tau). \tag{3.32}$$

The Heisenberg equation of motion for the annihilation operator is

$$\begin{aligned}\frac{\partial}{\partial\tau}c_{\alpha X}(\tau) &= \Big[\hat{\mathcal{H}} - \mu\hat{\mathcal{N}}, c_{\alpha X}\Big] = \Big[\hat{\mathcal{H}}, c_{\alpha X}\Big] - \mu\Big[\hat{\mathcal{N}}, c_{\alpha X}\Big] = \\ &= \frac{1}{2S}\sum_{q,X,\alpha'\beta'} V_{\alpha'\beta'}(q) M^{\alpha'}_{q}(X_1|X_4) M^{\beta'}_{-q}(X_2|X_3)\Big[c^{\dagger}_{\alpha' X_1}c^{\dagger}_{\beta' X_2}c_{\beta' X_3}c_{\alpha' X_4}, c_{\alpha X}\Big] \\ &- \frac{\Delta_{SAS}}{2}\sum_{X'}\Big[c^{\dagger}_{U,X'}c_{L,X'} + c^{\dagger}_{L,X'}c_{U,X'}, c_{\alpha X}\Big] + \mu c_{\alpha X} \\ &= \frac{1}{2S}\sum_{q,X,\alpha'\beta'} V_{\alpha'\beta'}(q) M^{\alpha'}_{q}(X_1|X_4) M^{\beta'}_{-q}(X_2|X_3)\Big[c^{\dagger}_{\alpha' X_1}c^{\dagger}_{\beta' X_2}, c_{\alpha X}\Big]c_{\beta' X_3}c_{\alpha' X_4} \\ &- \frac{\Delta_{SAS}}{2}\sum_{X'}\Big[-\{c^{\dagger}_{UX'}, c_{\alpha X}\}c_{LX'} - \{c^{\dagger}_{LX'}, c_{\alpha X}\}c_{UX'}\Big] + \mu c_{\alpha X}. \end{aligned} \tag{3.33}$$

in which $\hat{\mathcal{N}} = \sum_{X\alpha} c^{\dagger}_{\alpha X}c_{\alpha X}$. Using the identities $[AB,C] = A[B,C] + [A,C]B$ and $[AB,C] = A\{B,C\} - \{C,A\}B$ we can simplify the above

$$\begin{aligned}\frac{\partial}{\partial\tau}c_{\alpha X} &= \frac{1}{2S}\sum_{q,X,\alpha'\beta'} V_{\alpha'\beta'}(q) M^{\alpha'}_{q}(X_1|X_4) M^{\beta'}_{-q}(X_2|X_3) \times \\ &\times \ (c^{\dagger}_{\alpha' X_1}\delta_{\beta'\alpha}\delta_{XX_2} - c^{\dagger}_{\beta' X_2}\delta_{\alpha\alpha'}\delta_{XX_1})c_{\beta' X_3}c_{\alpha' X_4} \\ &+ \frac{\Delta_{SAS}}{2}\sum_{\sigma}(\delta_{U,\alpha}c_{LX} + \delta_{L,\alpha}c_{UX}) + \mu c_{\alpha X}. \end{aligned} \tag{3.34}$$

Inserting the above into Eq.(3.32) we obtain

$$\begin{aligned}
\frac{\partial G_{\alpha\beta}(XX')}{\partial\tau} &= -\delta_{\alpha\beta}\delta_{XX'}\delta(\tau) - \frac{1}{2S}\sum_{q,X,\alpha'\beta'} V_{\alpha'\beta'}(q) M_q^{\alpha'}(X_1|X_4) M_{-q}^{\beta'}(X_2|X_3) \times \\
&\times \Big[\hat{T}\Big\langle c^\dagger_{\alpha' X_1}(\tau) c_{\beta' X_3}(\tau) c_{\alpha' X_4}(\tau) c^\dagger_{\beta X'}(0)\Big\rangle \delta_{\alpha\beta'}\delta_{XX_2} \\
&- \hat{T}\Big\langle c^\dagger_{\beta' X_2}(\tau) c_{\beta' X_3}(\tau) c_{\alpha' X_4}(\tau) c^\dagger_{\beta X'}(0)\Big\rangle \delta_{\alpha\alpha'}\delta_{XX_1}\Big] \\
&+ \frac{\Delta_{SAS}}{2}\Big[-\delta_{U,\alpha}\hat{T}\Big\langle c_{LX} c^\dagger_{\beta X'}(0)\Big\rangle - \delta_{L,\alpha}\hat{T}\Big\langle c_{UX} c^\dagger_{\beta X'}(0)\Big\rangle\Big] \\
&- \mu\hat{T}\Big\langle c_{\alpha X} c^\dagger_{\beta X'}(0)\Big\rangle. \qquad (3.35)
\end{aligned}$$

We approximate the four point correlation functions above up to the tree diagram level(Hartree-Fock approximation)

$$\begin{aligned}
\hat{T}\Big\langle c^\dagger_{\alpha' X_1}(\tau) c_{\beta' X_3}(\tau) c_{\alpha' X_4}(\tau) c^\dagger_{\beta X'}(0)\Big\rangle &= \hat{T}\Big\langle c^\dagger_{\alpha' X_1}(\tau) c_{\beta' X_3}(\tau)\Big\rangle\langle c_{\alpha' X_4}(\tau) c^\dagger_{\beta X'}(0)\Big\rangle \\
&- \hat{T}\Big\langle c^\dagger_{\alpha' X_1}(\tau) c_{\alpha' X_4}(\tau)\Big\rangle\langle c_{\beta' X_3}(\tau) c^\dagger_{\beta X'}(0)\Big\rangle \\
\hat{T}\Big\langle c^\dagger_{\beta' X_2}(\tau) c_{\beta' X_3}(\tau) c_{\alpha' X_4}(\tau) c^\dagger_{\beta X'}(0)\Big\rangle &= \hat{T}\Big\langle c^\dagger_{\beta' X_2}(\tau) c_{\beta' X_3}(\tau)\Big\rangle\langle c_{\alpha' X_4}(\tau) c^\dagger_{\beta X'}(0)\Big\rangle \\
&- \hat{T}\Big\langle c^\dagger_{\beta' X_2}(\tau) c_{\alpha' X_4}(\tau)\Big\rangle\langle c_{\beta' X_3}(\tau) c^\dagger_{\beta X'}(0)\Big\rangle.
\end{aligned} \qquad (3.36)$$

Single particle densities can be defined as

$$\rho_{\alpha\beta}(XX') = \langle c^\dagger_{\alpha' X} c_{\beta' X'}\rangle. \qquad (3.37)$$

Using the above definition and Eq.(3.36) in Eq.(3.35) we find

$$\begin{aligned}
\frac{\partial G_{\alpha\beta}(XX')}{\partial\tau} &= -\delta_{\alpha\beta}\delta_{XX'}\delta(\tau) - \frac{1}{2S}\sum_{q,X,\alpha'\beta'} V_{\alpha'\beta'}(q) M_q^{\alpha'}(X_1|X_4) M_{-q}^{\beta'}(X_2|X_3) \times \\
&\times \Big\{[\rho_{\alpha'\beta'}(X_1X_3)(-G_{\alpha'\beta}(X_4X')) + \rho_{\alpha'\alpha'}(X_1X_4) G_{\beta'\beta}(X_3X')]\delta_{\alpha\beta'}\delta_{XX_2} + \\
&- [\rho_{\beta'\beta'}(X_2X_3)(-G_{\alpha'\beta}(X_4X')) + \rho_{\beta'\alpha'}(X_2X_4) G_{\beta'\beta}(X_3X')]\delta_{\alpha\alpha'}\delta_{XX_1}\Big\} + \\
&+ \frac{\Delta_{SAS}}{2}\Big[\delta_{U,\alpha} G_{L,\beta}(XX') + \delta_{L,\alpha} G_{U,\beta}(XX')\Big] + \\
&+ \mu G_{\alpha\beta}(XX'). \qquad (3.38)
\end{aligned}$$

We can find the textured lattice solutions of the above equation using Fourier transforms. Because we are in the Landau gauge, it is more convenient to define a special Fourier transform in which only one direction is transformed

$$G_{\alpha\beta}(\mathbf{q},\tau) = \frac{1}{g}\sum_{XX'} G_{\alpha\beta}(XX',\tau) e^{-iq_x(X+X')/2}\delta_{X',X-q_y\ell^2} \qquad (3.39)$$

$$\rho_{\alpha\beta}(\mathbf{q}) = \frac{1}{g}\sum_{XX'}\rho_{\alpha\beta}(XX')e^{-iq_x(X+X')/2}\delta_{X',X+q_y\ell^2}. \tag{3.40}$$

in which $g = S/2\pi\ell^2$ is the degeneracy of the Landau levels. Using this transformation the equation of motion 3.38 will be

$$\begin{aligned}
-i\omega G_{\alpha\beta}(\mathbf{k}) &= -\delta_{\mathbf{k},0}\delta_{\alpha\beta} - \frac{g}{S}\sum_{\mathbf{q}',\alpha',\beta'} V_{\alpha'\beta'}(\mathbf{k}-\mathbf{q}')\rho_{\beta'\beta'}(\mathbf{k}-\mathbf{q}')G_{\alpha'\beta}(\mathbf{q}')e^{i\frac{\ell^2}{2}\mathbf{k}\times\mathbf{q}'}\delta_{\alpha\alpha'} + \\
&+ \frac{1}{S}\sum_{\alpha',\beta';\mathbf{q},\mathbf{q}'} V_{\alpha'\beta'}(\mathbf{q})e^{i\ell^2\mathbf{q}\times(\mathbf{k}-\mathbf{q}')}\rho_{\beta'\alpha'}(\mathbf{k}-\mathbf{q}')G_{\beta'\beta}(\mathbf{q}')e^{i\frac{\ell^2}{2}\mathbf{k}\times\mathbf{q}'}\delta_{\alpha\alpha'} \\
&+ \frac{\Delta_{SAS}}{2}\Big[\delta_{U,\alpha}G_{L,\beta}(\mathbf{k}) + \delta_{L,\alpha}G_{U,\beta}(\mathbf{k})\Big] + \mu G_{\alpha\beta}(\mathbf{k}).
\end{aligned} \tag{3.41}$$

in which ω is a Matsubara frequency. The third term in the above equation has a sum over $\mathbf{q}$ that is equivalent to the following function

$$\begin{aligned}
I_{\alpha\beta}(\mathbf{G}) &\equiv \frac{1}{S}\sum_{\mathbf{q}} V_{\alpha\beta}(\mathbf{q})e^{i\ell^2\mathbf{q}\times\mathbf{G}} \\
&= \int \frac{d^2q}{(2\pi)^2}V_{\alpha\beta}(q)e^{i\ell^2\mathbf{q}\times\mathbf{G}} \\
&= \frac{e^2}{2\pi}\int dqd\theta e^{-q^2\ell^2/2}e^{i\ell^2qG\sin\theta} \quad (\alpha,\beta \text{ the same layer}) \\
&= \frac{e^2}{2\pi}\int dqd\theta e^{-q^2\ell^2/2}e^{i\ell^2qG\sin\theta}e^{-qd} \quad (\alpha,\beta \text{ different layer}).
\end{aligned} \tag{3.42}$$

For the same layer the above function is

$$\begin{aligned}
I^s_{\alpha\beta}(\mathbf{G}) &= e^2\int_0^\infty dqJ_0(\ell^2qG)e^{-q^2\ell^2/2} \\
&= e^2/\ell\sqrt{\frac{\pi}{2}}I_0(G^2/4\ell^2)e^{-G^2/4\ell^2}.
\end{aligned} \tag{3.43}$$

in which I_0 is the modified Bessel function of the zeroth order and for different layers we will have

$$\begin{aligned}
I^d_{\alpha\beta}(\mathbf{G}) &= e^2\int_0^\infty dqJ_0(\ell^2qG)e^{-q^2\ell^2/2}e^{-qd} \\
&= e^2/\ell\int_0^\infty dq'J_0(G'q')e^{-q'^2/2}e^{-q'd/\ell}.
\end{aligned} \tag{3.44}$$

In which we have scaled the wavevectors with $1/\ell$. Finally the equation of motion for the Green function becomes:

$$\begin{aligned}
(-i\omega-\mu)G_{\alpha\beta}(\mathbf{k}) &= -\delta_{\mathbf{k},\mathbf{0}}\delta_{\alpha\beta} - U_{\alpha\alpha'}(\mathbf{k},\mathbf{k}')G_{\alpha'\beta}(\mathbf{k}') = \\
&= -\delta_{\mathbf{k},\mathbf{0}}\delta_{\alpha\beta} - e^{i\frac{\ell^2}{2}\mathbf{k}\times\mathbf{k}'}W_{\alpha\alpha'}(\mathbf{k}-\mathbf{k}')G_{\alpha'\beta}(\mathbf{k}').
\end{aligned} \tag{3.45}$$

in which there is summation over repeated indices and

$$U_{\alpha\alpha'}(\mathbf{k},\mathbf{k}') = e^{i\frac{\ell^2}{2}\mathbf{k}\times\mathbf{k}'}W_{\alpha\alpha'}(\mathbf{k}-\mathbf{k}') \tag{3.46}$$

where W is defined as follows:

$$\begin{aligned} W_{\alpha\alpha'}(\mathbf{G}) &= \frac{\delta_{\alpha\alpha'}}{2\pi\ell^2}\sum_{\beta'} V_{\alpha\beta'}(\mathbf{G})\rho_{\beta'\beta'}(\mathbf{G}) - I_{\alpha\alpha'}(\mathbf{G})\rho_{\alpha'\alpha}(\mathbf{G}) + \\ &- \frac{\Delta_{SAS}}{2}\delta_{\mathbf{G},0}(\sigma_x)_{\alpha\alpha'} \end{aligned} \tag{3.47}$$

in which σ_x is the Pauli spin matrix. In this equation the first term represents intra-layer direct interactions while the second term represents the inter-layer ($I = I^d$) and intra-layer ($I = I^s$) exchange interaction between electrons. To avoid divergencies due to the self-interaction of the electron gas we should have considered an interaction term with a uniform density of positive ion background in the beginning. However we can directly include that effect here by setting $V_{\alpha\beta}(\mathbf{G}=0) = 0$ for α, β representing the same layer. This includes the effect of the positive background to each layer separately. In addition each layer will interact with the electric field of the positive uniform charge background of the other layer which is proportional to the interlayer separation so we set $V_{\alpha\beta}(G=0) = -d/\ell$ when $\alpha \neq \beta$.

Equation (3.45) can be solved for densities by diagonalizing the matrix U. Suppose $A^\alpha_\lambda(\mathbf{k})$ is an eigenvector of U with eigenvalue Ω_λ

$$\sum_\beta U_{\alpha\beta}(\mathbf{k},\mathbf{k}')A^\beta_\lambda(\mathbf{k}') = \Omega_\lambda A^\alpha_\lambda(\mathbf{k}). \tag{3.48}$$

We expand the Green's function in the basis of these eigenvectors

$$G_{\alpha\beta}(\mathbf{k}, i\omega) = \sum_\lambda c^\beta_\lambda(\omega)A^\alpha_\lambda(\mathbf{k}) \tag{3.49}$$

with the coefficients being

$$c^\beta_\lambda = \frac{\overline{A^\beta_\lambda}(\mathbf{k}=0)}{i\omega + \mu - \Omega_\lambda} \tag{3.50}$$

which yields

$$G_{\alpha\beta}(\mathbf{k}, i\omega) = \sum_\lambda \frac{\overline{A^\beta_\lambda}(\mathbf{k}=0)A^\alpha_\lambda(\mathbf{k})}{i\omega + \mu - \Omega_\lambda}. \tag{3.51}$$

where in the above overbar means complex conjugate. Now we can find densities using the fact that

$$\begin{aligned} \rho_{\alpha\beta}(\mathbf{k}) &= G_{\beta\alpha}(\mathbf{k}, \tau \to 0^-) \\ &= \sum_\lambda\sum_\omega \frac{\overline{A^\alpha_\lambda}(\mathbf{k}=0)A^\beta_\lambda(\mathbf{k})}{i\omega + \mu - \Omega_\lambda} \end{aligned} \tag{3.52}$$

in which the sum over Matsubara frequencies ω will yield the Fermi function

$$\rho_{\alpha\beta}(\mathbf{k}) = \sum_{\lambda} \overline{A^{\alpha}_{\lambda}}(\mathbf{k}=0) A^{\beta}_{\lambda}(\mathbf{k}) f_B(\mu - \Omega_\lambda) \tag{3.53}$$

where $f_B(x) = \frac{1}{1+e^{\beta x}}$ and $\beta = 1/k_B T$. The chemical potential μ can be found using the fact that

$$\sum_{\alpha} \rho_{\alpha\alpha}(\mathbf{k}=0) = \nu. \tag{3.54}$$

At zero temperature the equation (3.53) will become

$$\rho_{\alpha\beta}(\mathbf{k}) = \sum_{\Omega_\lambda < \mu} \overline{A^{\alpha}_{\lambda}}(\mathbf{k}=0) A^{\beta}_{\lambda}(\mathbf{k}) \tag{3.55}$$

in which only a finite set of eigenvalues of matrix U are being used.

To set up the bimeron lattice structure we assume that there is one extra electron per unit cell of a square lattice so the lattice constant would be $a = \sqrt{2\pi\ell^2/|\nu - 1|}$. The lattice vectors are then $\mathbf{a}_1 = a\hat{x}$ and $\mathbf{a}_2 = a\hat{y}$. Equation (3.45) has many solutions for different ranges of parameters. To find each one of them in an iterative method we start with a simple guess that obeys the desired symmetries of the solution. Usually, for starting densities, only the first few shells in reciprocal lattice space are non-zero.

For a lattice of bimerons as was mentioned before we should note that the in-plane component of bimeron pseudo-spin has *vortex symmetry* like skyrmions, which imposes the following restriction on the space of solutions

$$\rho_{SA}(\mathcal{R}_\varphi \mathbf{r}) = e^{i\varphi} \rho_{SA}(\mathbf{r}). \tag{3.56}$$

in which $\varphi = \pm\pi/2$ for a vortex(anti-vortex) with winding number $n = \pm 1$. Note that this symmetry is true only when densities are calculated in the S, A basis.

Using the densities one can calculate the energy per electron of the texture lattice $E = \langle\hat{\mathcal{H}}\rangle/N$ in the Hartree-Fock approximation

$$\begin{aligned} \langle\hat{\mathcal{H}}\rangle &= \frac{1}{2S} \sum_{\mathbf{q}} \sum_{\{X\}} \sum_{\alpha'\beta'} V_{\alpha'\beta'}(\mathbf{q}) M^{\alpha'}_{\mathbf{q}}(X_1|X_4) M^{\beta'}_{-\mathbf{q}}(X_2|X_3) \Big\langle c^{\dagger}_{\alpha' X_1} c^{\dagger}_{\beta' X_2} c_{\beta' X_3} c_{\alpha' X_4} \Big\rangle + \\ &- \frac{\Delta_{SAS}}{2} \sum_{X} \Big[\langle c^{\dagger}_{UX} c_{L,X} \Big\rangle + \Big\langle c^{\dagger}_{LX} c_{UX} \Big\rangle \Big]. \end{aligned} \tag{3.57}$$

in Hartree-Fock approximation

$$\langle\hat{\mathcal{H}}\rangle = \frac{1}{2S} \sum_{\mathbf{q}} \sum_{\{X\}} \sum_{\alpha'\beta'} V_{\alpha'\beta'}(\mathbf{q}) M^{\alpha'}_{\mathbf{q}}(X_1|X_4) M^{\beta'}_{-\mathbf{q}}(X_2|X_3) \Big[\rho_{\alpha'\beta'}(X_1 X_3) \rho_{\beta'\alpha'}(X_2 X_4) +$$

$$- \quad \rho_{\alpha'\alpha'}(X_1X_4)\rho_{\beta'\beta'}(X_2X_3)\Big] - \frac{\Delta_{SAS}}{2}\sum_X \Big[\rho_{U,L}(X,X) + \rho_{L,U}(X,X)\Big]. \tag{3.58}$$

in which the first term is the sum of inter-layer and intra-layer correlation energies while the second term is the sum of inter-layer and intra-layer exchange energies. The Fourier transform of the above is

$$\begin{aligned}\langle\hat{\mathcal{H}}\rangle &= \frac{1}{2}\sum_{\mathbf{k},\alpha,\beta} I_{\alpha\beta}(\mathbf{k})\rho_{\alpha\beta}(\mathbf{k})\rho_{\beta\alpha}(-\mathbf{k}) - \frac{1}{2}\sum_{\alpha\beta} V_{\alpha\beta}(\mathbf{q})\rho_{\alpha\alpha}(-\mathbf{q})\rho_{\beta\beta}(\mathbf{q}) \\ &- \frac{\Delta_{SAS}}{2}\Big[\rho_{U,L}(0) + \rho_{L,U}(0)\Big].\end{aligned} \tag{3.59}$$

Using the above we can also calculate the energy increase of a single excitation (E_{ex}) like a bimeron from the uniform background when the density deviates from $\nu_T = 1$

$$E_{texture} = \frac{\nu_T}{|1-\nu_T|}\Big[E - E_0(d)\Big] \tag{3.60}$$

in which $E_0(d)$ is the uniform background energy at $\nu_T = 1$ calculated by minimizing the energy (3.59)

$$\begin{aligned}E_{texture} &= -\frac{\Delta_{SAS}}{2} - \frac{1}{4}\Big[I^s(\mathbf{q}=0) + I^d(\mathbf{q}=0)\Big] \\ &= -\frac{\Delta_{SAS}}{2} - \frac{1}{4}\Big[\sqrt{\frac{\pi}{2}} + \sqrt{\frac{\pi}{2}}e^{d^2/2\ell^2}Erf(\frac{d/\ell}{\sqrt{2}})\Big].\end{aligned} \tag{3.61}$$

in which Erf is the error function. In the limit of vanishing bimeron density ($\nu_T \to 1$), the quantity $E_{texture}$ is the so-called neutral excitation energy, related to the chemical potential $\mu^{\pm}$ at densities just above and below the critical density $\nu_T = 1$, through the relation

$$\mu^{\pm} = \pm E_{texture} + E_0(d). \tag{3.62}$$

In which plus and minus signs are for excitations above and below $\nu_T = 1$. As a consequence of particle-hole symmetry which applies in the thermodynamic limit, the chemical potential satisfies the relation

$$\mu^+ + \mu^- = 2\Big[E_0(d) + \frac{\Delta_{SAS}}{2}\Big]. \tag{3.63}$$

It is therefore possible to extract the energy gap for a single charged excitation (the charge gap) from the knowledge of $E_{texture}$ alone

$$\Delta = \mu^+ - \mu^- = 2E_{texture} + 2\Big[E_0(d) - E_0(d=0)\Big]. \tag{3.64}$$

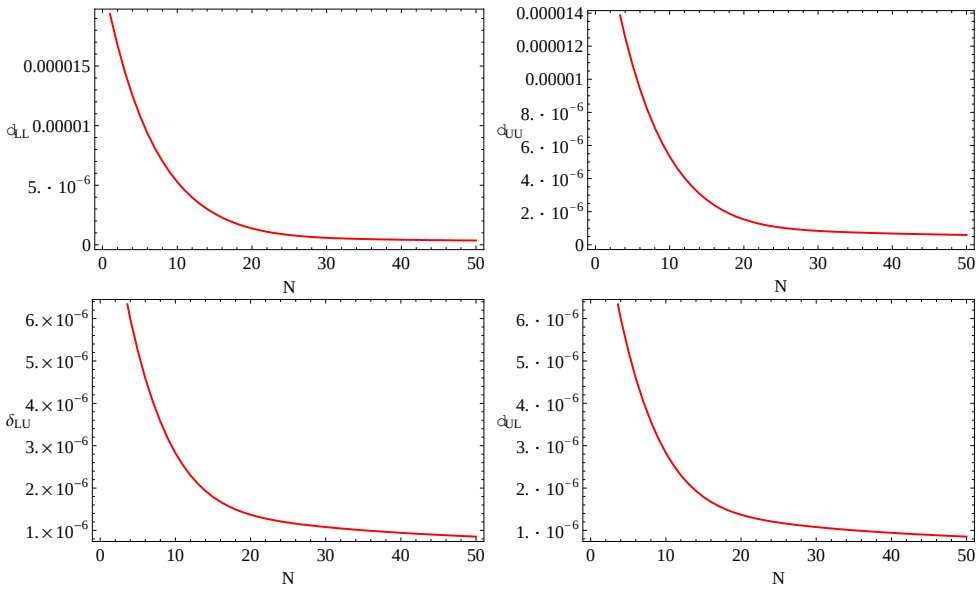

Figure 3.7: Four typical convergence factors for the last 50 iteration for densities of a meron-meron lattice at $d/\ell = 0.8$ and zero tunneling.

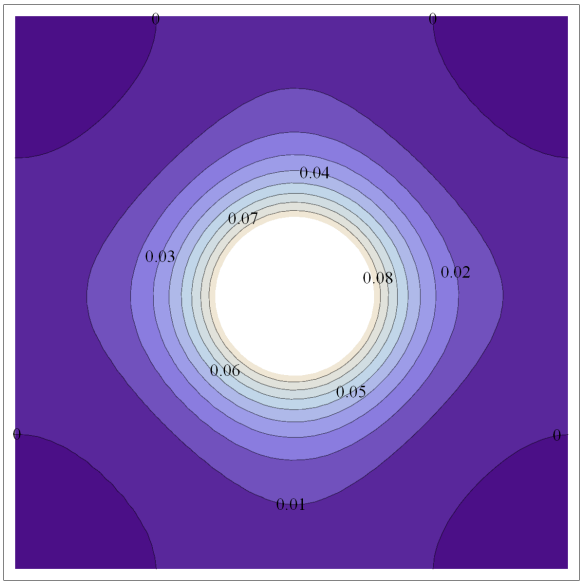

Figure 3.8: Contour plot of a bimeron at interlayer separation $d/\ell = 0$(The SU(2) symmetry of the Coulomb potential is not yet broken) and zero tunneling at $\nu_T = 1.02$. The contour labels are values of density in units of $1/2\pi\ell^2$

3.5 Numerical Results

To numerically solve equation (3.45) for the densities $\rho_{\alpha\beta}(\mathbf{G})$ we use a finite number of reciprocal lattice vectors $|\mathbf{G}| < G_{max}$. Using the symmetries explained above we guess an appropriate set of densities for the first few shells in reciprocal lattice vector space to calculate the matrix U (Eq. 3.46). This matrix is then diagonalized. Using the resulting eigenvectors the densities will be calculated (Eq. 3.55) to calculate U again. This iteration over ρ's continues until the solutions do not change. Figure (3.7) illustrates convergence factors for a single run of iterations. The convergence factors are defined as

$$\delta^2_{\alpha\beta} = \frac{\sum_G |\rho_{\alpha\beta}(\mathbf{G}) - \rho'_{\alpha\beta}(\mathbf{G})|^2}{\sum_G |\rho_{\alpha\beta}(\mathbf{G})|^2} \tag{3.65}$$

in which ρ''s are the solutions after ρ's in the iterative process. The behavior of δ factor is usually of three types: divergent, convergent and unstable. A divergent δ usually increases with increasing iteration number. A convergent δ decreases with increasing the iteration number (figure 3.7) usually down to around 10^{-6} or lower. The unstable δ usually converges first and very quickly rises up with increasing iteration number. We only accept the convergent solutions.

For very dilute lattices G_{max} increases and usually the self-consistent iterative method does not converge for filling factors $|1 - \nu_T| \leqslant 0.015$. Figure 3.8 is a contour plot of charge density of a bimeron in the center of a unit cell of a square lattice at filling factor $\nu_T = 1.02$ and layer separation $d = 0$ and at zero tunneling. In this lattice there is one bimeron(one extra electron) per unit cell so the minimum distance between two bimerons is of the order of 17.7ℓ. As we can see the charge density has circular symmetry around the center. The figure 3.9(a),(b) show the XY and Z-component of the pseudo-spin in the (S,A) basis respectively. In this picture the pseudo-spin vector at the center is pointing out of the plane $(-\hat{z})$ (note that P_z is negative at the center) representing electron being in the antisymmetric band and gradually tilts away toward the boundary where it eventually points in the symmetric $(+\hat{z})$ direction. Figure 3.10 represents the same texture. The pseudo-spin vectors are now calculated in the (U,L) basis (see section 3.3). The upper figure represents the XY components of the pseudo-spin vectors. The direction perpendicular to the page $(+\hat{z})$ now represents pseudo-spin being up, in other words electron's wave function is localized in the upper layer. The vectors lying in the plane perpendicular to $\hat{z}$ are distributed in both layers. In this representation the bimeron consists of a vortex and an anti-vortex that are connected by a string of over-turned pseudo-spins. They are

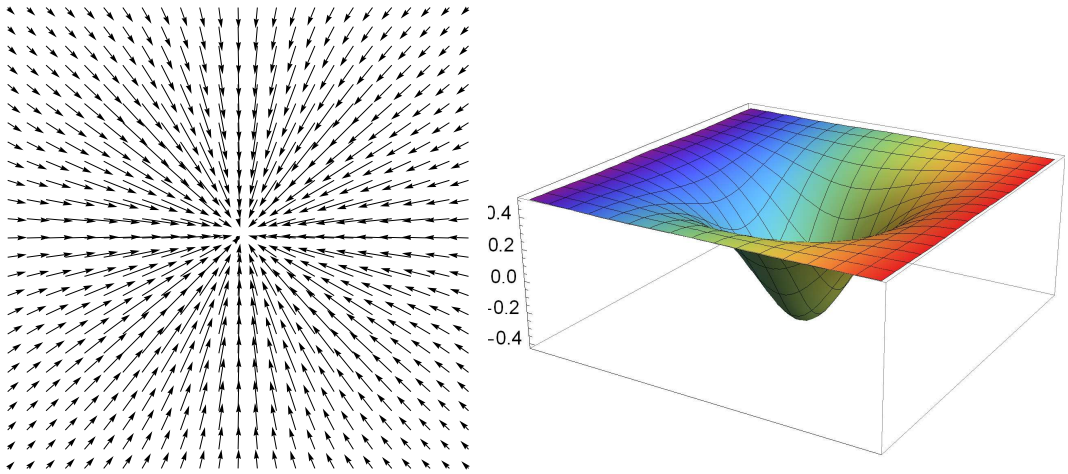

(a) (b)

Figure 3.9: (a) In-plane components of a bimeron in (S,A) basis at $\nu_T = 1.02$, zero tunneling and zero layer separation. The length of the vectors is proportional to the magnitude of $|\rho_{SA}|$ at each point. (b)Z-component of the same bimeron in (S,A) basis: $\rho_{SS} - \rho_{AA}$ in units of $1/2\pi\ell^2$. The colors do not have a physical interpretation.

over-turned from the majority direction which is to the right ($+\hat{x}$) representing equal distribution in both upper layer and lower layer. The lower left of the picture shows a profile of the z-component of the pseudo-spin ($= \rho_U - \rho_L$). Each of the vortices in the bimeron has a local charge imbalance at the center but in the opposite direction.

At $d = 0$ the bimeron texture is equivalent to a skyrmion texture because the Hamiltonian has the full SU(2) symmetry. By increasing the separation between the layers the bimeron is still a solution to the ground state at $\nu_T = 1.02$. Figure 3.11 shows a contour plot of the charge density of a bimeron at $d = 0.2\ell$ and zero tunneling. The circular symmetry is clearly broken. Figure 3.12 shows the same texture again in the (U,L) basis.

This change in shape of the bimeron charge density continues in higher separations so that when we get to $d = 0.8\ell$ the charge density clearly starts to split. Figure 3.13 shows the bimeron charge density at $d = 0.8\ell$ and zero tunneling. The charge density has split. This happens because at higher separations the inter-layer exchange is weak and fails to keep the bimeron from spreading. On the other hand the interaction between bimerons in the lattice prevents bimerons from expanding in a symmetric way in order to keep each other from overlapping. Figure 3.14 shows a bimeron pseudo-spin distribution at $d/\ell = 0.8$. As we can see the constituent vortices are moved away from each other so that the z-component of their pseudo-spin at the

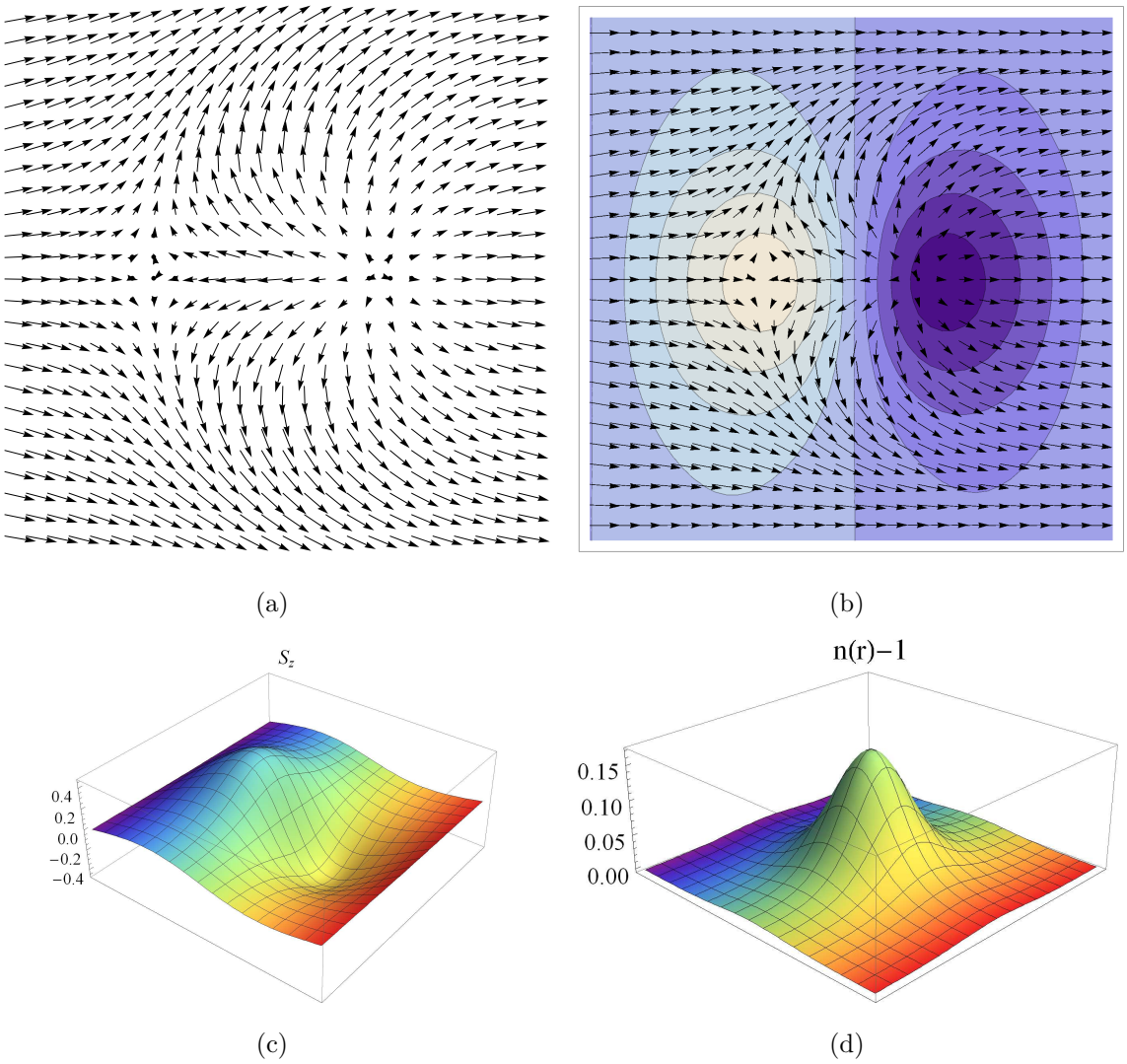

Figure 3.10: (a)In-plane components of the pseudo-spin of a bimeron in (U,L) basis at $\nu_T = 1.02$, zero tunneling and zero layer separation. The length of the vectors is proportional to the magnitude of $|\rho_{UL}|$ at each point. The plot shows the two merons bound together in this excitation. (b) The In-plane pseudo-spin field (vectors) and Z-component of the same set of vectors(contour). (c) Z-component of the same bimeron in (U,L) basis: $\rho_{UU} - \rho_{LL}$ in units of $1/2\pi\ell^2$. (d) 3D plot of the excess density of the bilayer system due to the same bimeron in units of $1/2\pi\ell^2$.

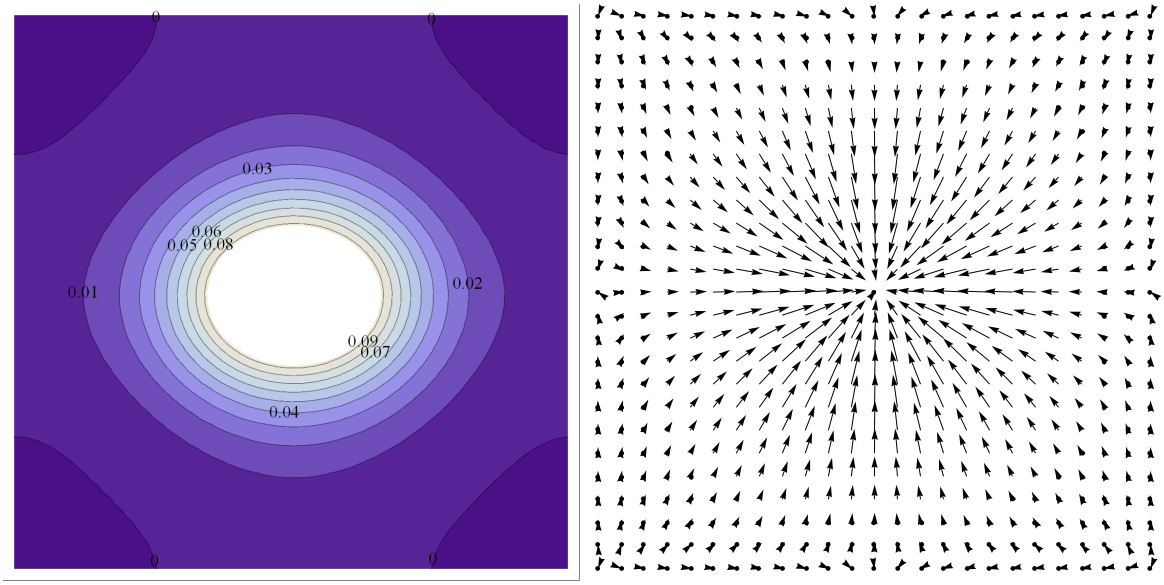

(a) (b)

Figure 3.11: (a) Contour plot of a bimeron charge density at interlayer separation $d/\ell = 0.2$(the SU(2) symmetry of the Coulomb potential is broken) and zero tunneling at $\nu_T = 1.02$. The contour labels are values of density in units of $1/2\pi\ell^2$. (b) In-plane components of the same bimeron. The length of the vectors is proportional to the magnitude of $|\rho_{SA}|$ at each point.

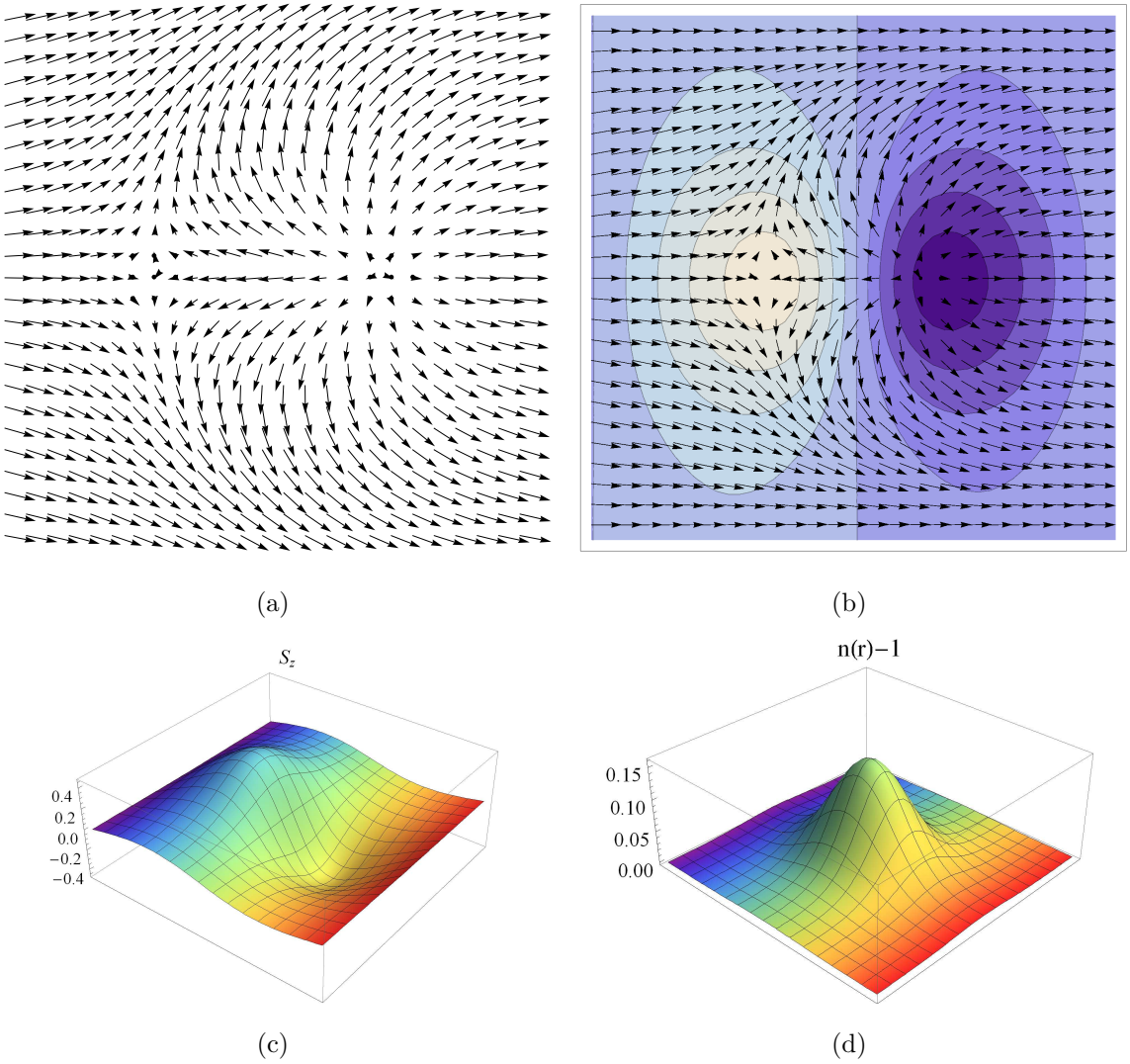

Figure 3.12: (a) In-plane components of the pseudo-spin of a bimeron in the (U,L) basis at $\nu_T = 1.02$, zero tunneling and $d/\ell = 0.2$. The length of the vectors is proportional to the magnitude of $|\rho_{UL}|$ at each point. (b) The In-plane pseudo-spin field (vectors) and Z-component of the same set of vectors(contour). (c) Z-component of the same bimeron in (U,L) basis: $\rho_{UU} - \rho_{LL}$ in units of $1/2\pi\ell^2$. (d) 3D plot of the excess density of the bilayer system due to the same bimeron in units of $1/2\pi\ell^2$. The colors do not have a physical interpretation.

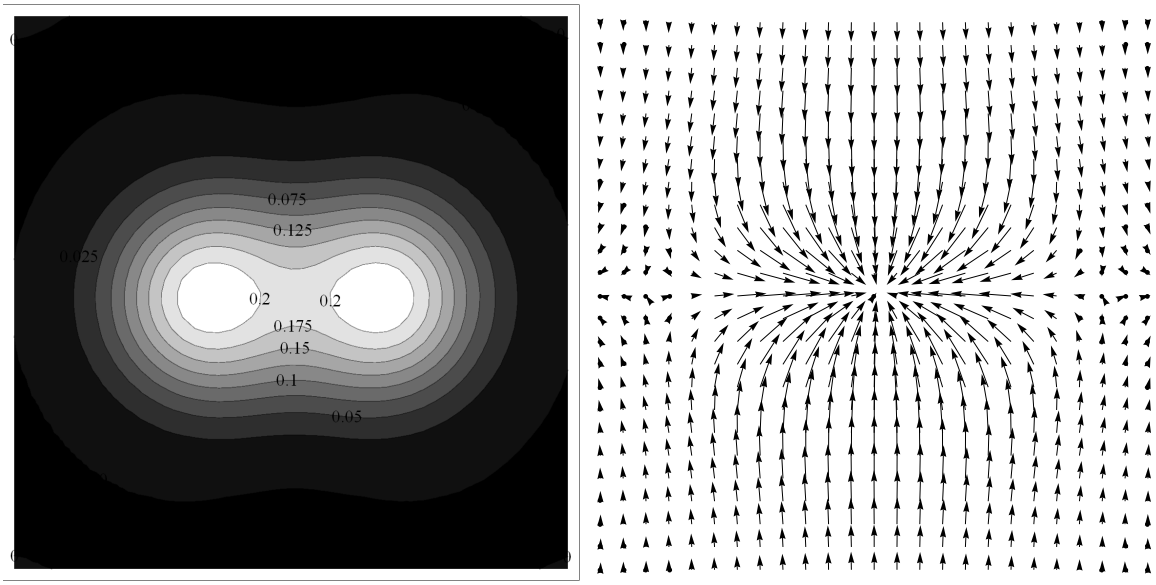

(a) (b)

Figure 3.13: (a) Contour plot of a bimeron at interlayer separation $d/\ell = 0.8$ and zero tunneling at $\nu_T = 1.02$. The contour labels are values of density in units of $1/2\pi\ell^2$. (b) In-plane components of the same bimeron. The length of the vectors is proportional to the magnitude of $|\rho_{SA}|$ at each point.

center are more pronounced. As we mentioned before each of the constituent vortices of a bimeron are called a *meron*. Merons have vorticity and a strong imbalance at their core. In a bimeron, just like a skyrmion, the pseudo-spin gradually rotates by 180 degrees from the center to boundary (as can be seen in S,A basis) while in a meron the pseudo-spin rotates only 90 degrees from the center to boundary. Another possible lattice solution for the Hartree-Fock equations is having two extra electrons per unit cell in a square lattice of merons. In fact it turns out that at zero tunneling and high density of bimerons this lattice is energetically favorable (Figure 3.15). A meron lattice can be obtained by imposing vortex symmetry on ρ_{UL}:

$$\rho_{UL}(\mathcal{R}_{\frac{\pi}{2}}\mathbf{r}) = e^{i\pi/2}\rho_{UL}(\mathbf{r}). \tag{3.66}$$

Figure 3.16 shows a lattice of merons. The arrows are the XY components of the merons in (U,L) basis:

$$\begin{aligned} p_z &= \rho_{UU} - \rho_{LL} \\ p_x + ip_y &= 2\rho_{UL} \end{aligned} \tag{3.67}$$

Each meron has half the total charge of a bimeron so it carries total of $\pm e/2$ charge. Also clearly each meron is carrying a local charge imbalance ($\propto p_z$) at its center which

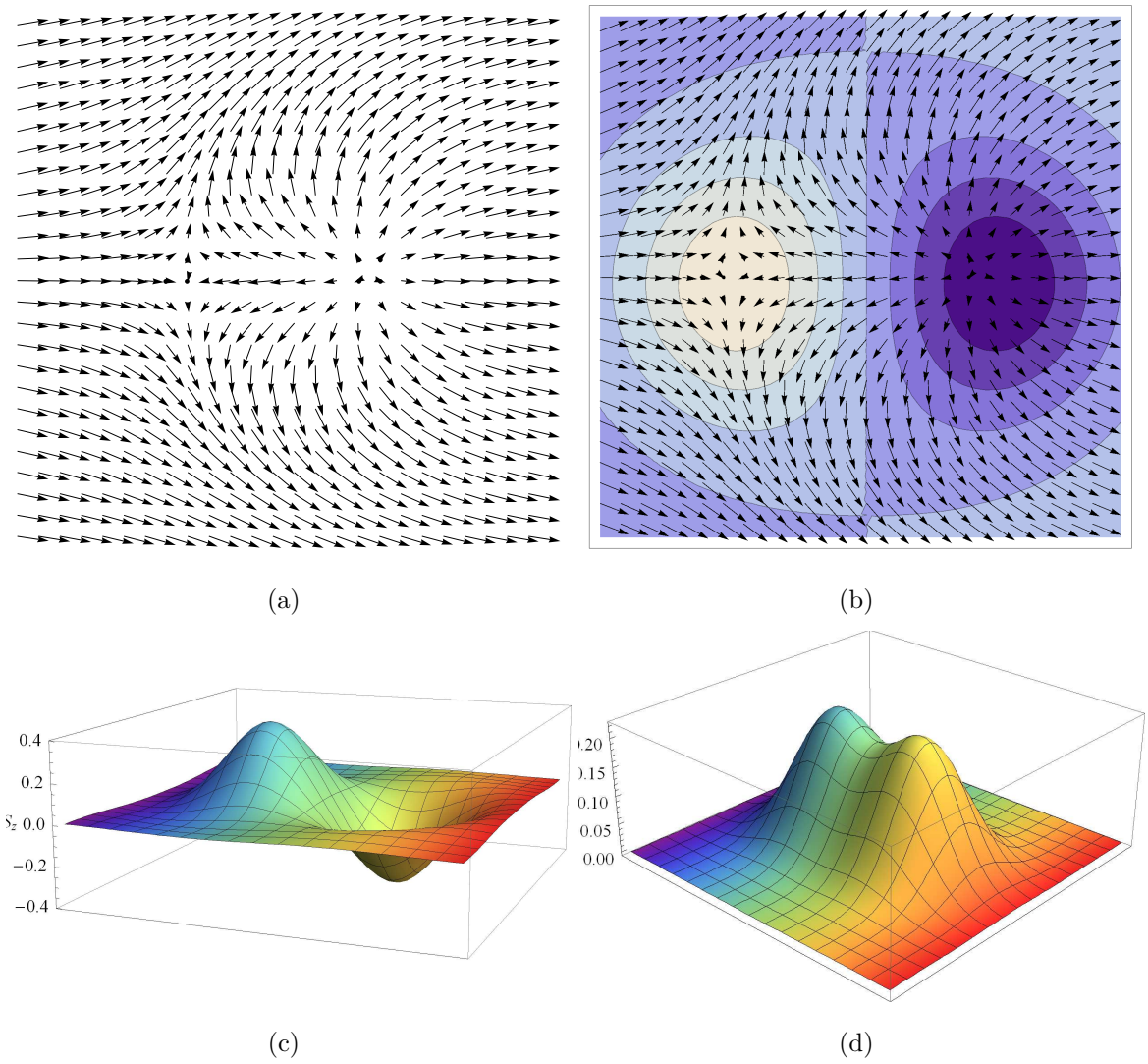

Figure 3.14: (a)In-plane components of the pseudo-spin of a bimeron in (U,L) basis at $\nu_T = 1.02$, zero tunneling and layer separation $d/\ell = 0.8$. The length of the vectors is proportional to the magnitude of $|\rho_{UL}|$ at each point. (b)The In-plane pseudo-spin field (vectors) and Z-component of the same set of vectors(contour). (c) Z-component of the same bimeron in (U,L) basis: $\rho_{UU} - \rho_{LL}$ in units of $1/2\pi\ell^2$. (d) 3D plot of the excess density of the bilayer system due to the same bimeron in units of $1/2\pi\ell^2$.

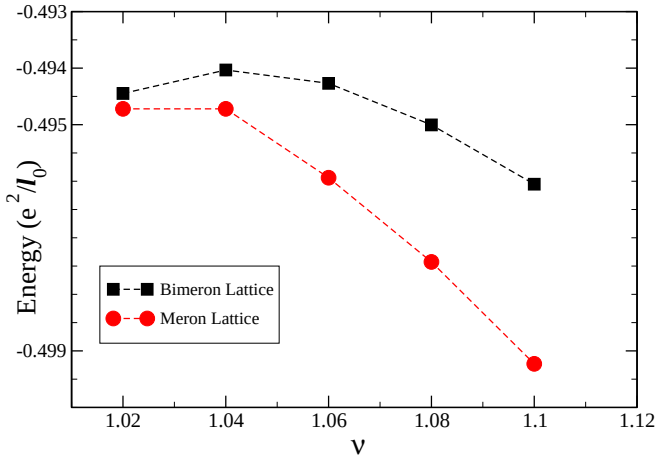

Figure 3.15: Hartree-Fock energy per electron for two different lattice states v.s. total filling factor of the bilayer system at zero tunneling.

is an *electric dipole moment* called the *meron's polarity*. Consequently merons are of four types: V↑,A↑,V↓ and A↓, in which V(A) represents vortex(anti-vortex) and ↑(↓) represents polarity up(down) toward upper(lower) layer. In a balanced bilayer system the charge of a meron is $q = -n\sigma$ in which n is the vorticity and σ is the polarity [27]. It turns out later on that in the imbalanced case the charges are slightly different.

3.6 Spin Investigations in Bilayers

3.6.1 NMR Experiment

As mentioned in the previous section, for very low tunneling $\Delta_{SAS} \ll \Delta_Z$, the lowest energy charged excitations of the bilayer quantum Hall system are bimerons which are of pseudo-spin nature. This result, however, assumes that the spin fluctuations are frozen out and have no contribution to the ground state of the texture lattice, an assumption that is only valid when ignoring many body effects. In an attempt to investigate the spin structure of the electron system in bilayers two different experiments have been performed separately, nuclear magnetic resonance experiments[50] and tilting the sample in magnetic field. We will explain the latter in the next section. Figure(3.17) shows the nuclear magnetic relaxation times of the bilayer system for different filling factors away from $\nu_T = 1$. This result is reminiscent of the data from single layer quantum Hall ferromagnets discussed in section 2.2.6. The rapid reduction of the relaxation time of nuclear spins can be interpreted as coupling to a low

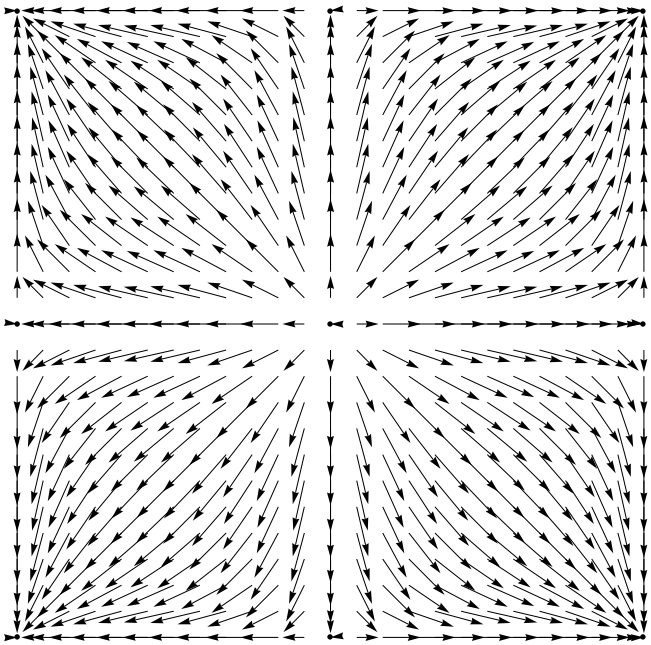

(a)

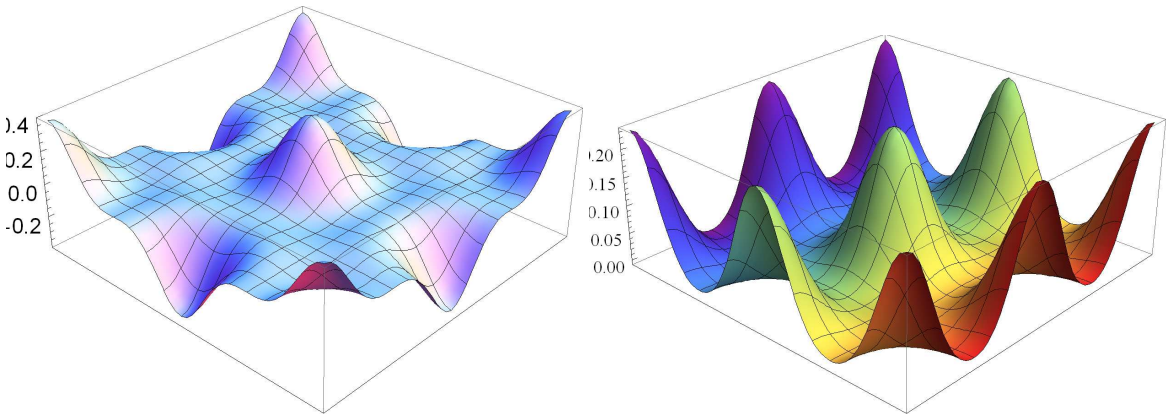

(b) (c)

Figure 3.16: (a)In-plane components of pseudo-spin vectors of a meron lattice in (U,L) basis at $\nu_T = 1.02$, layer separation $d/\ell = 0.8$ and zero tunneling. The length of the vectors is proportional to the magnitude of $|\rho_{UL}|$ at each point. (b) Z-component of the same meron lattice state in (U,L) basis: $\rho_{UU} - \rho_{LL}$ in units of $1/2\pi\ell^2$. (c) 3D plot of the excess density of the bilayer system due to the same meron lattice in units of $1/2\pi\ell^2$.

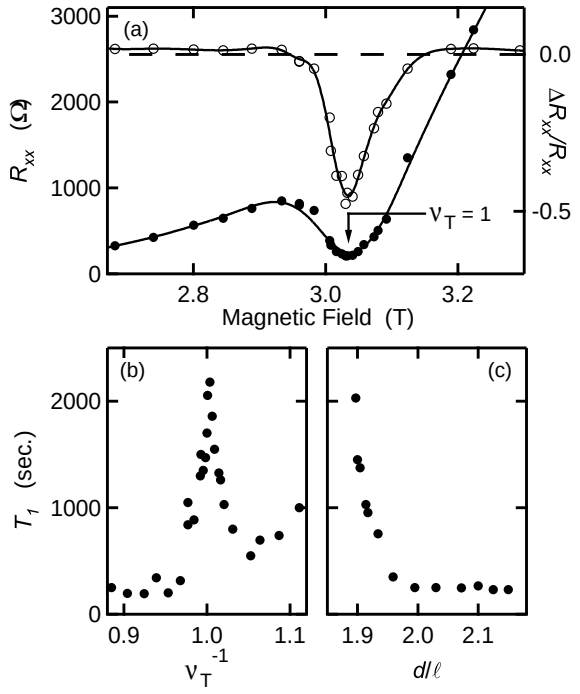

Figure 3.17: (a) Resistively detected NMR. Solid dots: Equilibrium longitudinal resistance Rxx near $\nu_T = 1$. Open dots: Fractional change in R_{xx} in response to ^{71}Ga NMR pulses. Solid lines are guides to the eye. (b) NMR T_1 relaxation time vs inverse filling factor. (c) T_1 v.s. d/ℓ at $\nu_T = 1$. All data at T=35 mK. After [50].

frequency spin wave mode. Because the Coulomb interaction is not spin dependent it is expected that in the coherent regime the spin wave excitations of the bilayer system have the same properties as that of single layers, meaning that they are gapped with a frequency much higher than the nuclear spin frequency, and consequently it is not possible for the nuclear spins to come to equilibrium via this mode. The other possibility would be the presence of a skyrmion lattice similar to single layers. This interpretation of the experimental data suggests that the lowest energy excitations of the bilayer system might have spin textures involved. We should note that the NMR data represented have been taken at relatively large layer separations $d/\ell \gtrsim 1$ where many body effects are the most effective, as one expects for very large separations where pseudo-spin excitations are destroyed by quantum fluctuations.

Based on these ideas it seems necessary to find microscopic solutions of the bilayer texture that involves both spin and pseudo-spin. In fact at large separations, it may be possible that some of the charging energy associated with the imbalance at the center of merons is compensated by the lower energy cost of tilting the spin at those regions. This will give us a motivation to investigate the pseudo-spin with *interwoven spin textures*.

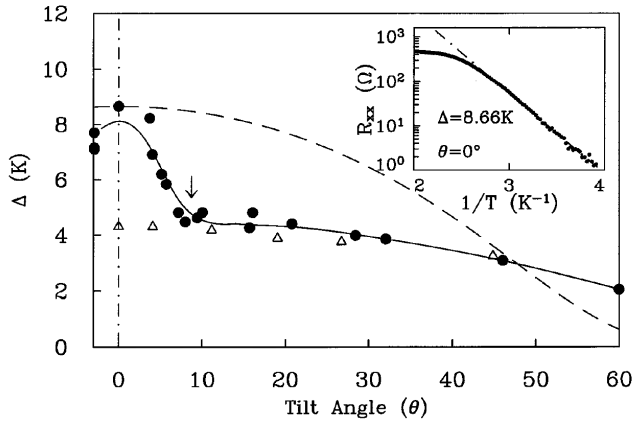

Figure 3.18: The energy gap as a function of tilt angle in a weakly tunneling bilayer sample $\Delta_{SAS} = 0.8K$. The solid circles are for $\nu_T = 1$. The triangles for $\nu_T = 2/3$. The dashed line is the predicted behavior of $\frac{\Delta_{SAS}}{\Delta(\theta=0)}$. After [47].

3.6.2 Parallel Magnetic Field

The longitudinal resistivity in bilayer systems is activated (i.e. has Arrhenius behavior) when the resistance is caused by thermally activated processes. The low temperature activation energy of bilayer system is shown in the inset of the figure 3.18. This activation energy measured here is much larger than Δ_{SAS}. This alone can be a signal of the fact that this gap is not a single particle gap. Also the Arrhenius behavior is valid up to temperatures much lower than Δ ($\sim 0.05\Delta$) which means this gap can not be a single particle gap. This destruction of the activated behavior at low temperatures is because the order that had been produced by the collective gap is destroyed.

One of the early experiments performed in order to investigate the coherence between the quantum wells was the application of a relatively weak magnetic field parallel to the plane of the 2D electron systems[47]. This task can be achieved by tilting the sample in a magnetic field. In this situation the activation energy is measured with respect to the tilt angle. The behavior of the bilayer activation energy with respect to the tilt angle is seen in figure 3.18. This response is definitely not consistent with the assumption that the tilting only changes the Zeeman coupling because the activation energy is not sensitive to Zeeman coupling. In this sample, in which tunneling is non-zero, the tunneling electrons will acquire an Aharanov-Bohm phase as is illustrated in the figure (3.19). Consequently one can replace the

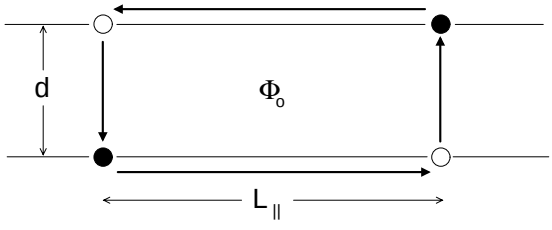

Figure 3.19: Schematic diagram of two parallel 2DEG in presence of a parallel magnetic flux Φ_0. The arrows show the path of a typical tunneling electron.

tunneling amplitude t by te^{iQx} in the Hamiltonian in which $Q = 2\pi/\ell_{\|}$ and so the effective energy becomes

$$E = \int d^2r \Big[\frac{1}{2}\rho_s|\nabla\varphi|^2 - \frac{t}{2\pi\ell^2}\cos(\varphi - Qx)\Big] \tag{3.68}$$

where φ is the phase degree of freedom of the pseudo-spin[29]. At low $B_{\|}$, Q is small and the low energy state has $\varphi \approx Qx$ in other words the local spin orientation tumbles. On the other hand, at large $B_{\|}$ the gradient cost is too large and we have $\varphi \approx$ constant. This is a change in the ground state that can be seen in figure 3.18. In other words, at small tilt angle the pseudo-spin activation rapidly changes but very soon prefers to stay constant and remains so at large angles.

It is anticipated that by a continuous change of the layer charge densities the system can go from a balanced coherent bilayer system to a single layer system where all the charges are gathered in one layer. In this process how do the low energy excitations of the system change? We already know that the excitations of the balanced system have pseudo-spin nature while in the single layer it involves only real spin. Measuring the behavior of the activation energy with respect to tilt angle for different density imbalances can reveal what happens. Figure 3.20 shows the activation energy with respect to tilt angle for imbalances equal to zero to nearly 100%. As we can see the behavior changes continuously from non-monotonic to monotonic signalling a continuous change of the activated state from pseudo-spin to spin. This is telling

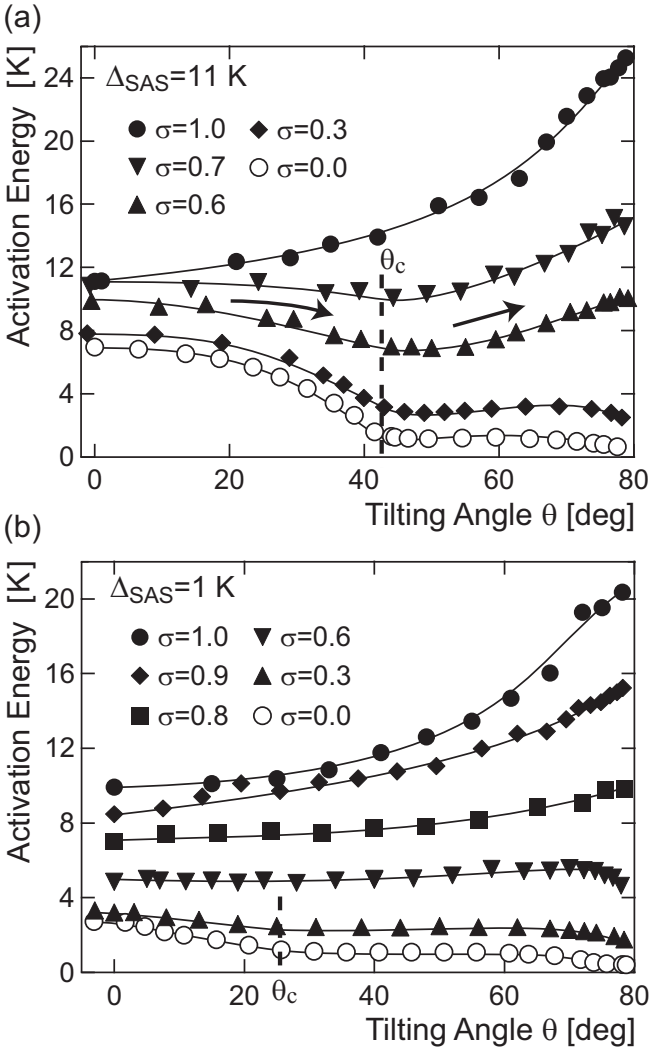

Figure 3.20: (a) The angular dependence of the activation energy of a bilayer sample for $\Delta_{SAS} = 11K$ and different layer imbalances $\sigma = \Delta\nu/\nu_T$. The arrows indicate a combination of both real spin and pseudo-spin behavior at $\sigma = 0.6$. (b)The same for $\Delta_{SAS} = 1K$. The effect of tilt angle is greatly reduced due to reduced tunneling. After [40].

us that a combination of spin and pseudo-spin texture state may be present in the system. In the next section we will explain how we can numerically show that the Hartree-Fock equations support the existence of a spin combined with pseudo-spin texture lattice state.

3.7 CP3 Skyrmions

Including the spin of electrons in a bilayer system, the lowest Landau level subbands would be $\alpha = (S,\uparrow),(A,\uparrow),(S,\downarrow),(A,\downarrow)$. The group of rotations of the wave function of electrons would be isomorphic to the SU(4) group. However the Hamiltonian of the bilayer system has an extra U(1) gauge symmetry that reduces the SU(4) to the CP(3) group [52]. A CP(3) transformation rotates the four-component spinor with a common local phase

$$\psi_\sigma(r) \rightarrow e^{i\varphi(r)}\mathcal{R}_{\sigma\sigma'}\psi_{\sigma'}(r) \tag{3.69}$$

in which $\mathcal{R}$ is an SU(4) rotation matrix. The Hamiltonian for each of the layers separately has a U(1) symmetry due to spin but for a bilayer system the inter-layer exchange interaction requires that the phase of the two layers be the same to keep the Hamiltonian invariant. This is a very important fact about the bilayer system, otherwise one could argue that the spin-pseudo-spin textures are nothing but two separate spin and pseudo-spin textures each with a separate topological winding number. In the bilayer system this is not in fact true and the inter-layer interaction makes it possible to have one spin-pseudo-spin texture with one topology, in other words this texture has a single topological winding number. This CP(3) object is often called a *CP(3) Skyrmion* or an *interwined texture*.

To find the equation of motion for the Green's function of the bilayer system that involves both spin of electrons and pseudo-spin we proceed exactly as in section 3.4. The Hamiltonian now involves both the Zeeman term and tunneling term

$$\begin{aligned}\mathcal{H} &= \frac{1}{2S}\sum_{\mathbf{q}}\sum_{\{X\}}\sum_{\alpha\beta} V_{\alpha\beta}(\mathbf{q})M^{\alpha}_{\mathbf{q}}(X_1|X_4)M^{\beta}_{-\mathbf{q}}(X_2|X_3)c^{\dagger}_{\alpha X_1}c^{\dagger}_{\beta X_2}c_{\beta X_3}c_{\alpha X_4} \\ &+ \frac{\Delta_Z}{2}\sum_{X,j=U,L}(c^{\dagger}_{j\uparrow,X}c_{j\uparrow,X} - c^{\dagger}_{j\downarrow,X}c_{j\downarrow,X}) - \frac{\Delta_{SAS}}{2}\sum_{X,\sigma}(c^{\dagger}_{U\sigma,X}c_{L\sigma,X} + c^{\dagger}_{L\sigma,X}c_{U\sigma,X})\end{aligned} \tag{3.70}$$

in which M's are defined in equation (3.30) and $\alpha,\beta = U\uparrow, L\uparrow, U\downarrow, L\downarrow$ (Note that we are using the (U,L) basis). Because the Coulomb potential is spin independent

the matrix elements of the V are exactly the same as ones in eq.(3.31). Following the same line of derivation as in equations (3.33-3.38) we find

$$\frac{\partial G_{\alpha\beta}(XX')}{\partial\tau} = -\delta_{\alpha\beta}\delta_{XX'}\delta(\tau) - \frac{1}{S}\sum_{q,X,\alpha'\beta'} V_{\alpha'\beta'}(q) M_q^{\alpha'}(X_1|X_4) M_{-q}^{\beta'}(X_2|X_3) \times$$
$$\times\Big\{\rho_{\beta'\beta'}(X_2X_3)G_{\alpha'\beta}(X_4X') - \rho_{\beta'\alpha'}(X_2X_4)G_{\beta'\beta}(X_3X')\Big\}\delta_{\alpha\alpha'}\delta_{XX_1} +$$
$$-\frac{\Delta_Z}{2}\Big[(\sigma_z)^{4\times4}G(XX')\Big]_{\alpha\beta} + \frac{\Delta_{SAS}}{2}\Big[(\sigma_x\otimes\mathbf{1})^{4\times4}G(XX')\Big]_{\alpha\beta} + \mu G_{\alpha\beta}(XX'). \tag{3.71}$$

In which :

$$\sigma_z^{4\times4} \equiv \begin{pmatrix} \mathbf{1} & \mathbf{0} \\ \mathbf{0} & -\mathbf{1} \end{pmatrix},\ \sigma_x\otimes\mathbf{1} = \begin{pmatrix} 0 & 1 & 0 & 0 \\ 1 & 0 & 0 & 0 \\ 0 & 0 & 0 & 1 \\ 0 & 0 & 1 & 0 \end{pmatrix}$$
$$G = \begin{pmatrix} G_{U\uparrow,U\uparrow} & G_{U\uparrow,L\uparrow} & G_{U\uparrow,U\downarrow} & G_{U\uparrow,L\downarrow} \\ G_{L\uparrow,U\uparrow} & G_{L\uparrow,L\uparrow} & G_{L\uparrow,U\downarrow} & G_{L\uparrow,L\downarrow} \\ G_{U\downarrow,U\uparrow} & G_{U\downarrow,L\uparrow} & G_{U\downarrow,U\downarrow} & G_{U\downarrow,L\downarrow} \\ G_{L\downarrow,U\uparrow} & G_{L\downarrow,L\uparrow} & G_{L\downarrow,U\downarrow} & G_{L\downarrow,L\downarrow} \end{pmatrix} \tag{3.72}$$

The projection of the Coulomb potential in the lowest Landau level will give the same functions as before because the Coulomb term is spin independent. So finally after Fourier transforming we will have

$$\begin{aligned}(-i\omega-\mu)G_{\alpha\beta}(\mathbf{k}) &= -\delta_{\mathbf{k},\mathbf{0}}\delta_{\alpha\beta} - U_{\alpha\alpha'}(\mathbf{k},\mathbf{k}')G_{\alpha'\beta}(\mathbf{k}') = \\ &= -\delta_{\mathbf{k},\mathbf{0}}\delta_{\alpha\beta} - e^{i\frac{\ell^2}{2}\mathbf{k}\times\mathbf{k}'}W_{\alpha\alpha'}(\mathbf{k}-\mathbf{k}')G_{\alpha'\beta}(\mathbf{k}'). \end{aligned}\tag{3.73}$$

in which

$$\begin{aligned}W_{\alpha\alpha'}(\mathbf{G}) &= \frac{\delta_{\alpha\alpha'}}{2\pi\ell^2}\sum_{\beta'} V_{\alpha\beta'}(\mathbf{G})\rho_{\beta'\beta'}(\mathbf{G}) - I_{\alpha\alpha'}(\mathbf{G})\rho_{\alpha'\alpha}(\mathbf{G}) + \\ &+ \frac{\Delta_Z}{2}(\sigma_z^{4\times4})_{\alpha\alpha'}\delta_{\mathbf{G},0} - \frac{\Delta_{SAS}}{2}(\sigma_x\otimes\mathbf{1})_{\alpha\alpha'}\delta_{\mathbf{G},0}. \end{aligned}\tag{3.74}$$

In all the above there is a summation over repeated indices. The potentials I are defined in equations (3.43,3.44). To understand the interplay between spin and pseudospin we can calculate the energy of the system in the Hartree-Fock approximation following the equations (3.57-3.59)

$$\langle\mathcal{H}\rangle = \frac{1}{2}\sum_{\mathbf{k},\alpha\beta} I_{\alpha\beta}(\mathbf{k})\rho_{\alpha\beta}(\mathbf{k})\rho_{\beta\alpha}(-\mathbf{k}) - \frac{1}{2}\sum_{\alpha\beta} V_{\alpha\beta}(\mathbf{q})\rho_{\alpha\alpha}(-\mathbf{q})\rho_{\beta\beta}(\mathbf{q}) +$$

$$+ \quad \frac{\Delta_Z}{2}\sum_{j=U,L}\Big[\rho_{j\uparrow,j\uparrow}(0)-\rho_{j\downarrow,j\downarrow}(0)\Big]-\frac{\Delta_{SAS}}{2}\sum_{\sigma=\uparrow,\downarrow}\Big[\rho_{U\sigma,L\sigma}(0)+\rho_{L\sigma,U\sigma}(0)\Big] \tag{3.75}$$

The first term in the above equation involves the inter-layer and intra-layer exchanges including terms like $I_{UL}\rho_{U\uparrow}\rho_{L\downarrow}$ which are spin-pseudo-spin exchange terms. The second term involves inter-layer and intra-layer direct Coulomb interactions.

Before starting the calculation we should note that the CP(3) skyrmion may not exist in all parts of the phase diagram. The phase diagram of the spin-pseudo-spin system includes interlayer bias, interlayer tunneling, Zeeman coupling and of course layer separation and filling factor. In this five dimensional parameter space we have been able to find only a few solutions of equation (3.73). As was mentioned before it is expected that high Zeeman couplings ($\Delta_Z \gg \Delta_{SAS}$) destroy the spin textures. We also argued that at the center of a CP(3) skyrmion texture a tilt of spin may compensate for the charging energy associated with the local imbalance of the pseudo-spin texture, in other words a spin flip at the center may be able to relax some of the charging energy cost. This argument however would be true if we are at large inter-layer separations ($d/\ell > 1$) where the pseudo-spin exchange energy is small enough for spin to be able to compensate. Consequently the CP(3) skyrmion may not exist at small layer separations ($d/\ell \ll 1$). In fact the spin transition in NMR experiments have been observed close to the phase boundary. These experiments have been also performed at vanishing tunneling samples. These analysis suggest we should start to look for CP(3) solution in zero tunneling, low Zeeman gap and large separations. On the other hand as was discussed in the previous section at low tunneling the bimeron lattice prefers to transform to a meron lattice which is a vortex-antivortex lattice. Consequently we start the iterative process with the spin and pseudo-spin distribution following the idea of reference [52] in which we impose vortex symmetry in spin of each layer and at the same time impose vortex symmetry in the pseudo-spin in each spin band:

$$\begin{aligned}
\rho_{U\uparrow L\uparrow}(\mathcal{R}_{\pi/2}\mathbf{G}) &= e^{i\pi/2}\rho_{U\uparrow L\uparrow}(\mathbf{G}) \\
\rho_{U\downarrow L\downarrow}(\mathcal{R}_{\pi/2}\mathbf{G}) &= e^{-i\pi/2}\rho_{U\downarrow L\downarrow}(\mathbf{G}) \\
\rho_{U\uparrow U\downarrow}(\mathcal{R}_{\pi/2}\mathbf{G}) &= e^{i\pi/2}\rho_{U\uparrow U\downarrow}(\mathbf{G}) \\
\rho_{L\uparrow L\downarrow}(\mathcal{R}_{\pi/2}\mathbf{G}) &= e^{-i\pi/2}\rho_{L\uparrow L\downarrow}(\mathbf{G})
\end{aligned} \tag{3.76}$$

Usually the iterative procedure itself finds the solution imposing only three of the above.

3.7.1 Numerical Results

The Hartree-Fock approximation does not converge at separations larger than $d/\ell \sim 1.2$ (due to lack of sufficient accuracy for correlations) so we limit our calculations for separations $0 \leq d/\ell \leq 1.2$. Experiments have been performed[50] at larger separations ($d/\ell \sim 1.92$) but we should note that our calculations neglect layer thickness and disorder. Figure (3.23) represents the core of our numerical results. This figure shows the reduction of the charge density due to the presence of a vortex-antivortex lattice of spin and pseudo-spin at total filling factor $\nu = 0.97$ at $d/\ell = 1.$, zero tunneling and $\Delta_Z = 0.002(e^2/\ell)$. Because the total filling factor here is smaller than $\nu_T = 1$ the textures are equivalent to quasi-holes of an electron gas hence the density difference plotted is negative. The lower plots are spin and pseudo-spin out of plane distributions which show that neither spin nor pseudo-spin have complete polarization. The vorticity of spin and pseudo-spin is shown in figure (3.22) as well. The size of the vectors are relative to the projection of the pseudo-spin or spin into the XY plane. As we can see each pseudo-spin vector is rotated by $\pi/2$ locally with respect to the spin vector at the same position, in other words

$$\begin{aligned} \rho_{U\uparrow,L\uparrow}(\mathbf{G}) &= e^{i\pi/2}\rho_{U\uparrow,U\downarrow}(\mathbf{G}) \\ \rho_{U\downarrow,L\downarrow}(\mathbf{G}) &= e^{i\pi/2}\rho_{L\uparrow,L\downarrow}(\mathbf{G}). \end{aligned} \tag{3.77}$$

Figure (3.23) shows the energy difference of CP(3) skyrmion lattice and meron lattice ($E_{CP3} - E_{Meron}$) per electron in terms of mK. The energies are with respect to layer separation for three different Zeeman gaps. The experimentally relevant Zeeman gaps are about $\Delta_Z = 0.006(e^2/\ell)$[50]. As we can see in this picture the CP(3) skyrmion lattice has lower energy at high layer separations. This figure also clearly shows the spin polarization per electron for the CP(3) skyrmion lattice with respect to layer separation is incomplete for three different Zeeman couplings. In figure (3.21) although the density of excitations is low ($\nu_T = 0.97$) the CP(3) skyrmions have distributed their density much more uniformly than a bimeron lattice. In fact no bimeron-skyrmion combination has been observed as solution. The CP(3) skyrmion lattice stays the lowest energy state for the whole density interval of $0.8 \leq \nu_T \leq 0.97$.

The CP(3) skyrmion lattice is not the only result of the numerical investigation of bilayer excited states. At different parts of the phase diagram of the spin-pseudo-spin system we have found other states. A list of all these states plus the pure pseudo-spin states follows:

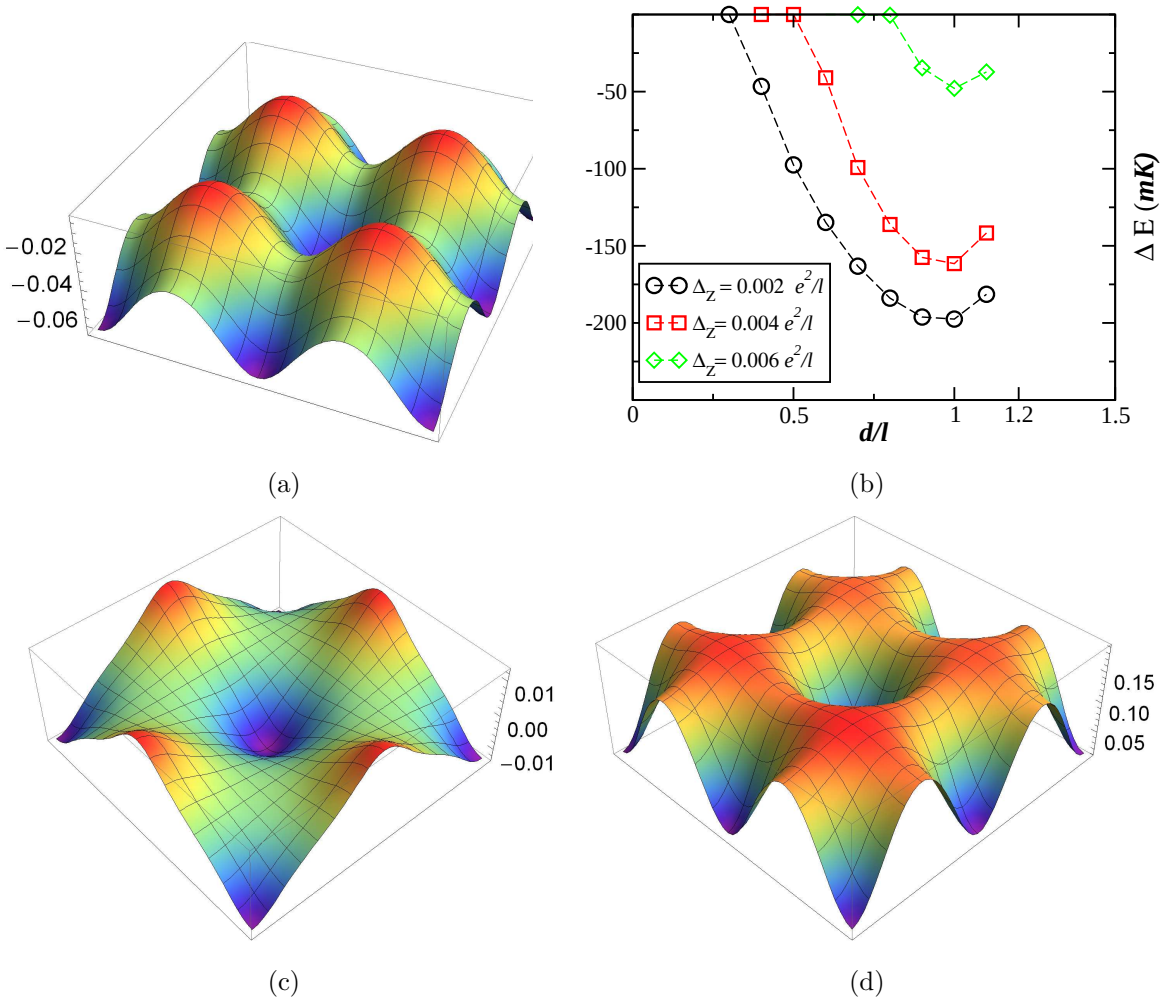

Figure 3.21: (a) Charge density $\rho(\mathbf{r}) - \frac{\mathbf{1}}{\pi\ell^{\mathbf{2}}}$ of a CP3 skyrmion lattice at $\nu_T = 0.97$, $d/\ell = 1.0$, zero tunneling and $\Delta_Z = 0.002(e^2/\ell)$ in unit cell. (b) Energy per electron of the same kind of lattice relative to that of a meron lattice at $\nu_T = 0.8$ at zero tunneling v.s. layer separation. (c) Z-component of psudo-spin in units of $1/2\pi\ell^2$ of the same lattice in (a). (d) Z-component of the real spin in the same state. Colors do not have a physical interpretation.

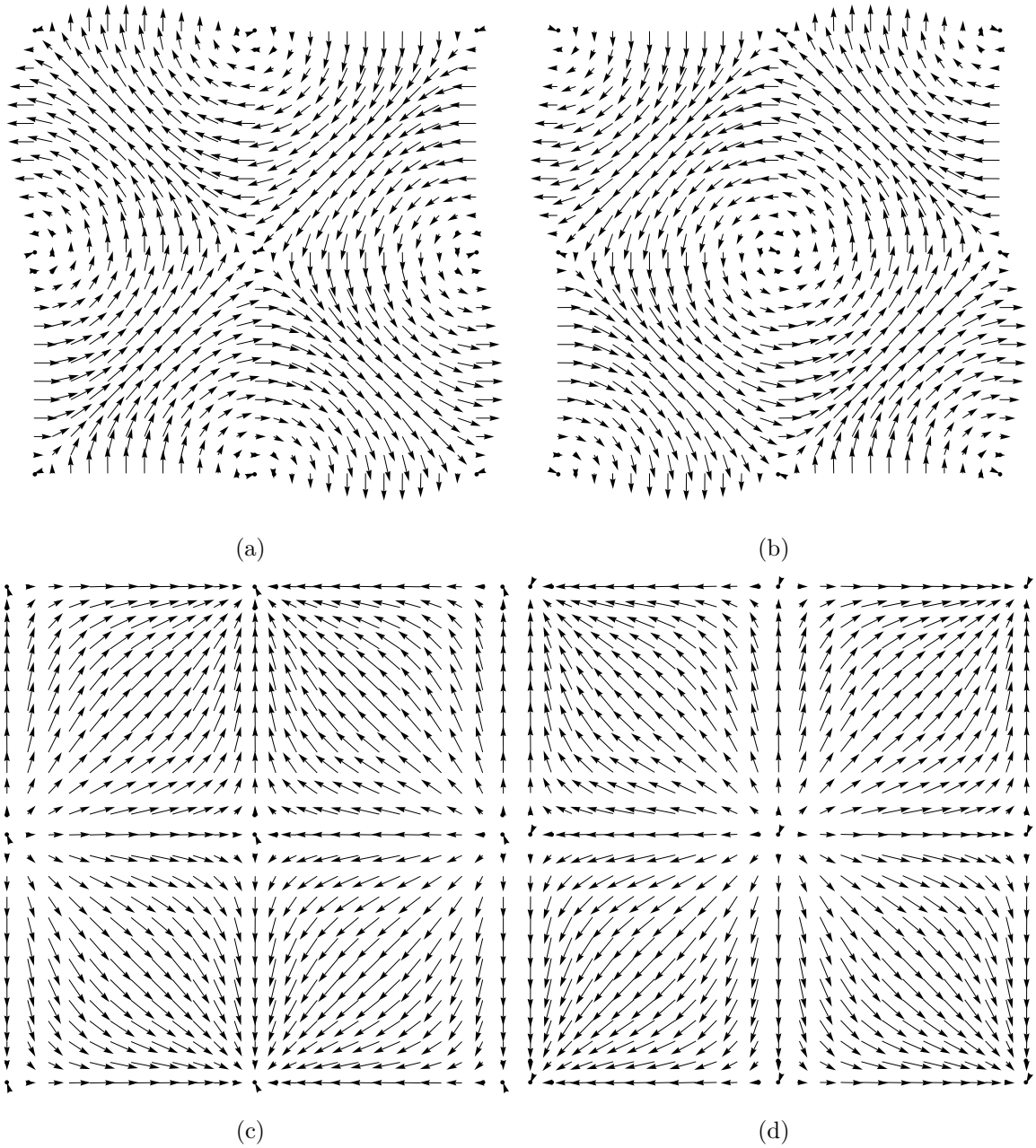

Figure 3.22: In plane component of the (a) spin in upper layer (b) spin in lower layer (c) pseudo-spin in up spin band (d) pseudo-spin in lower spin band of CP3 skyrmion lattice at $d/\ell = 1.0$, zero tunneling, $\Delta_Z = 0.002(e^2/\ell)$ and $\nu_T = 0.97$. All four distributions are associated with one single quantum state of the bilayer system.

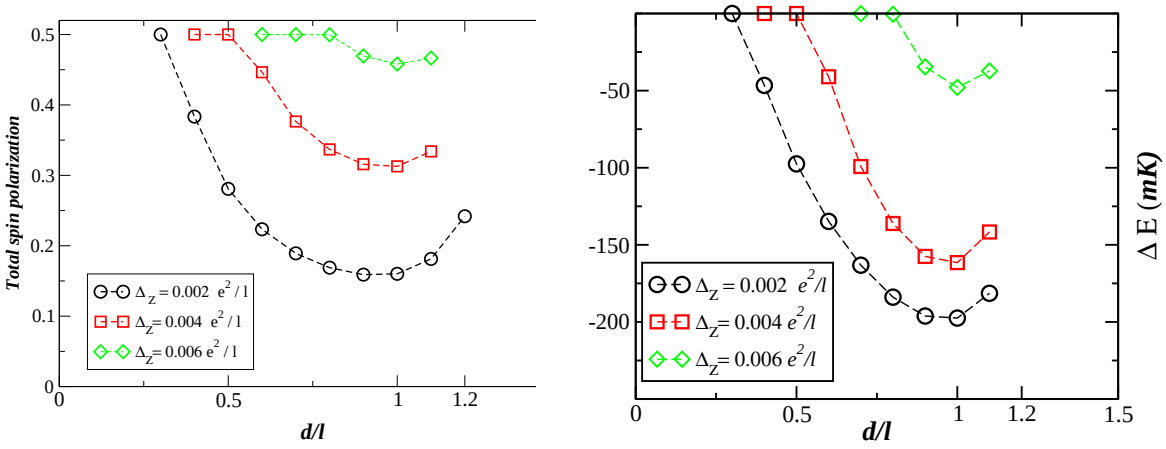

(a) (b)

Figure 3.23: (a) Total spin polarization of a CP3 skyrmion lattice state of bilayer system at $\nu_T = 0.8$ and zero tunneling v.s. layer separation for different Zeeman couplings. (b) Energy per electron of the same state relative to the meron state.

- CP3 Skyrmion: a square lattice with four spin-pseudospin textures(each being half a bimeron) of opposite phases per unit cell as was discussed earlier. This state is represented in Figures 3.21 and 3.22 in the case of zero tunneling.

- Symmetric Skyrmion Lattice (SS): this is a pseudospin- polarized square-lattice state with two symmetric-band spin Skyrmions of opposite phases per unit cell. In other words the skyrmions are formed in a superposition of the upper and lower layer

$$\rho_{S\uparrow,S\downarrow}(\mathcal{R}_{\pi/2}\mathbf{G}) = e^{i\pi/2}\rho_{S\uparrow,S\downarrow}(\mathbf{G}) \tag{3.78}$$

  At the same time however in this state there is spin vortex and antivortex state present in each layer separately. This state exists also at finite tunneling strengths and low Zeeman couplings. Figure 3.24 shows the total excess density of a SS lattice at $\Delta_{SAS} = 0.04(e^2/\ell)$, $\Delta_Z = 0.003(e^2/\ell)$ and $d/\ell = 0.8$. The vector field in this picture is the XY component of the real spin in symmetric band. The same texture lattice is seen in each layer separately but no texture is seen in spin band.

- High tunneling CP3 (HCP3): a square lattice with two spin-pseudo-spin Skyrmions of opposite phase per unit cell. The difference between this state and the CP3 state above is that here the spin texture exists in the symmetric and antisymmetric bands while in the latter it exists separately in each quantum well. This

state is the ground state only when the tunneling gap is higher than the Zeeman gap. We note that the HCP3 state is an intermediate state between SS and bimeron lattice states. The textures in the HCP3 state splits into two vortices with charge $e/2$ by reducing the Zeeman gap. Figure 3.25 shows the total excess density of HCP3 lattice state at $d/\ell = 0.1$, $\Delta_{SAS} = 0.04(e^2/\ell)$ and $\Delta_Z = 0.002(e^2/\ell)$ at filling factor $\nu_T = 1.2$ which is a high density of textures. In this density as we can see the textures have spread their charge density much more uniformly than a usual bimeron lattice. Figure 3.26 shows the XY component of real spin of this state in symmetric, antisymmetric band and the pseudo-spin in up and down spin band. In all these cases we can see the vorticity while separately in each layer no spin or pseudo-spin vorticity can be seen:

$$\rho^{HCP3}_{L\uparrow,L\downarrow}(\mathcal{R}_{\pi/2}\mathbf{G}) \neq e^{i\pi/2}\rho^{HCP3}_{L\uparrow,L\downarrow}(\mathbf{G}) \tag{3.79}$$

- Bimeron Lattice: Discussed in previous section.
- Meron Lattice: Discussed in previous section.

One expects that the SS state will not exist at high Zeeman couplings which is true for all spin textures. One also expects that since the pseudo-spin is polarized, this state should be stable only at high tunneling. However there is an asymmetry between states with filling factor $\nu_T < 1$ and $\nu_T > 1$ as the SS state is stable for low and even zero tunneling at $\nu_T < 1$ while unstable for low tunneling at $\nu_T > 1$. This issue of asymmetry between filling factor above and below $\nu_T = 1$ continues to exist for other spin-pseudo-spin states like the CP(3) skyrmion state in which our numerical routines do not converge for filling factors above $\nu_T = 1$. This may seem to be in contrast with the symmetry observed in the NMR experiments however there are several possibilities that must be addressed:

First this is not surprising because in this four subband level there is no particle-hole symmetry unlike the case of a pure skyrmion or bimeron. Also the stability of these states greatly depends on the lattice structure. In all our numerical work we did not try any other lattice basis such as the triangular basis. One explanation for the existence of high tunneling states like HCP3 at low tunneling samples can be disorder which can pin the lattices and locally stabilize them.

Figure 3.27 shows the difference in the energy of the HCP3 or SS and the bimeron lattice. As we can see, by increasing Δ_{SAS} the ground state changes from bimeron lattice to HCP3 and then to SS. Also in Fig.3.27 we can see the spin depolarization

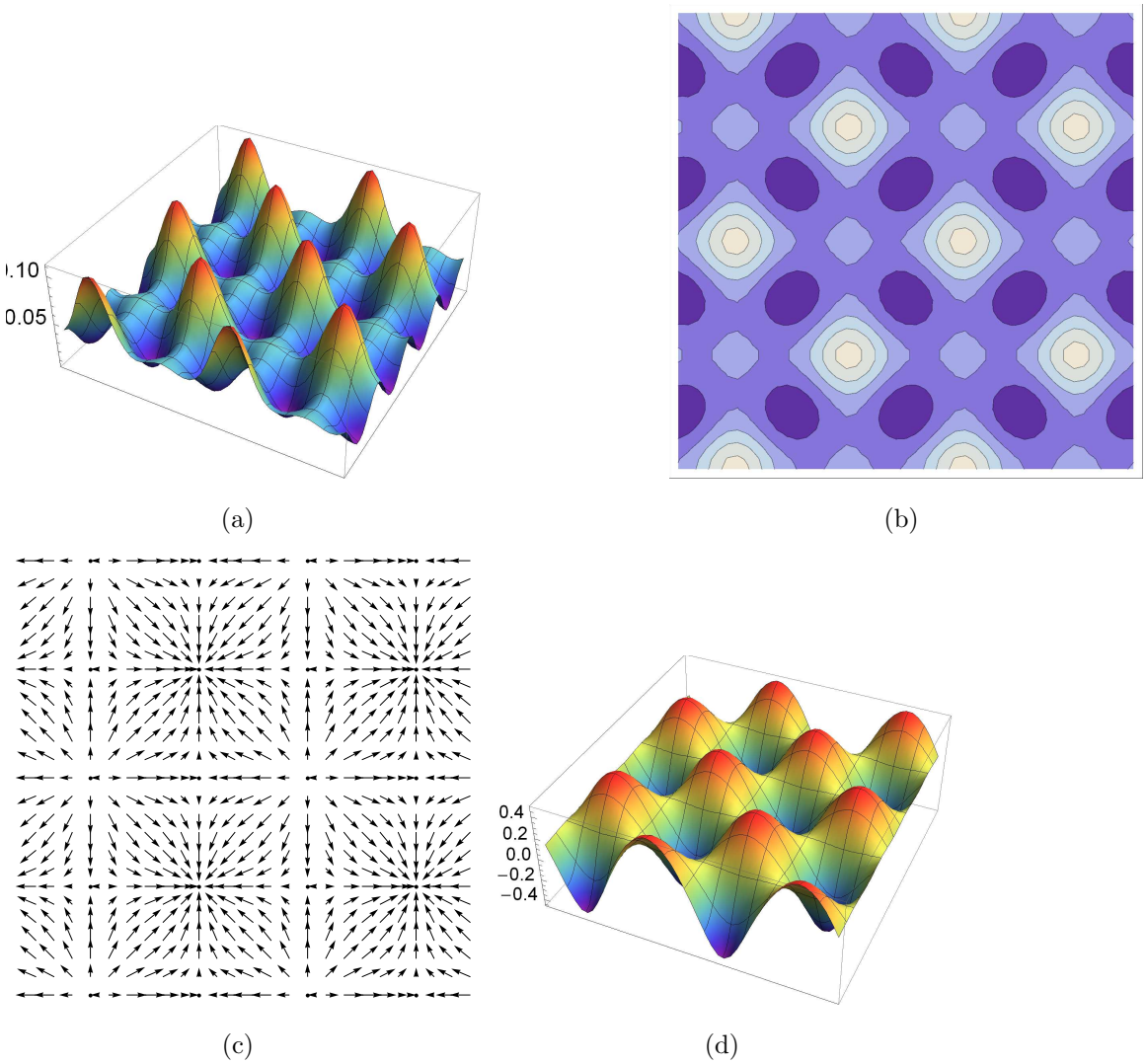

(a) (b)

(c) (d)

Figure 3.24: (a) Excess of total charge density of the symmetric skyrmion lattice state at $d/\ell = 0.8$, $\Delta_{SAS} = 0.04(e^2/\ell)$ and $\Delta_Z = 0.003(e^2/\ell)$ at filling factor $\nu_T = 1.04$.(b) The contour plot of the same state. (c) In-plane component of the spin distribution of the same state. The size of vectors are proportional to $|\rho_{S\uparrow S\uparrow}|$ at each point. (d) Z-component of the spin $\rho_{S\uparrow S\uparrow} - \rho_{S\downarrow S\downarrow}$.

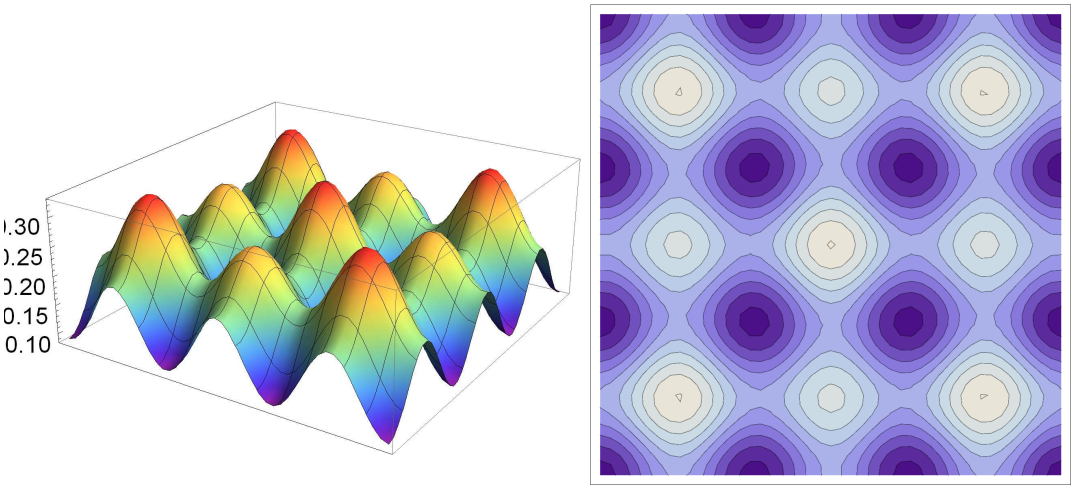

(a) (b)

Figure 3.25: (a) 3D plot (b) contour plot of the excess of the total charge density of a bilayer system in an HCP3 lattice state at $\nu_T = 1.2$, $d/\ell = 0.1$, $\Delta_{SAS} = 0.04(e^2/\ell)$ and $\Delta_Z = 0.002(e^2/\ell)$.

in HCP3 state as a function of Δ_{SAS}. The spin polarization of the HCP3 state is more sensitive to Δ_{SAS} than the SS state. For $\nu_T > 1$ the SS state also can be the ground state. At $\nu_T = 1.04$, we find that the SS state is the ground state for $d/\ell \lesssim 0.8$, $\Delta_{SAS} > 0.03$ and $0 < \Delta_Z \lesssim 0.002(e^2/\ell)$. The spin polarization with interlayer separation in the SS state is shown in Fig.3.27. The linear behavior is also seen at $\nu_T < 1$. This smooth response to layer separation is very different from the response of CP(3) skyrmion state (Fig. 3.23).

3.7.2 Effect of interlayer bias

To conclude this section, we look at the effect of a potential bias on the spin polarization. Intuitively we understand that a CP3 skyrmion involves a twist in some high dimensional space that is difficult to plot in two-dimensions. That twist will occur through degrees of freedom where it costs the least energy, and the texture will vary less in sectors where the system is stiff. If we can change the stiffness of textures along some direction of phase space, we can drive the texture into or out of that degree of freedom. A simple analogy would be to drive an O(3) model into an XY model by making excursions into the z direction too costly. The behavior of this system with respect to bias illustrates this physics. We choose the parameters $d/\ell = 1$, $\nu_T = 0.8$, $\Delta_{SAS} = 0.0002(e^2/\ell) \sim 0.03$K and $\Delta_Z = 0.01(e^2/\ell)$ so that, at the balanced point,

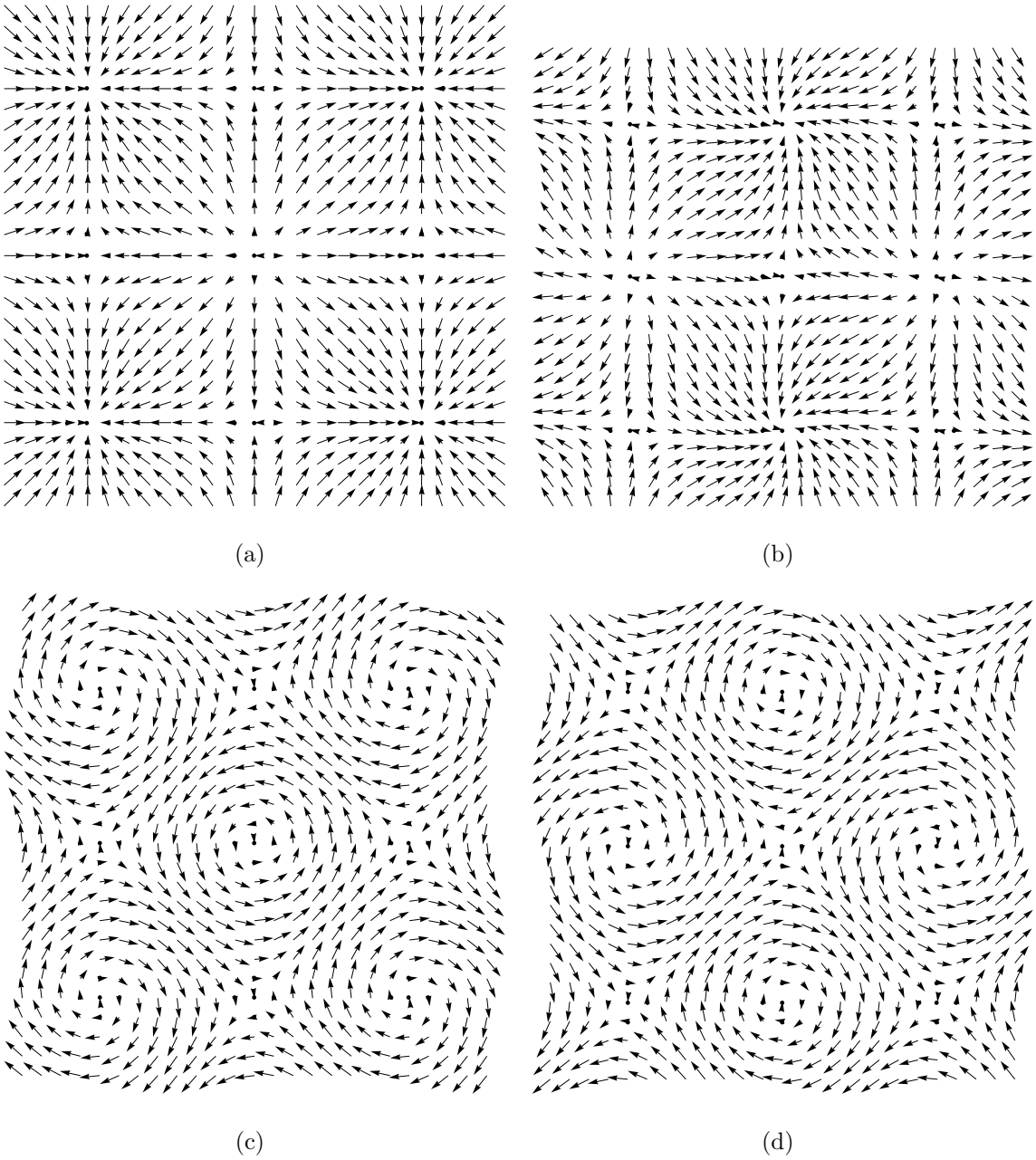

Figure 3.26: In-plane component of the (a) spin in the symmetric band $|\rho_{S\uparrow S\downarrow}|$ and (b) in the antisymmetric band $|\rho_{A\uparrow A\downarrow}|$. (c) pseudo-spin in the up spin band $|\rho_{S\uparrow A\uparrow}|$ and (d) pseudo-spin in down spin band $|\rho_{S\downarrow A\downarrow}|$. All these distributions are associated with a single HCP3 state at $\nu_T = 1.2$, $d/\ell = 0.1$, $\Delta_{SAS} = 0.04(e^2/\ell)$ and $\Delta_Z = 0.002(e^2/\ell)$.

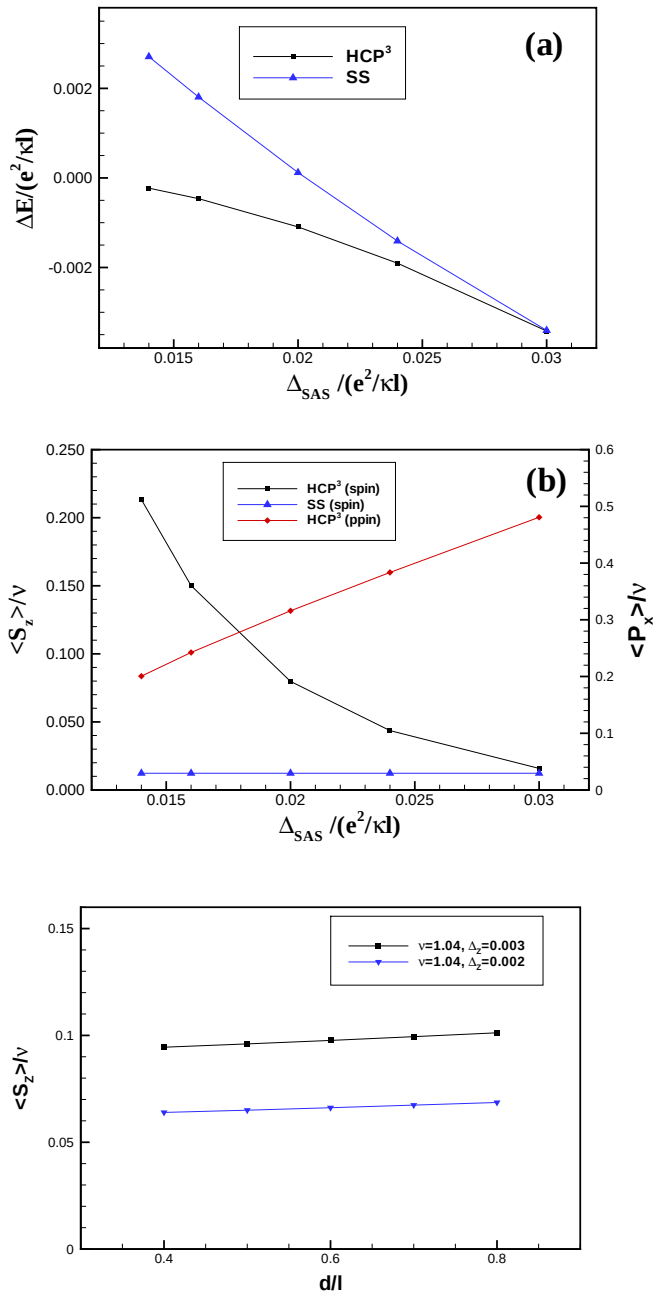

Figure 3.27: (a) Energy difference between the HCP3 crystal or SS crystals and the meron state as a function of tunneling for $\nu_T = 1.2$,$\Delta_Z = 0.0015(e^2/\ell)$ and $d/\ell = 0.1$. (b) Spin and pseudo-spin polarization as a function of tunneling for the HCP3 and SS states. (c) Spin polarization as a function of interlayer separation in the SS state for different values of the Zeeman coupling and filling factors. Here $\Delta_{SAS} = 0.04(e^2/\ell)$ and $\nu_T = 1.04$.

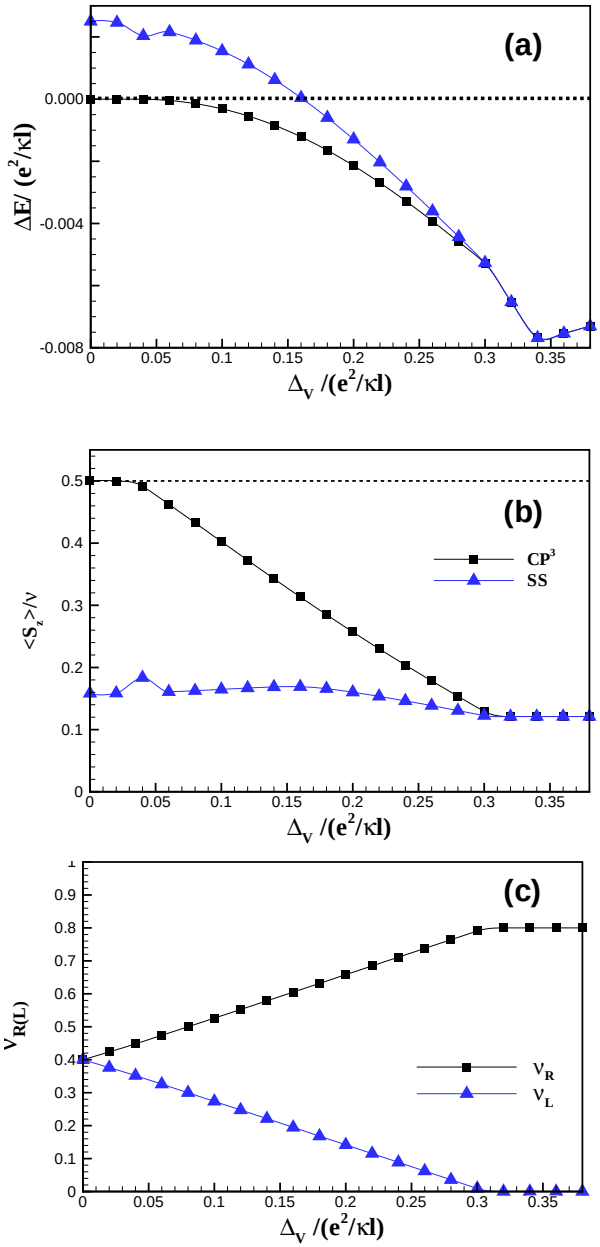

Figure 3.28: (a) Energy difference between the CP3 or SS states and the SPB state. (b) Spin polarization per electron as a function of bias for $\nu_T = 0.8$,$\Delta_{SAS} = 0.0002(e^2/\ell)$ and $\Delta_Z = 0.01(e^2/\ell)$. (c) Filling factor in the right and left wells in the CP3 state.

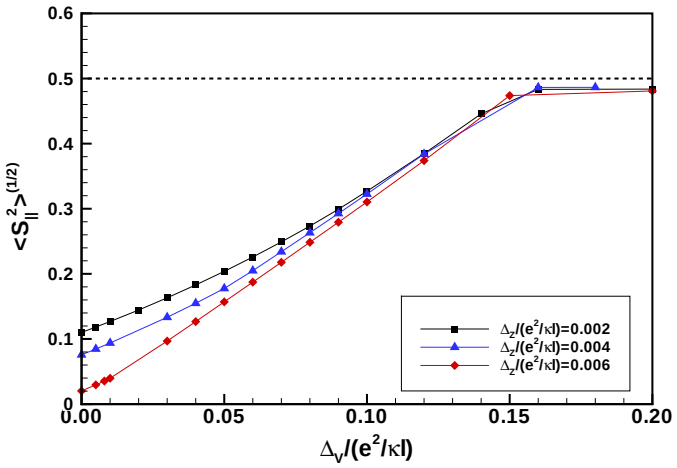

Figure 3.29: Average in-plane spin polarization in the CP3 crystal state as a function of applied bias for $\nu_T = 0.8$,$\Delta_{SAS} = 0.0002(e^2/\ell)$ and $d/\ell = 1.0$.

the ground state is a spin-polarized bimeron crystal. Our numerical results, plotted in Fig.3.28, show that there is a transition first into a CP3 crystal and then into the SS state as the applied bias increases. The energy of the CP(3) skyrmion crystal interpolates nicely between the bimeron and SS phases as can be seen in the figure. The corresponding spin polarizations are shown in Fig.3.28(a,b). The bias induces a linear spin depolarization of the 2DEG in the CP(3) skyrmion state. In effect, the texture inducing the deviation of charge density from $\nu_T = 1$ is being shifted from the pseudo-spin degree of freedom to the spin degree of freedom in a continuous way. Note that the spin polarization varies only slightly with d/ℓ in the SS state. Figure 3.28(c) shows the filling factors ν_L and ν_U in the CP(3) state (the exact same curves are obtained in the SS state). Above $\Delta_b \sim 0.30(e^2/\ell)$, all the charge is transferred into the upper layer and the spin polarization is that appropriate for a monolayer skyrmion crystal with filling factor $\nu = 0.8$ and Zeeman coupling $\Delta_Z = 0.01(e^2/\ell)$ and is then independent of the interlayer separation. We expect the marked decrease in the spin polarization with bias to translate into an increase of the NMR relaxation rate with increasing bias.

Our numerical calculations show that crystals involving spin and/or pseudo-spin textures are likely candidates for the ground state of the 2DEG in a bilayer quantum Hall system around filling factor $\nu_T = 1$. At small tunneling and for $\nu_T < 1$, we find intertwined spin and pseudo-spin textures (CP3 crystal) with a spin polarization that is strongly interlayer dependent while at higher tunneling, a symmetric Skyrmion state

with fully polarized pseudo-spins or another type of spin-pseudo-spin state minimizes the energy. As was discussed in the previous section, a Skyrmion crystal has an extra gapless spin mode in the crystal phase and possibly in some over-damped form in a Skyrmion liquid state that is believed to be responsible for the rapid nuclear spin relaxation observed in the experiments (Fig. 3.17). This extra Goldstone mode is present both in the SS and CP3 crystal states that we studied in this section, but not in the bimeron or meron lattice states. To make a direct comparison with the NMR experiments, it is necessary to compute the NMR relaxation rate.

Results of such calculations are presented in ref.[41]. The inverse relaxation time $\mathrm{T}_1^{-1} \sim \int_{-\infty}^{\infty} dt \langle S_-(t) S_+ \rangle e^{-i\omega_N t}$ where ω_N is the nuclear magnetic resonance frequency.[42]. If the spin correlation function relaxes exponentially i.e., $\langle S_-(t) S_+ \rangle = \langle S_x^2 + S_y^2 \rangle e^{-t/\tau} = \langle S_{||}^2 \rangle e^{-t/\tau}$ then $T_1^{-1} \sim \rangle S_{||}^2 \langle \tau / (1 + \omega_N^2 \tau^2)$ is proportional to the in-plane spin polarization so that the behavior of spin polarization S_z should be an indication of the behavior of the relaxation time T_1. The rapid change in the spin polarization that we found in the CP3 crystal state (very small Δ_{SAS} for filling factors around $\nu_T = 1$) may explain the rapid change in the NMR relaxation rate measured in the experiment of [50] which was carried out at almost zero tunneling. Our Hartree-Fock calculation indicates that the ground state at higher tunneling is a SS state instead of a CP3 crystal. In this case, the spin polarization S_z varies much less rapidly with filling factor than for CP3 crystal. Moreover, the spin polarization does not depend much on the interlayer separation as can be seen, for example, in Fig. (3.27(b)). These results as well as a strong dependence on the interlayer separation would be more readily explained by a CP3 crystal state than by the SS state that we find. This is also true for their measurement of the relaxation rate in the presence of an applied bias. Figure (3.29) illustrates the in-plane component for various Zeeman couplings as a function of bias, which we believe is a measure of the NMR relaxation rate, for small Δ_{SAS}. The evident continuous behavior is reminiscent of the experimental results in shown in figure (3.20). This remarkable diagram illustrates how in the spin-pseudo-spin state one can manipulate the spin distribution using an interlayer bias.

Chapter 4

Activated Transport in Bilayer Systems

4.1 Introduction

In previous chapters we discussed the coherence of the electrons in a double quantum well system under strong magnetic field at total filling factor $\nu_T = 1$. We discussed how this system selects a new type of ground state in which electrons have a new degree of freedom, pseudo-spin. We also demonstrated how this system supports new types of low energy excitations in the pseudo-spin and spin sector. Transport in this system exhibits new features and challenging experimental results that need to be addressed. At filling factor $\nu_T = 1$ a single quantum well under strong magnetic field exhibits quantized Hall conductivity and zero longitudinal resistivity at low temperatures as was reviewed in the chapter 2. For a bilayer system at total filling factor $\nu_T = 1$, it is also expected the same features will be observed because the system is in a quantum state equivalent to that of a single quantum well state. In fact, it is now experimentally verified that the Hall conductivity in bilayer systems at total filling factor $\nu_T = 1$ is also quantized and the longitudinal resistivity vanishes at low temperatures.(Fig. 4.4).

In a typical experimental set up, quantum wells are formed in a thin ($\sim$ 15-20 nm) GaAs layer sandwiched between two AlGaAs layers with typical thickness of around 300 nm. The AlGaAs layers have different conduction band gaps causing the conduction band electrons supplied from Si-doped regions to become trapped in the quantum wells. The barrier (of thickness $\sim$ 12 nm) is typically an AlAs/GaAs layer in which the tunneling nearly vanishes. The intrinsic electron density trapped in these quantum wells can be measured and it is usually around 4×10^{10} cm^{-2}. All these crystal structures are grown using MBE technique offering an advantage over other crystal growth techniques which is growth in a controlled ultra high vacuum

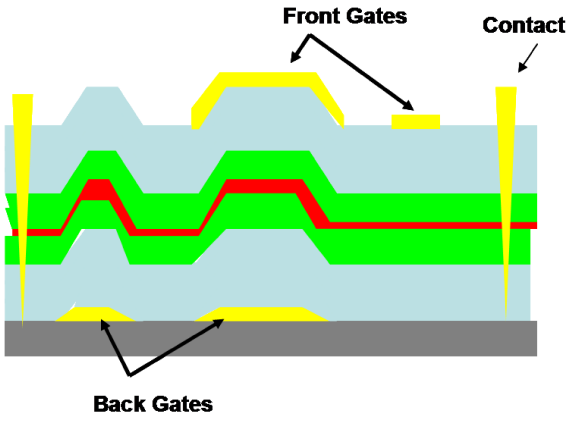

Figure 4.1: A schematic picture of a double quantum well heterostructure. The metallic gates are used to deplete the electron gases in top and bottom wells (green). The contacts are used to make electrical contact to each electron gas. The red layer is the barrier layer.

environment. This provides samples with relatively low disorder in which the mobility can exceed 400000 cm^2/Vs at the required densities. The low disorder is crucial because one needs to avoid localization before reaching the required magnetic fields.

In order to measure resistivity in different directions in each layer one has to be able to make contact to each layer separately. In order to do that, electrical contacts to the quantum wells are made by thermally evaporating Au/Ge on photolithographically defined regions of the mesa and then annealing the metal. This allows it to diffuse down into the crystal and through the quantum wells (see figure 4.1). Through such contacts electrical access to both electron gases is possible at the same time. In order to make contact to each quantum well separately, Eisenstein first realized [44] that it is possible to block the electrical contact to an arbitrary well by depleting the electron gas using another metallic (Cr/Au) gate that has been deposited on top or below the bilayer structure. For full experimental details, complications and methods we refer the reader to literature [44].

4.2 Excitonic Superfluid

At $\nu_T = 1$ in the bilayer system the filling factor of the lowest Landau level in each layer is smaller than one. Consequently each layer has a number of holes at the same

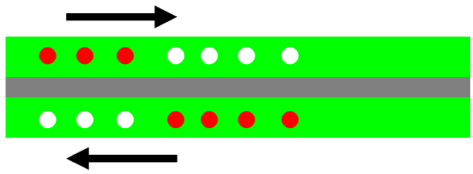

Figure 4.2: A schematic picture of a counterflow in a double quantum well. Arrows show the direction of electron (red) movement. The counterflow will move electron-hole (red-white) pairs.

energy level. One expects the holes to be able to pair with the electrons in the other layer to form a gas of *excitons*. The quantum state of an exciton formed by two fermions is a boson, hence in principle this gas can bose condense and become an *excitonic condensate*. This is equivalent to phase coherence in the bilayer system. To see this note that the ground state wave function of the bilayer system is

$$|\Psi\rangle = \prod_X \left[c^\dagger_{X,\uparrow} + e^{i\varphi} c^\dagger_{X,\downarrow}\right]|0\rangle \tag{4.1}$$

in which $\uparrow(\downarrow)$ refers to electron being created in upper(lower) layer. This state can be seen as a collection of paired electrons($\uparrow$) and holes($\downarrow$) with the same wave vector ($k = X/\ell^2$) or as a coherent state of two electron fluids which translates to all electrons in the two well having the same pseudo-spin state ($|\rightarrow\rangle = |\uparrow\rangle + |\downarrow\rangle$).

The superfluid aspect of the bilayer system has been subject of research in recent years. In order to drive this excitonic state one needs to inject counterflow currents in the bilayer system. In a counterflow distribution the current has the same magnitude but with opposite direction in each layer (Fig. 4.2). If the ground state of the system is an excitonic superfluid one expects the counterflow which drives neutral excitons to be dissipationless and display vanishing Hall resistance. On the other hand a parallel flow would derive the $\nu_T = 1$ quantum Hall liquid state and must show quantized Hall conductivity and zero longitudinal resistivity. Figure (4.3) shows the results of measurement of counterflow and parallel flow Hall and longitudinal resistivity at different filling factors at 30 mK. At $\nu_T = 1$ the counterflow Hall resistivity has clearly vanished signalling the fact that the current is carried by neutral particles. The longitudinal resistivity on the other hand is nearly zero in both cases. In figure (4.4) we see that as temperature decreases the longitudinal and Hall resistivity in counterflow measurement decreases indicating a condensate state at zero temperature.

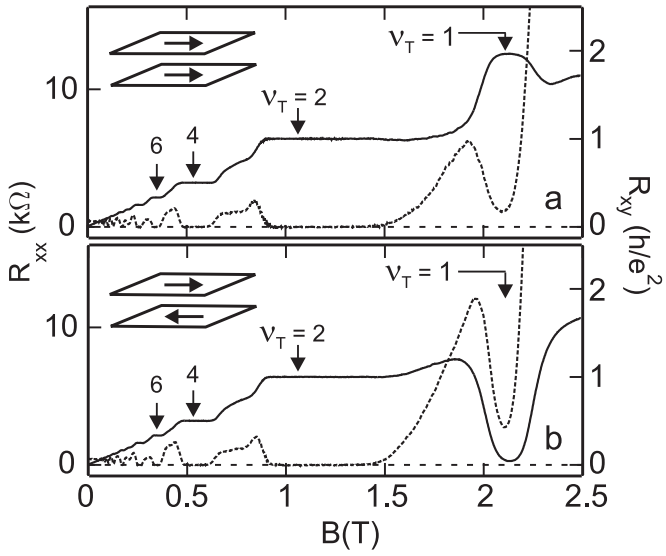

Figure 4.3: Hall and longitudinal resistances (solid and dotted traces, respectively) in a low density double-layer 2DES at T=50 mK. (a) Currents in parallel in the two layers. (b) Currents in counterflow configuration. Resistances determined from voltage measurements on one of the layers. After [53]

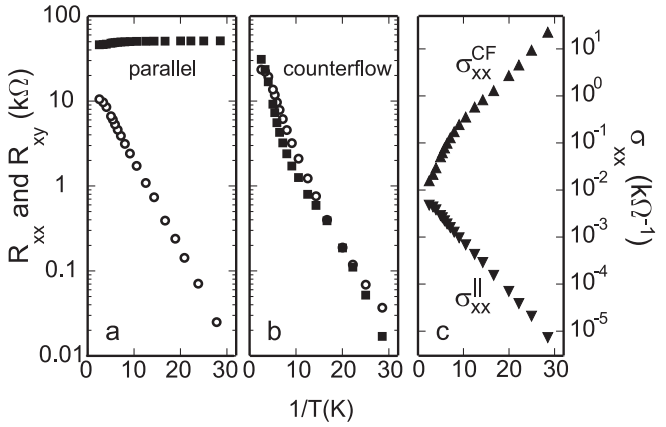

Figure 4.4: Temperature dependencies of various resistances and conductivities at $\nu_T = 1$ and $d/\ell = 1.48$. (a) Parallel current flow. Open dots: $R^{||}_{xx}$; closed squares: $R^{||}_{xy}$. (b) Counterflow. Open dots R^{CF}_{xx} , closed squares R^{CF}_{xy} . (c) Parallel and counterflow longitudinal conductivities, $R^{||}_{xx}$ and R^{CF}_{xx} , respectively. After [53]

The fact that no superfluidity has been observed at any finite temperature needs to be explained.

Another signal of superfluidity in this system was mentioned in the beginning of the previous chapter: the interlayer tunneling peak at zero bias. This effect is similar to the tunneling peak observed in conductance between superconducting islands known as DC Josephson effect [54]. However in the case of bilayer systems this peak remains finite even at very low temperatures, contrary to superconductors where it is infinite. There is still debate on what is the underlying explanation for this *imperfect superfluidity*. In this chapter we will only discuss the parallel and counterflow dissipation and on the subject of tunneling refer the reader to literature[59; 58; 69].

At the moment there are very few theories trying to explain the finite temperature dissipation of excitonic superflow. In this chapter we will develop two different theories both arguing that disorder and topological excitations (vortices) have an essential role in dissipation of superflow.

In transport measurements each quantum well can be contacted separately. In a so called *drag geometry* current is injected only into one layer and longitudinal and Hall resistivities are measured in each layer separately. Because of the Coulomb interaction between the electrons in different layers the moving electrons on the current carrying layer(*drive layer*) induces a voltage drop in the other layer(*drag layer*) which is called *drag resistivity*. Because electron gases in both layers together make one single quantum state, one expects the Hall resistivity in the drag layer to be quantized as well as in drive layer. This has been indeed observed as seen in figure 4.5. The main motivation behind our theories however has been the measurement[56] of the temperature dependent resistivity in drag geometry. This measurement has been performed for various layer imbalances. Imbalance between two layers can be created using the large metallic full front and back gates. By application of suitable voltages one can tune the density of each layer separately using these gates. The activation energies as a function of interlayer imbalance are shown in figure 4.6. The drive activation energy is almost linear and antisymmetric with respect to interlayer imbalance. The other linear plot is for when the drag and drive layers have been interchanged. In this plot, the drag activation energy looks almost symmetric. The most naive interpretation of this result would be that each layer has separate charged excitations, leading to the different activation energies, and interlayer coherence essentially plays no role. Yet such a picture is very difficult to reconcile with the experiments described above, in which imperfect superfluidity is manifest. In other words it is expected that the

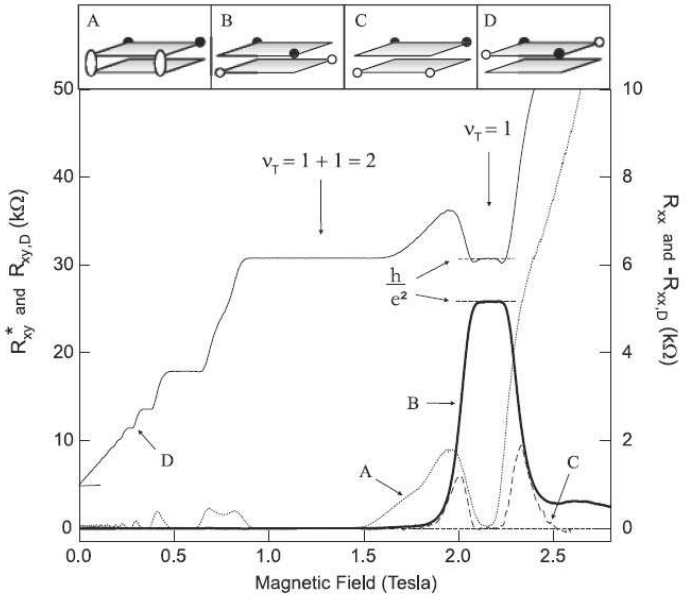

Figure 4.5: Conventional and Coulomb drag resistances of a low density double layer 2DES. Trace A: Conventional longitudinal resistance R_{xx} measured with current in both layers. Trace B: Hall drag resistance $R_{xy,D}$. Trace C: Longitudinal drag resistance $R_{xx,D}$; sign reversed for clarity. Trace D: Hall resistance R^*_{xy} of the single current-carrying layer (displaced vertically by 5 kV for clarity). Trace B reveals the quantization of Hall drag in the $\nu_T = 1$ excitonic QHE. Insets schematically illustrate the measurement configurations: Current is injected and withdrawn at the open dots; voltage differences between the solid dots are recorded. Traces A, B, and D obtained at $T = 20mK$; trace C at 50 mK. Layer densities: $N1 = N2 = 2.6{\times}10^{10}$ cm^{-2}, giving $d/\ell = 1.6$ at $\nu_T = 1$. After [55].

excitations have the responsibility for dissipation in both layers and consequently the activation energy for them should behave the same in either layer.

4.3 Role of Disorder

Although trapped electron gasses in today's semiconductor quantum wells have mobilities exceeding 400000 cm^2/Vs we believe the remaining disorder can play an important role in dissipation. There are some theoretical works in support of this suggestion[57]-[62]. The remote dopants such as Si atoms can form a slowly varying random external potential for the electron fluid. Based on the Efrös model[70; 71],

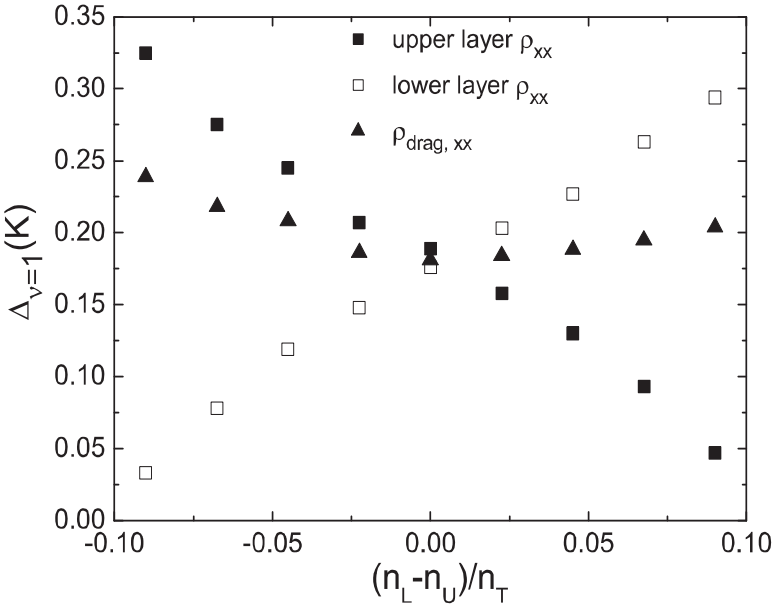

Figure 4.6: Activation energies of the $\nu_T = 1$ state vs density imbalance. Squares correspond to the activation energy determined from the longitudinal resistance in the lower and upper layer, respectively. Triangles denotes the activation energy obtained from the longitudinal drag. After [56].

these spatial fluctuations are screened nonlinearly by the incompressible $\nu_T = 1$ electron fluid. This screening generates puddles or islands each one having density higher or lower than average $\nu_T = 1$ density4.7. Consequently these puddles must contain a finite density of charged excitations of bilayers. At relatively large Zeeman energies we neglect any spin fluctuations and assume that these excitations are bimerons (see previous chapter). Inside puddles with $\nu_T > 1$ there are bimerons (meron pairs) and inside puddles with $\nu_T < 1$ there are anti-bimerons (anti-meron pairs). Between the puddles there are narrow regions that still have their total filling factor $\nu_T = 1$. These strips have a width of approximately a magnetic length ℓ. These incompressible strips follow the equipotentials of the total effective potential and are the only regions where there is still coherence left and there is a charge gap for excitations. On the other hand the quantum coherence is locally lost inside puddles because of the random motion of mobile bimerons. At the edges of the coherent strips merons and anti-merons from two neighboring puddles are weakly paired (Fig. 4.7). These pairs can not cross the incompressible links at zero temperature because they have to overcome the charge gap inside the strips. At high enough temperatures however this barrier can be overcome and a meron (anti-meron) can cross these strips.

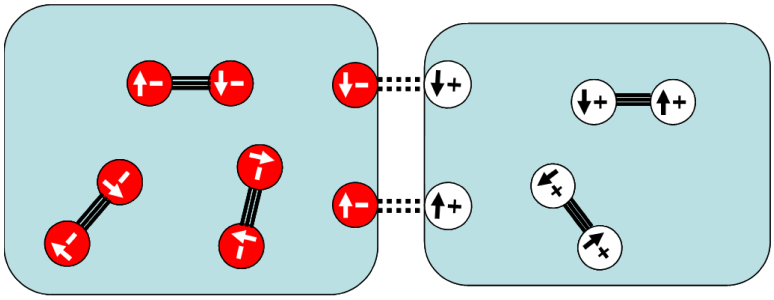

Figure 4.7: Schematic picture of two neighboring puddles inside a $\nu_T = 1$ bilayer system. Red objects are merons with vectors indicating their dipole moment direction (which is perpendicular to the plane of puddles) and signs indicating their electric charge. The white objects are anti-merons.

A meron is a vortex in pseudo-spin phase or equivalently in the phase of the exciton condensate wave function in analogy to 2D superfluids. In this analogy a supercurrent (in this case an exciton current) will apply a *Magnus* force[67] on vortices (merons) transverse to the supercurrent direction. The appearance of Magnus force is very general and has nothing to do with quantum mechanics (it was originally discovered in classical fluids[67]). In a 2D neutral superfluid with the fixed boundary condition (uniform flow $\mathbf{v} = \frac{\hbar}{m^*}\nabla\varphi$ at the boundaries or equivalently constant current at the two ends of the Hall bar) a vortex placed in this fluid will feel a Magnus force of magnitude

$$\mathbf{F}_M = \rho\mathbf{v} \times \hat{n} \tag{4.2}$$

in which ρ is the density of the neutral fluid forming the vortex and $\hat{n} = \hat{z}\oint \mathbf{v}\cdot d\mathbf{l}$ is perpendicular to the plane of the superflow. The motion of vortex perpendicular to the flow (as in eq. 4.2) produces a voltage drop along the direction of the flow. This occurs because the passage of a vortex across the flow produces a phase slip of 2π along the flow, and the rate of change of the phase is directly proportional to the voltage. However this is not all that determines the dynamics of merons. In order to completely understand the dynamics of merons in a bilayer quantum Hall system we need to remember that these merons have electric charge and one needs to take this into account in a systematic way. We will address this using Chern-Simon Theory in the next section.

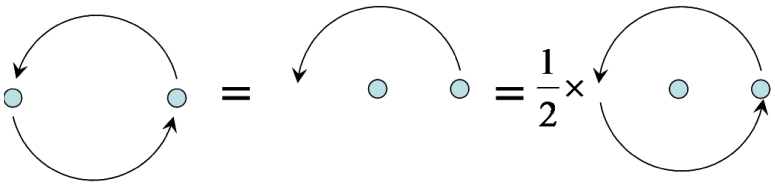

Figure 4.8: Operation of exchange of two indistinguishable particles is equivalent to half the rotation of one around the other.

4.4 Chern-Simon Theory for Quantum Hall Systems

In this section we are going to show how one can use boson statistics for fermions in two dimensions and what is the consequences of this view in quantum Hall systems. A detailed, mathematically rigorous Chern-Simon theory is unnecessary for our purposes here and is out of the scope of this dissertation[72]. However we will try to lay out a simplified view in order to be able to use it for our bilayer system.

Imagine two spinless fermions on a two dimensional surface. The wave function of this two body system must be antisymmetric

$$\Psi(\mathbf{r}_1, \mathbf{r}_2) = e^{i\pi}\Psi(\mathbf{r}_2, \mathbf{r}_1) \tag{4.3}$$

In two dimensions one can imagine this property of the wave function as arising from the Aharanov-Bohm phase induced by an external magnetic vector potential. This can be justified by noting that the operation of exchanging of two particles can be regarded as half the operation of rotating one around the other (see figure 4.8). The induced Aharanov-Bohm phase then will be

$$\phi_{AB} = \frac{e}{2\hbar}\oint \mathcal{A}\cdot d\mathbf{l} = \frac{e\Phi}{2\hbar} \tag{4.4}$$

in which the integral is over the closed loop as seen in figure (4.8) and Φ is the magnetic flux. For this phase we should have $\phi_{AB} = \pi$ which yields

$$\Phi = \phi_0. \tag{4.5}$$

in which $\phi_0 = h/e$ is a quantum of magnetic flux. In conclusion we see that in two dimensions fermionic statistics can be constructed by using a charged boson (with charge e) with a fake magnetic flux quantum. The important notion here is that the exchange operation is merely statistical and only limits the properties of the wave function independent of the Hamiltonian while the Aharanov-Bohm phase interpretation automatically includes the Hamiltonian. This is basically telling us

that converting fermions to bosons plus magnetic flux is Hamiltonian dependent and so its process will be different for different many body systems. In fact there is a method to include the many body effects into account in a more systematic way. Below we will briefly explain such a method for the quantum Hall effect. Consider N spinless electrons in a two dimensional layer under strong magnetic field. The Hamiltonian of such a system is

$$\hat{\mathcal{H}} = \sum_{i=1}^{N} \frac{1}{2m}[\mathbf{p}_i + e\mathbf{A}(\mathbf{r}_i)]^2 + \sum_i eA_0(\mathbf{r}_i) + \sum_{i<j} V(\mathbf{r}_i - \mathbf{r}_i) \tag{4.6}$$

One can show rigorously that this Hamiltonian operator can be rotated to a new Hamiltonian for a bosonic system with an extra as yet undetermined gauge field $\mathbf{a}(\mathbf{r}_i)$

$$\hat{\mathcal{H}}' = \sum_{i=1}^{N} \frac{1}{2m}[\mathbf{p}_i + e\mathbf{A}(\mathbf{r}_i) + e\mathbf{a}(\mathbf{r}_i)]^2 + \sum_i eA_0(\mathbf{r}_i) + \sum_{i<j} V(\mathbf{r}_i - \mathbf{r}_i) \tag{4.7}$$

in which we require

$$\mathbf{a}(\mathbf{r}_i) = \frac{\phi_0}{2\pi}\frac{\theta}{\pi}\sum_{j\neq i} \nabla_i \alpha_{ij} \tag{4.8}$$

where ϕ_0 is the quantum of flux and θ will be determined later. The derivatives ∇_i are with respect to $\mathbf{r}_i$ and angles are

$$\alpha_{ij} = \tan^{-1}\frac{y_j - y_i}{x_j - x_i}. \tag{4.9}$$

The eigenfunctions of the fermionic Hamiltonian $\Psi(\mathbf{r}_1, \mathbf{r}_2, ..., \mathbf{r}_N)$ are antisymmetric while the eigenfunctions of the bosonic Hamiltonian $\Phi(\mathbf{r}_1, \mathbf{r}_2, ..., \mathbf{r}_N)$ are symmetric. The operator that rotates $\hat{\mathcal{H}}$ to $\hat{\mathcal{H}}'$ is

$$U = \exp\Big[i\sum_{i<j}\frac{\theta}{\pi}\alpha_{ij}\Big]. \tag{4.10}$$

One can show that

$$\mathcal{H} = U\mathcal{H}'U^{-1} \tag{4.11}$$

which means that if one can solve the bosonic problem and find its eigenfunctions Φ with eigenvalues E then

$$\Psi = U\Phi \tag{4.12}$$

is an eigenfunction of $\mathcal{H}$ with the same eigenvalue as E. The parameter θ will be adjusted by imposing the correct statistics for Ψ. To connect bosons to fermions we require θ to be an odd multiple of π

$$\theta = (2k+1)\pi. \tag{4.13}$$

From the above discussion it is clear that the rotation operator in fact contributes a phase $e^{\pm i\theta}$ when two particles are exchanged. The vector potential $\mathbf{a}$ interacts with the bosons and this phase transformation arises as the Aharanov-Bohm phase. From equations (4.8) and (4.9) we can find the desired gauge field

$$a_\alpha(\mathbf{r}_i) = \frac{\phi_0}{2\pi}\frac{\theta}{\pi}\epsilon_{\alpha\beta}\sum_{j\neq i}\frac{(x_j - x_i)_\beta}{|\mathbf{r}_i - \mathbf{r}_j|^2}. \tag{4.14}$$

This vector potential can be interpreted as coming from the field $\mathcal{A}(\mathbf{r})$ created by a particle at point $\mathbf{r}_j$ acting on the particle at position $\mathbf{r}_i$.

$$\mathcal{A} = \frac{\phi_0}{2\pi}\frac{\theta}{\pi}\Big(\frac{-y}{|\mathbf{r}|^2}, \frac{x}{|\mathbf{r}|^2}\Big) = \frac{\phi_0}{2\pi}\frac{\theta}{\pi}\frac{1}{r}\mathbf{e}_\varphi \tag{4.15}$$

is the vector potential with the strength $\phi_0\frac{\theta}{\pi}$ at the origin with the associated magnetic field

$$\nabla \times \mathcal{A} = \phi_0\frac{\theta}{\pi}\delta(\mathbf{r})\hat{z} \tag{4.16}$$

For an arbitrary closed path C around the origin we obtain

$$\Phi = \oint_C \mathcal{A}(\mathbf{r})\cdot d\mathbf{l} = \phi_0\frac{\theta}{2\pi} \tag{4.17}$$

which is the flux associated with this vector potential.

Equation (4.14) can be written as

$$\mathbf{a}(\mathbf{r}_i) = \sum_{j\neq i}\mathcal{A}(\mathbf{r}_i - \mathbf{r}_j). \tag{4.18}$$

Consequently a particle at position $\mathbf{r}_j$ can be regarded as the source of the magnetic flux $\phi_0(\theta/\pi)$, creating a vector potential at $\mathbf{r}_i$. As was mentioned the exchange of two particles is equal to half a rotation of one around the other and the Aharanov-Bohm phase change of their wave function would be

$$\Delta\phi_{AB} = \frac{e}{2\hbar}\oint_C \mathcal{A}(\mathbf{r}_2 - \mathbf{r}_1)\cdot d\mathbf{r}_2 = \frac{e}{2\hbar}\phi_0\frac{\theta}{\pi} = \theta \tag{4.19}$$

which means for fermions it should be $\theta = \pi$. However for more general discussions we keep θ unspecified.

In order to be able to use reliable approximations it is useful to express the bosonic representation of the electronic system using second quantized formulation

$$\begin{aligned}\hat{\mathcal{H}}' &= \int d^2r\phi^\dagger(\mathbf{r})\Big\{\frac{1}{2m}\Big[-\frac{i}{\hbar}\nabla + e\mathbf{A}(\mathbf{r}) + e\mathbf{a}(\mathbf{r})\Big]^2 - \mu + eA_0(\mathbf{r})\Big\}\phi(\mathbf{r}) \\ &+ \frac{1}{2}\int d^2r d^2r'\rho(\mathbf{r})V(\mathbf{r}-\mathbf{r}')\rho(\mathbf{r}').\end{aligned} \tag{4.20}$$

Here $\phi(\mathbf{r})$ is the bosonic creation operator

$$[\phi(\mathbf{r}), \phi^\dagger(\mathbf{r}')] = \delta(\mathbf{r} - \mathbf{r}'), \tag{4.21}$$

and $\rho(\mathbf{r}) = \phi^\dagger(\mathbf{r})\phi(\mathbf{r})$ is the particle density. The Chern-Simon gauge field then will have the form

$$\mathbf{a}(\mathbf{r}) = \int d^2\mathbf{r}' \mathcal{A}(\mathbf{r} - \mathbf{r}')\rho(\mathbf{r}'). \tag{4.22}$$

which yields

$$\hat{z}b(\mathbf{r}) = \nabla \times \mathbf{a}(\mathbf{r}) = \phi_0 \frac{\theta}{\pi} \rho(\mathbf{r})\hat{z}. \tag{4.23}$$

as the Chern-Simon magnetic field density proportional to the particle density ρ. This is indicating that to every boson one gauge flux $(\theta/\pi)\phi_0$ is attached and the combination of the two will make a fermion.

The above discussions introduces a systematic way to include the Chern-Simon gauge field into the problem of a fermionic system in two dimensions. Note that the importance of dimensionality is apparent here when one wants to use the Aharanov-Bohm effect to derive the correct statistics as was mentioned in the beginning of this section.

In summary we have learned that one can replace the two dimensional electron system with a system of charged bosons that are interacting with each other via a short-range repulsive force expressed as a gauge term in the Hamiltonian called the Chern-Simon gauge field. In a simple mean field approximation and for the case where the external magnetic field is constant $\nabla \times \mathbf{A} = -B\hat{z}$ one can neglect the density fluctuations and estimate the average magnetic field at each point as

$$\overline{\mathbf{B}} = -B\hat{z} + \phi_0 \frac{\theta}{\pi} \overline{\rho}\hat{z}. \tag{4.24}$$

At filling factor ν we will then have

$$\overline{\mathbf{B}} = B(\frac{\nu\theta}{\pi} - 1)\hat{z} \tag{4.25}$$

which indicates that at $\nu = 1$ we can choose $\theta = \pi$ which makes $\overline{\mathbf{B}} = 0$. Consequently the 2D electron system in constant magnetic field at $\nu = 1$ will be equivalent to the mean field approximation of a charged bosonic system with Chern-Simon gauge field with *zero* total magnetic field. This will immediately suggest that this system may bose condense and become a superfluid. Using this fact one will be able to derive all properties of the quantum Hall system including zero longitudinal resistivity and quantized Hall conductivity.

Now let's go back to eq.(4.25) in which we choose $\theta = \pi$. From this equation we see that adding(removing) a charge to(from) the $\nu = 1$ system is equivalent to adding(removing) a quantum of magnetic flux to(from) the system. This is the same property discussed in the chapter 2 where spin configuration actually provided an additional flux equivalent to additional charge with the assumption that the Hall conductivity is quantized however we have gone through a reverse argument here and did not use the quantized Hall conductivity assumption.

4.5 Dynamics of Merons in Bilayer System

According to the discussions above we can interpret a $\nu_T = 1$ bilayer as a system of bosons each having a flux quantum attached to them. The magnetic field providing this flux is anti-parallel to the external magnetic field (eq.4.24). On average the total magnetic field on this bosonic system then will be zero and we will have a $\nu_T = 1$ bose condensate (a superfluid). Bosons in this condensate however have another degree of freedom, their pseudo-spin. One may also view this *composite boson condensate with a pseudo-spin degree of freedom* as a *composite boson condensate together with an excitonic condensate.*(see section 4.2)

In this section we are going to calculate the forces on merons for any current distribution in a bilayer system. As was discussed in section 4.3 from these dynamics we will be able to find the dissipation mechanism and may be able to explain the observed activation energies.

Let's take $\mathbf{J}_U$ and $\mathbf{J}_L$ as current densities in the upper and lower layers respectively. This current distribution has two components: a parallel flow component, $\mathbf{J}_{||} = (1/2)(\mathbf{J}_U + \mathbf{J}_L)$ and a counterflow $\mathbf{J}_{CF} = (1/2)(\mathbf{J}_U - \mathbf{J}_L)$. As was mentioned in the section 4.3 a meron will feel a Magnus force from the counterflow in analogy to fluid dynamics. On the other hand from the discussion in the previous section we understand that addition of a charge to the $\nu = 1$ quantum Hall system is equivalent to the addition of a flux quantum to the bosonic system. This should also be true for a charged excitation of the bilayer system. Consequently a bimeron or any charged excitation with total charge q will be carrying a Chern-Simon flux equal to $(q/e)\phi_0$. This magnetic flux will interact with the current that flows inside the $\nu_T = 1$ charged bosonic superfluid by the Lorentz force. These two forces (the Magnus force from excitonic superfluid and the Lorentz force on the $\nu_T = 1$ charge flow) will determine

the motion of merons. In order to derive these forces first we consider the general imbalanced bilayer (relevant to biased bilayer experiments mentioned in the beginning of this chapter) with filling factors ν_U and ν_L for upper and lower layers respectively. The charge of merons in this case can be determined according to the table 4.1. The Magnus force due to the counterflow (Eq. 4.2) is

$$\mathbf{F}_M = -(s\phi_0)\mathbf{J}_{CF} \times \hat{z}, \tag{4.26}$$

in which $s = \frac{1}{2\pi}\oint \nabla\varphi \cdot d\mathbf{l}$ is the vorticity, ϕ_0 is the quantum of flux and the minus sign is because $\mathbf{J}_{CF}$ is the current density of electron charge (-e) . It is also important to note that we are defining the currents as the current of electrons moving in the lab frame while we should use the counterflow with respect to the $\nu_T = 1$ bosonic system as the background. In order to find the velocity of the excitons with respect to this background first we note that the velocity of the electrons in the background system with respect to the lab frame is

$$\mathbf{v}^{Lab}_{back} = \frac{2\pi\ell^2}{-e\nu_T}\mathbf{J}_{||}. \tag{4.27}$$

To determine the velocity of excitons with respect to the lab frame we can assume $\nu_U > \nu_L$ without loss of generality

$$\mathbf{v}^{Lab}_{exciton} = \frac{2\pi\ell^2}{-e\nu_L}\mathbf{J}_L. \tag{4.28}$$

Consequently the exciton(counterflow) current density with respect to the background will be

$$\begin{aligned}
\mathbf{J}^{rel}_{CF} &= \frac{-e\nu_L}{2\pi\ell^2}\mathbf{v}^{rel}_{exciton} \\
&= \frac{-e\nu_L}{2\pi\ell^2}(\mathbf{v}^{Lab}_{exciton} - \mathbf{v}^{Lab}_{back}) \\
&= \frac{s\phi_0}{\nu_T}[\mathbf{J}_U - \nu_U(\mathbf{J}_U + \mathbf{J}_L)].
\end{aligned} \tag{4.29}$$

As we mentioned the free topological excitations(merons) carry a flux which results in a Lorentz force from the charged bosonic background current. This force can be written as

$$\mathbf{F}_{Lorentz} = -(q\phi_0)\mathbf{J}_{||} \times \hat{z} \tag{4.30}$$

in which q is the charge of the meron that has to be determined in a general imbalanced bilayer case using the table (4.1). From the equations (4.30) and (4.29) we conclude that the total force on a meron from any current distribution in bilayer system is

$$\mathbf{F}_{meron} = \frac{\phi_0}{\nu_T}\{[(1-\nu_L)s - q\nu_T]\mathbf{J}_L - [s\nu_L + q\nu_T]\mathbf{J}_U\} \times \hat{z}. \tag{4.31}$$

s	+1	+1	-1	-1
p	+1	-1	+1	-1
q_{sp}	$-\nu_L$	ν_U	ν_L	$-\nu_U$

Table 4.1: Electrostatic charge of each type of meron in units of e. ν_U, ν_L are the upper and lower filling factors respectively. s and p are vorticity and dipole moment respectively.

At $\nu_T = 1$ using the table (4.1) we find that in a drag experiment ($J_U = J$ and $J_L = 0$) the force on two types of merons with the same dipole moment ($p = +1$) vanishes ! This indicates that for the drag geometry merons of only one dipole moment type are able to dissipate current. On the other hand, because merons have a dipole moment, their activation barrier energy in the presence of an interlayer bias must be linear in lowest order approximation in bias V

$$\Delta_{meron} \approx \Delta_0 + pV \tag{4.32}$$

in which p is the meron dipole moment. Consequently if one varies the interlayer bias the observed activation energy must behave *asymmetrically* which agrees with experiment as is seen in figure (4.6). The detailed behavior of the energy barrier can be calculated numerically as will be explained in the next section. To complete this analysis one has to calculate the voltage drop in each layer explicitly.

In a general current distribution we consider ΔV_U and ΔV_L as the voltage drops inside the upper and lower layers between two points a distance y apart as a result of transverse meron motion. Using an analogy to the Josephson effect in a weak link inside a superconductor for a density n_{sp} of merons with vorticity s and dipole p we will have

$$\frac{-e}{\hbar}\Delta V = \frac{d\varphi}{dt} = 2\pi s n_{sp} u_{sp} y \tag{4.33}$$

in which φ is the phase of the exciton condensate and u_{sp} is the velocity of the merons. Because this voltage drop is in a exciton (a particle-hole pair) condensate $\Delta V = \Delta V_U - \Delta V_L$. Taking into account all the meron types

$$\frac{1}{y}[\Delta V_U - \Delta V_L] = -\phi_0 \sum_{s,p} s n_{sp} u_{sp}. \tag{4.34}$$

On the other hand the motion of meron means motion of a magnetic flux in the bilayer system which induces a voltage drop according to Faraday's law

$$\frac{-e}{\hbar}\Delta V = 2\pi y \sum_{s,p} n_{sp} u_{sp} q_{sp} \tag{4.35}$$

in which ΔV is the total voltage drop in both layers: $\Delta V = \nu_U \Delta_U + \nu_L \Delta_L$. Consequently

$$\frac{1}{y}[\nu_U \Delta V_U + \nu_L \Delta V_L] = -\phi_0 \sum_{s,p} q_{sp} n_{sp} u_{sp}. \tag{4.36}$$

For the drag geometry($J_L = 0$) one immediately concludes that $\Delta V_L = 0$ and at $\nu_T = 1$

$$\Delta V_{drive} = y\phi_0^2(\mu_{V\uparrow} n_{V\uparrow} + \mu_{A\uparrow} n_{A\uparrow}) \tag{4.37}$$

in which we have defined $\mu = v/F$ as the effective mobility of merons.

In order to explain the voltage drop in the drag layer ($V_L \neq 0$) we must identify how forces on the $p = \downarrow$ merons might arise. A natural candidate for this is the interaction between merons with opposite vorticities, which in the absence of disorder binds them into pairs at low meron densities. Assuming that driven merons crossing incompressible strips will occasionally be a component of these bimerons, a voltage drop in the drag layer will result, of the same sign as that of the drive layer. The mobility of such bimerons is limited by the energy barrier to cross an incompressible strip. Since these strips are narrow compared to the size scale of the constituents of the bimeron, we expect the activation energy to be given approximately by the maximum of the activation energies for merons of the two polarizations $p = \uparrow, \downarrow$. This leads to a drag resistance much smaller than that of the drive layer, and an activation energy that is symmetric with respect to bias. Both these behaviors are observed in experiment[56; 68]. It is interesting to notice that, within this model, as samples become increasingly clean one expects such mobile bimerons to become more prominent relative to single merons, so that the voltage drop in the two layers will increasingly match with decreasing disorder. In principle a drag experiment in a sample clean enough that all merons are paired will result in precisely the same voltage drop in each layer, so that pure counterfow becomes dissipationless, and parallel flow dissipation occurs in a manner such that one cannot distinguish whether the electrons are moving in the upper or lower layer.

The most important difference between the Chern-Simon theory of bilayer dissipation presented here and other theories is the involvement of topological charges. Thus it is important to know how the energy barrier of incompressible links for these charges behaves as a function of various parameters as we discuss in the next section.

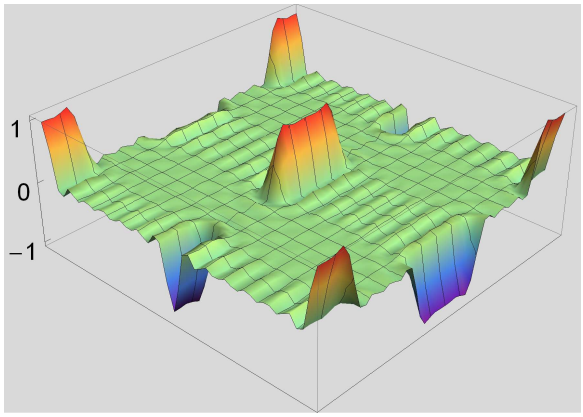

(a)

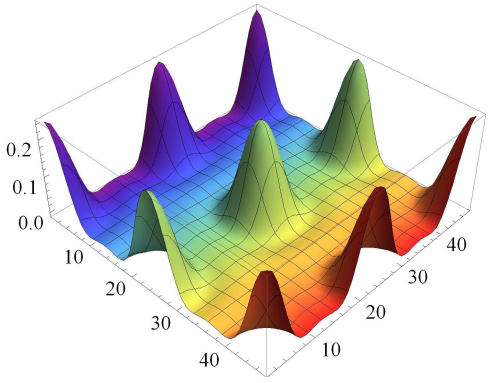

(b)

Figure 4.9: (a)Finite reciprocal lattice vector construction of a checkerboard strip bias potential with a width $\sim 1.04\ell$ for $\nu_T = 1.02$ lattice. The length of each strip is $\sim 10\ell$.(b) Unit cell of a lattice of merons for layer separation $d/\ell = 1$ at $\nu_T = 1.02$ and zero tunneling.

4.6 Model of Activation Barrier For Merons

In equilibrium, one expects the energy of merons residing in different puddles to be roughly equal. When a meron hops from one puddle to the next it must pass through an incompressible strip, where its energy is higher. Computing the activation energy directly for such a process is challenging because it is difficult to find the energy of a meron in a puddle with any precision. However, one can estimate the relative activation energy for merons to pass through the barrier region for different biases. In order to do this, we compute the energy of a lattice of merons in a commensurate potential, for which there is a strip with interlayer bias running directly through the center of every meron in the lattice (Fig. 4.9). By taking the difference in energy between configurations in which the meron polarizations are parallel and antiparallel to the bias potential, one arrives at an estimate for the bias dependence of the activation energy. We used the same method to derive the energy of topological excitations as in chapter 3.

To compare with experiment we wish to compute the energy difference as a function of the difference in filling factors for the layers, $\Delta\nu$. To accomplish this we also compute meron lattice states with a uniform bias, to estimate the $\Delta\nu$ associated with a given bias. Estimates of the incompressible strip width indicate that it should be of order ℓ, which is rather narrow compared to the size a meron for very small tunneling so we consider this situation in computing the bias dependence of the activation energy. Typical densities resulting from the calculations are illustrated in Figures (4.10(a),4.10(b)). Figure (4.10(a)) shows the density of a meron before applying the strip bias potential at $d/\ell = 1$ and zero tunneling. This distribution clearly has circular symmetry. Figure (4.10(b)) shows the density of the meron after applying the strip bias potential that creates an imbalance of $\Delta\nu/\nu_T \sim \%4.8$. As we can see the meron has lost the circular symmetry in trying to avoid the bias region. Figure (4.11)(b) shows the difference between the two densities where we can see that the meron has transferred part of the charge density away from the biased region. In fact, part of the charge has moved to the sides of the strip creating an asymmetry toward a direction perpendicular to the strip.

In our numerical derivation the initial condition for the meron had a vortex symmetry ($\rho(\mathcal{R}_\theta \mathbf{G}) = e^{i\theta}\rho(\mathbf{G})$). During all the iterations the solution kept this symmetry even in the presence of the strip bias without the need to enforce it. This indicates that the meron lattice solution is robust against the different variations of bias potential.

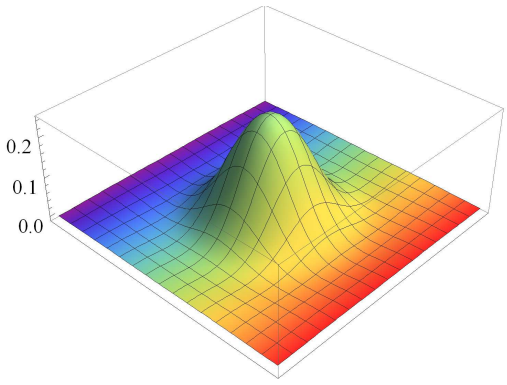

(a)

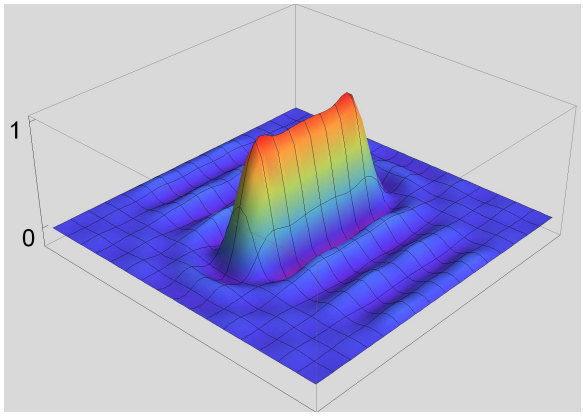

(b)

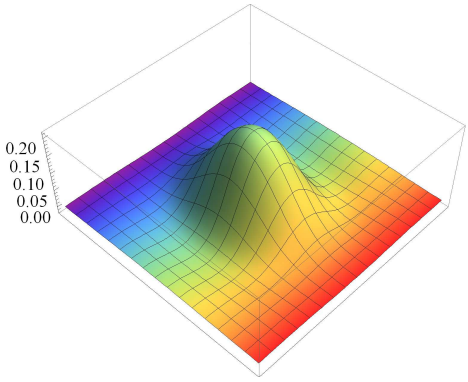

(c)

Figure 4.10: (a)Charge density of a meron at $d/\ell = 1$, $\nu_T = 1.02$ and zero tunneling. (b) The applied bias strip potential with a width of $\sim 1.04\ell$. (c) Charge density of meron after applying the bias strip potential that creates an imbalance of $\Delta\nu \sim \%4.8$.

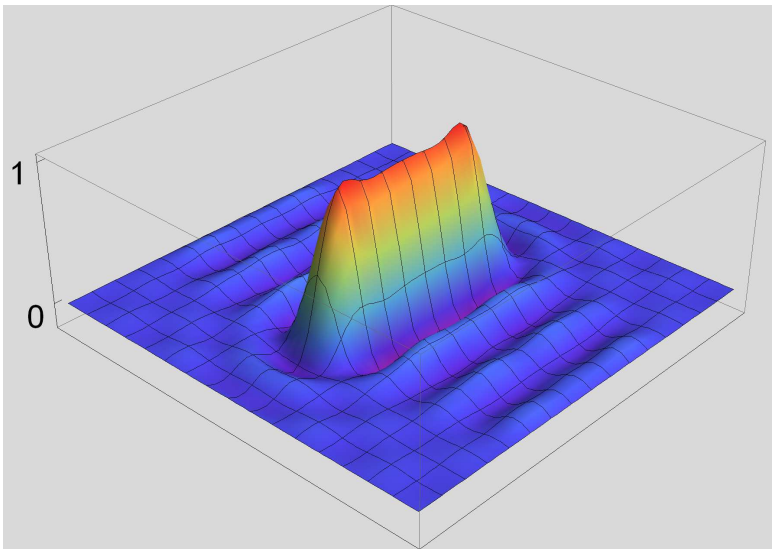

(a)

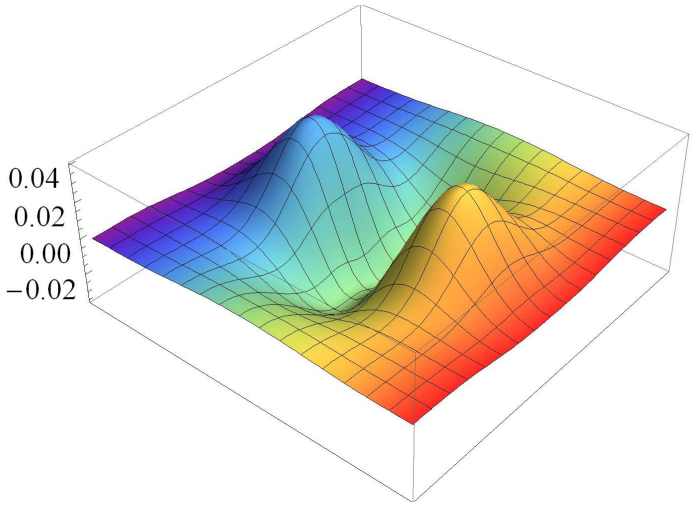

(b)

Figure 4.11: (a) The same potential as in figure 4.10(b) . (b) Difference of charge density of a meron after applying the potential with strength $v = 0.01e^2/\ell$ creating an imbalance of $\sim \%4.8$ at $d/\ell = 1.0$, $\nu_T = 1.02$ and zero tunneling.

Figures (4.12) shows the difference in charge density of a meron at a smaller separation $d/\ell = 0.5$ and zero tunneling with almost the same imbalance $\Delta\nu/\nu_T \sim \%4.6$. Clearly the change is much smaller than the case with larger separation. Physically, this difference is a result of the larger exchange energy for smaller layer separations, which makes it more difficult for merons to deform. Through such deformations, the electron density in the merons can avoid the most energetically expensive regions. On the other hand, for very small layer separation, the bias required to displace charge from one layer to the other becomes very small, so that for a fixed population imbalance $\Delta\nu$, the energy difference between the two polarizations must vanish as $d \to 0$. As a result, the activation energy for fixed $\Delta\nu$ is expected to be a *non-monotonic* function of d/ℓ as can be seen in figure (4.13). This is an important prediction that can be tested in experiment. Figure (4.14) shows the energy difference of a meron as a function of layer imbalance. The results are qualitatively quite similar to experimental observations although the overall magnitude is roughly a factor of 3 larger. Likely causes of this discrepancy are the absence of finite well-width corrections in our calculations, and the absence of quantum fluctuations which should lower the exchange stiffness in the incompressible strip. Discrepancies of this magnitude between Hartree-Fock calculations and measured activation energies are quite typical [63; 20] in quantized Hall systems. On the other hand this value decreases with decreasing the width of the strip bias potential as can be seen in figure (4.15). This indicates that the observed activation energies in experiments are indeed the energy barrier against merons hopping across the incompressible strips rather than their excitation energy out of the $\nu_T = 1$ vacuum and another reason why they are smaller than the actual calculated values in the numerical Hartree-Fock approximations.

Before we finish this section it is important to point out that it has been argued that the Lorentz force and Magnus force on a skyrmion in a single layer quantum Hall system are in fact equivalent and are two representations of the same force[64]. This argument is true and must be answered for the case of bilayer system. First we should remember that the Magnus force and Lorentz force come from two different *external current sources*, namely counterflow current and parallel flow current and one can distinguish between the two experimentally. Second it is possible to derive the dynamics of merons using a classical theory of vortex dynamics in ferromagnets [65]. In this theory *out-of-plane* vortices are defined as the vortices that have an out of plane component determining their polarity. Depending on the polarity one can show that these vortices will feel a force called *gyromagnetic force*. One can show that

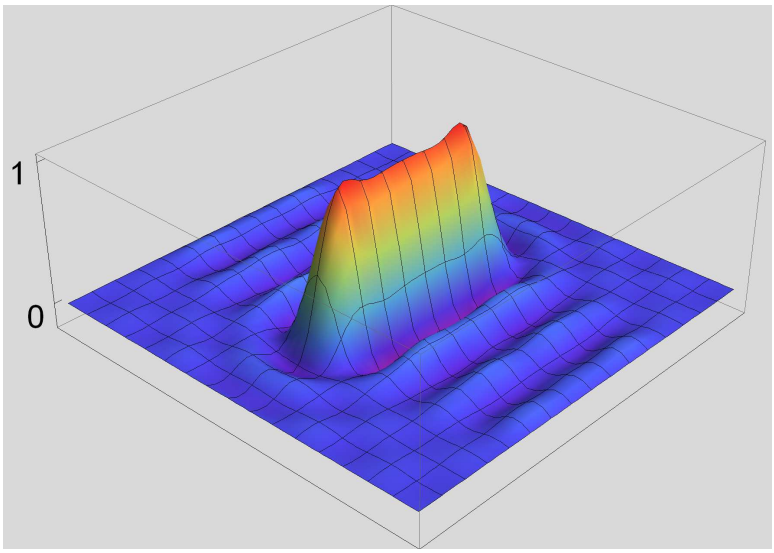

(a)

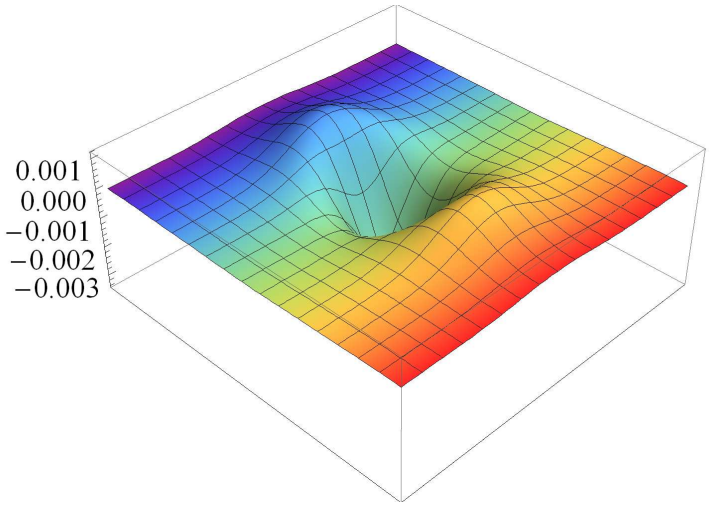

(b)

Figure 4.12: (a) The same potential as in figure 4.10(b) . (b) Difference of charge density of a meron after applying the potential with strength $v = 0.003e^2/\ell$ creating an imbalance of $\sim \%4.6$ at $d/\ell = 0.5$, $\nu_T = 1.02$ and zero tunneling.

in presence of any current distribution the Magnus and gyromagnetic force together give rise to the same total force as the one in equation (4.31).

4.7 Future Work

The presented theory in the last few sections is a new approach in analyzing the transport properties of the bilayer systems. This theory can be developed in so many different ways. The possible role of low but non-zero tunneling amplitude in activation energy of merons can be investigated using for example parallel magnetic field. As was discussed in chapter (3) in a sample with non-zero tunneling bimerons are lower in energy than merons. Bimerons on the other hand do not have an electric dipole moment consequently they don't respond to the interlayer bias which results in the disappearing of the asymmetric behavior in the activation barrier. It would also be interesting to know the response of a bimeron to a strip bias potential. Does the bimeron prefer to split into two separate merons? This may illustrate why disorder can unbind merons. This response can be studied by varying interlayer bias, tunneling and separation. On the other hand the role of spin has been completely ignored in this chapter. First of all one needs to find out what would be the response of the meron to strip potential when the Zeeman gap is low such that it allow the spin of electrons tilt away from majority direction in order to compensate for energy cost of the bias strip. On the other hand CP3 skyrmions are robust against interlayer bias as was illustrated in the previous chapter. The question then remains whether they are robust against the application of strip biases ? and how their energy will change. All these questions can be answered by extending the above numerical work and also by studying a possible spin-pseud-spin Chern-Simon theory for bilayer system. These questions also may in principle be studied by experiments.

4.8 Meron-Edge Theory, An Alternative?

The edge current in quantum Hall system has unique properties. In the above discussions edge current was totally ignored assuming that in the absence of backscattering there is no dissipation in the edge current. However throughout the whole theory it was assumed that the edge current is responsible for the quantized Hall conductance (as discussed in chapter 2). There is a serious concern among the Hall effect community about the role of edges of the Hall bar in the measured transport properties [66].

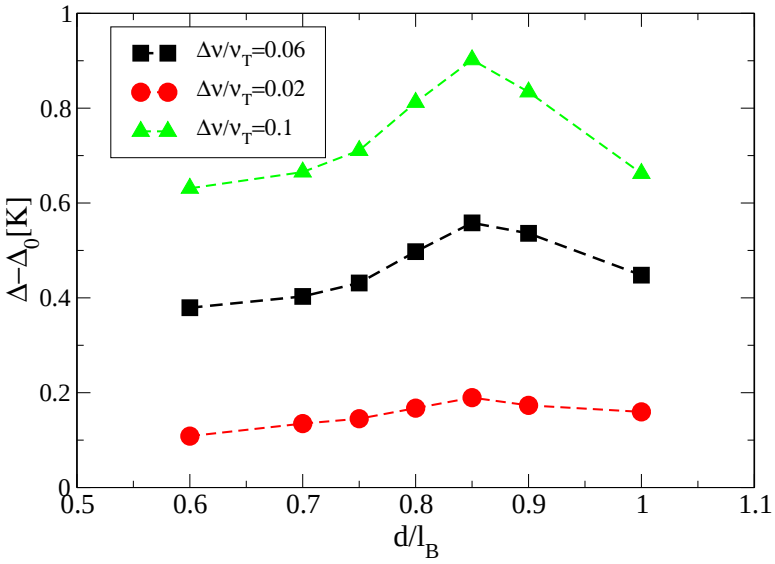

Figure 4.13: The energy barrier for a meron crossing a strip bias of width $\sim 1.04\ell$ as a function of layer separation for three different imbalances.

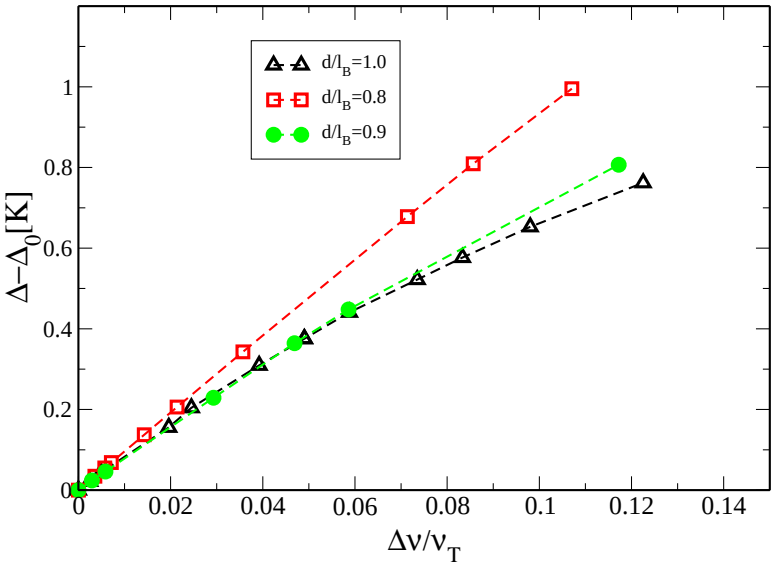

Figure 4.14: Energy barrier for a meron crossing a strip bias of width $\sim 1.04\ell$ as a function of layer imbalance for three different three different layer separations.

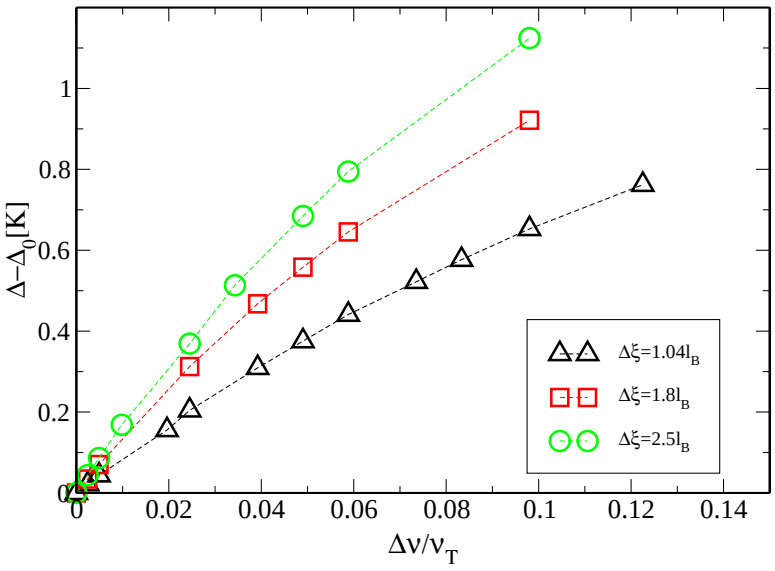

Figure 4.15: Energy barrier for a meron crossing a strip bias as a function of layer imbalance for three different strip widths $\Delta\xi$ at $d/\ell = 0.8$.

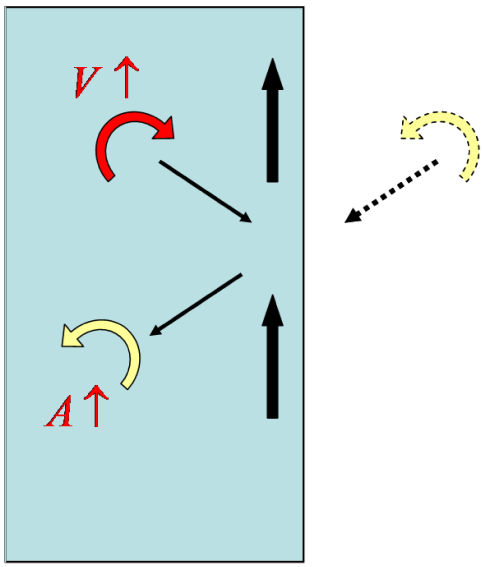

Figure 4.16: Schematic picture of one possible process through which a meron driven toward edge can be absorbed by edge current follwed by emission of a meron with opposite vorticity. The dashed drawing on the right is the image of the meron (vortex).

One of the reasons for this concern is that the contacts made to the electron fluid are first of all interacting with the edge current. In an attempt to interpret the activation energy results of the experiments (Fig. 4.6) one can consider the interaction of the edge current with the bulk in presence of merons. In this section we introduce an effective theory of meron-edge interaction and show that it is possible to explain the experimental results using this theory.

We assume the edge current possess two independent properties : local charge density $\rho(y) = \rho_U(y)+\rho_L(y)$ and pseudo-spin density $m(y) = \rho_U(y)-\rho_L(y)$. Assuming the system is in coherent quantum Hall regime the Hall resistivity is nonzero and quantized in both layers (fig. 4.5). Also we assume that the charge of merons are close to half the electronic charge independent of imbalance. This assumption is only true for small imbalances. Finally we consider the specific case of current in top layer $I_U \neq 0$ and in bottom layer $I_L = 0$.

One can view the current distribution as the sum of a counterflow and a parallel flow as was used before. The counterflow current drives excitons in the system so it couples to the excitonic superfluid. This current in the superfluid will produce a Magnus force (eq. 4.2) on the merons already present in the system, a force transverse to the direction of the current. This force drives vortices to one edge and anti-vortices to the other edge of the system. Voltage probes in a layer measure the local edge current at the leads. The charge and dipole moment of the driven merons at the edge will influence the local charge and pseudo-spin density of the edge and cause dissipation. The measured activation energies are then the energies of merons trying to overcome the incompressible barriers formed by disorder. This activation energy is numerically calculated in the previous section.

We use $n_\uparrow$, $n_\downarrow$, $p_\uparrow$ and $p_\downarrow$ to denote the charge densities associated with merons of the type $V^- \uparrow$, $A^- \downarrow$, $A^+_\uparrow$ and $V^+_\downarrow$ respectively. The $\pm$ sign indicate the charge of the meron. We assume there is no recombination inside a puddle and that the charge transfer between puddles occurs almost instantaneously in the steady state so the current density associated with any type of meron flowing into the edge will be: $j(x0) = \mu I_{CF} + \Gamma\delta n(x0)$ in which I_{CF} is the counterflow current, x_0 is the position of the last strip a meron has to hop across to reach the edge and μ is the effective mobility of the meron. We have assumed only the merons drift in the x-direction perpendicular to the current flow. Finally δn indicates the deviation from zero-current density, n_0. We assume this process is thermally activated, $\Gamma = \Gamma_0 e^{-\Delta/k_BT}$ and $\mu = \mu_0 e^{-\Delta/k_BT}$ in which the activation energy has been calculated in the previous section.

Assuming current flows in the top layer, the pseudo-spin of electrons at the edge are polarized toward top layer. The merons hopping the last energy barrier join the edge current. From a microscopic point of view it is very difficult to find out what happens to the local charge density when a meron enters the edge, however macroscopically, using basic physical principles we can argue in a semiclassical way that the edge current can absorb the charged merons: When a meron $V^- \uparrow$ is close to the edge, in order to satisfy the correct pseudo-spin boundary conditions one can imagine an image charge which has to be $A^+ \uparrow$ or $A^- \downarrow$ approaching the edge from outside (Fig. 4.16), edge current absorbs the $V^- \uparrow$ and $A^+ \uparrow$ or $A^- \downarrow$ will enter the system so in effect the charge density or pseudo-spin density at the edge has changed by one unit. Note that the only type of charge needed to be conjugated is the vorticity charge not the real electric charge because there is no restrictions on the electric field distribution at the edge. The same type of processes can occur for other types of merons. These processes will dissipate the edge current and depending on the type of process the dissipation in drag and drive layer will be different. Consider the edge that absorbs vortices and emits anti-vortices, and assume the interlayer bias is toward the top layer. In this case the most energetically favorable process is $V^- \uparrow \rightarrow A^+ \uparrow$ in which the total charge at the edge changes by one electronic charge. This charge will be added only to the upper layer to minimize the exchange interaction energy with the existing pseudo-spin up electrons. The rate of this process can be formulated as $g_{n\uparrow}n_\uparrow - g_{p\uparrow}p_\uparrow$ which includes the reverse process and the g's are the coupling constants indicating the strength of the process. The next lowest energy process is $V^- \uparrow \rightarrow A^- \downarrow$. This process doesn't change the total charge density of the edge but increases the pseudo-spin density of the edge electrons by trying to rotate their pseudo-spins toward the upper layer reducing the charge density in the bottom layer. The rate for this process can be written as $h_{n\uparrow}n_\uparrow - h_{n\downarrow}n_\downarrow$. The next process is $V\downarrow^+ \rightarrow A\uparrow^+$: again this will not change the total charge density of the edge but tries to rotate the pseudo-spin of the edge electrons toward bottom layer reducing the charge density of the upper layer. The rate of this process is : $h_{p\downarrow}p_\downarrow - h_{p\uparrow}p_\uparrow$. The last and least favorable process is $V\downarrow^+ \rightarrow A\downarrow$ in which the total charge of the edge reduces by one electronic charge but the pseudo-spin of edge is not affected. The rate of this process is $g_{p\downarrow}p_\downarrow - g_{p\downarrow}p_\downarrow$. The above discussion implies $g_{n\uparrow}, g_{p\uparrow} \gg h_{n\uparrow}, h_{n\downarrow} \gg h_{p\downarrow}, h_{p\uparrow}, g_{p\downarrow}, g_{n\downarrow}$. Assuming the edge current flows only in one edge channel with constant velocity v_E the evolution of the edge charge density for each layer will be as follows :

$$\frac{d\rho_\uparrow}{dt} = v_E \frac{\partial \rho_\uparrow}{\partial x} + (g_{n\uparrow}n_\uparrow - g_{p\uparrow}p_\uparrow) +$$

$$
\begin{aligned}
&- \quad (h_{p\downarrow}p_\downarrow - h_{p\uparrow}p_\uparrow) - (g_{p\downarrow}p_\downarrow - g_{n\downarrow}n_\downarrow) \\
\frac{d\rho_\downarrow}{dt} &= v_E\frac{\partial\rho_\downarrow}{\partial x} + (h_{p\downarrow}p_\downarrow - h_{p\uparrow}p_\uparrow) + \\
&- \quad (h_{n\uparrow}n_\uparrow - h_{n\downarrow}n_\downarrow). \qquad (4.38)
\end{aligned}
$$

In the absence of tunneling the meron dipole moment can not flip which along with the charge conservation allows us to conclude that the number of each meron type is constant in the steady state. Using this boundary condition we can then find the density gradient of the edge of each layer in terms of the g's and h's in the steady state. Besides the zero bias energy, the activation energy Δ includes the dipole-bias interaction contribution $\tilde{\Delta}(V) \propto V$ for small biases: $\Delta = \Delta_0 + \tilde{\Delta}(V)$. Because the first process has the largest matrix element we can approximately ignore the other processes. Also we can assume the coupling for exchange of $V^- \uparrow$ and $A^+ \uparrow$ merons at the edge are nearly equal: $g_{n\uparrow} \sim g_{p\uparrow}$. With these assumptions, for the drive layer one can get:

$$\frac{d\rho_\uparrow}{dx} = \frac{g_{n\uparrow}e^{\tilde{\Delta}/k_BT}(\mu_{n\uparrow} + \mu_{p\uparrow})}{2e^{\Delta_0/k_BT}g_{n\uparrow} + \Gamma_0 e^{\tilde{\Delta}/k_BT}}I_{CF} \qquad (4.39)$$

In the above μ's are the zero temperature mobilities. In the zero temperature limit we will have $\delta\rho_\uparrow \sim \frac{1}{2}I_{CF}e^{-(\Delta_0-\tilde{\Delta})/k_BT}$ for all positive and negative values of interlayer bias which means the activation energy of the drive layer is behaving asymmetric with respect to V. At this level of approximation no voltage drop can be seen for the drag layer. To the lowest non-zero approximation the charge density gradient for the edge of drag layer will be:

$$\frac{d\rho_\downarrow}{dx} = -\frac{e^{\tilde{\Delta}/k_BT}((\mu_{n\uparrow} - \mu_{p\uparrow})h_{n\uparrow} + (\mu_{n\downarrow} - \mu_{p\downarrow})h_{n\downarrow})}{h_{n\uparrow}e^{\Delta_0/k_BT} + h_{n\downarrow}e^{\frac{2\tilde{\Delta}+\Delta_0}{k_BT}} + \Gamma_0 e^{\tilde{\Delta}/k_BT}}I_{CF}. \qquad (4.40)$$

for which at zero temperature limit we see that

$$\delta\rho_\downarrow \sim -e^{-(\Delta_0+\tilde{\Delta})/k_BT}[(\mu_{n\uparrow} - \mu_{p\uparrow})h_{n\uparrow}/h_{n_\downarrow} + (\mu_{n\downarrow} - \mu_{p\downarrow})]I_{CF} \qquad (4.41)$$

for $V > 0$ and

$$\delta\rho_\downarrow \sim -e^{-(\Delta_0-\tilde{\Delta})/k_BT}[(\mu_{n\uparrow} - \mu_{p\uparrow}) + (\mu_{n\downarrow} - \mu_{p\downarrow})h_{n\downarrow}/h_{n_\uparrow}]I_{CF} \qquad (4.42)$$

for $V < 0$. This is showing a symmetric activation energy with respect to V.

Of course ultimately the above two pictures (Chern-Simon theory and meron-edge interaction theory) must be united. The Chern-Simon theory neglects edges entirely and only assumes a balanced meron population. However this can only be true for a finite system if we allow for charge conversion as given in figure (4.16). Conversely, the edge picture does not predict the mobilities and transition rates implicit in eq.(4.38). These must be generated by a microscopic theory such as the Chern-Simon approach.

Chapter 5

Nanoring Arrays

Traditional solid state physics deals with systems of macroscopic size. Using a combination of statistical mechanics and quantum mechanics physicists have been able to understand many physical aspects of different types of materials. These materials consist of a macroscopic number of particles of the order of Avogadro's number N and volume V. In order to be able to use statistics in calculations one needs to assume N and V approach infinity in a way that the density $n = N/V$ stays constant. Quantum interference effects in these systems usually are suppressed due to the large number of particles except at special circumstances like in superfluid systems at low temperatures or most of the second order magnetic phase transitions. However fabrication of micro- and nano-sized structures like quantum dots, wires and rings in recent years[3] has made it possible for physicists to examine new ideas in the physics of electronic devices. In these systems two important interrelated quantum mechanical characteristics can change the behavior from being a regular macroscopic system: discreteness of energy levels and interference. These small size devices act as artificial atoms with discrete spectra and shell structure similar to those of real atoms. It is also possible to control the properties of these synthetic atoms in a way that is impossible with real ones. For example, a regular atomic orbital is three dimensional and one has limited control over the electronic wave function, while in contrast by controlling the shape of a quantum dot we can distort the wave function, controlling its polarizability and its interaction with adjacent dots.

When the number of particles in a quantum system is small one can expect to observe quantum interference effects. However even in very dilute systems quantum phase coherence can be destroyed by inelastic scattering events. In very small systems on the other hand, the confined particle's path can be short enough to reduce the

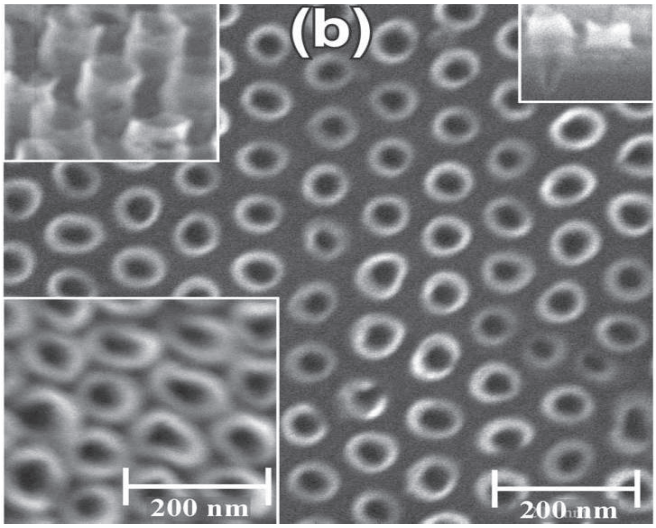

Figure 5.1: SEM Images of Ni Nano-Rings a patterned perpendicular recording media. Fabricated using bottom-up Alumina Templates with top-down fabrication techniques. Courtesy of Prof. Johnson's Lab, Department of Physics, University of Oklahoma.

number of inelastic scattering. In the next section I will explain how inelastic scattering can destroy the quantum mechanical phase of a particle and show that if the size of the systems is smaller than or of the order of a characteristic length L_ϕ called *phase breaking length* then one can expect quantum interference effects to appear in the measured properties.

The focus here is on the periodic arrays of nano-rings. The basic difference between the ring geometry and a quantum dot is the excluded middle(Fig.5.1) which confines the electron in a ring to a narrow spatially periodic channel. This system is capable of exhibiting various interesting phenomena such as a *persistent current*[4; 5; 6; 7] and *electrostatic polarization*[8] due to quantum mechanical phase coherence. We should emphasize that the model used here is very simple and does not include many different structural details of the rings. This idea of electrostatic polarization of interacting ring arrays is a new idea and it is intended to open up a new field investigation on collective phenomena in nanostructures.

5.1 Phase Coherence

As mentioned in the introduction the main feature of small size devices is the absence of scatterings that destroy the quantum mechanical phase and consequently

any possible interference effects. This is a very important feature in nanostructures like interacting quantum rings. In these systems the particles behave quantum mechanically and one needs to take the uncertainty principle and interference effects into account in analysis. These systems usually are coupled to a much larger system called the environment. The environment can be a lattice, surrounding electron gas or the measurement probes. If in the scattering event the state of the environment changes then a measurement has happened. These types of scattering events are called *inelastic*. In this case the coupling of the particle with the environment involves this change of state in the total state of the particle+system and causes the interference terms to vanish. As an example let's consider the Aharanov-Bohm experiment in a quantum ring as figure (5.2) is demonstrating. In this setup an electron is expected to have the option of traveling either right or left arm of the ring. The ring is threaded by a magnetic flux Φ. In case of no interaction with the environment the wave function of the electron at time t is:

$$\psi = \psi_l(t) + \psi_r(t) \tag{5.1}$$

in which ψ_l and ψ_r are the probability amplitudes of the electron taking the left and right arms respectively. The probability distribution then will have an interference term $2Re[\psi_l^* \psi_r]$ and this term will have the Aharanov-Bohm phase $\phi_{AB} = e\Phi/\hbar$ as it is the real part of the probability amplitude of the electron traveling once around the ring.

Now when a measurement event takes place or there is an interaction with the environment the wavefunction will not be the same as before. Let's say $\chi_l(\eta)$ and $\chi_r(\eta)$ are the wavefunctions of the environment for the left and right arms respectively. η is a coordinate of the environment. The wavefunction of the electron+environemt system will then be:

$$\psi = \psi_l \otimes \chi_l(\eta) + \psi_r \otimes \chi_r(\eta) \tag{5.2}$$

After time t the interference term would be :

$$2Re[\psi_l(t)^* \psi_r(t) \int d\eta \chi_l^*(\eta, t) \chi_r(\eta, t)] \tag{5.3}$$

The integral over η is because the state of the environment is not being measured at any time during the electron travel so we have to sum over all η's. This is nothing but the scalar product of two states of the environment. These two states are the same at $t = 0$ but at time t the interaction has happened and they are different. When these two states are orthogonal to each other then the state of the electron has been identified and the interference term is zero, the states can be distinguished.

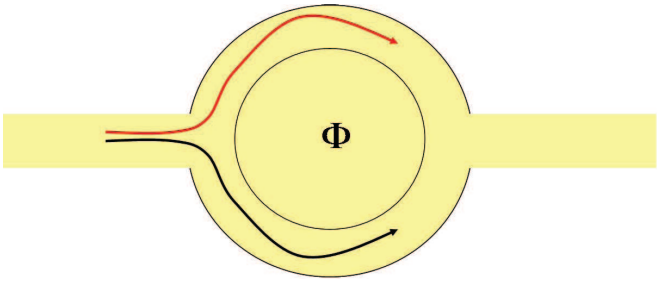

Figure 5.2: Schematic picture of the possible electron path through a semi-circular circuit threaded by a magnetic flux.

The *dephasing rate*, $1/\tau_\phi$ is defined as the frequency of this type of event which is the shift of the environment state to another orthogonal state. The *dephasing length*, L_ϕ is defined as the average length at which the particle travels without changing the state of the environment to an orthogonal one.

5.2 Model of Interacting Rings

We consider a one dimensional array of singly charged narrow quantum rings with radius R and center-to-center separation of D (Fig.5.2). The width of each ring is much smaller than its inner radius so that the lateral confinement energy of the electron is high enough that we need only consider the one dimensional movement of the electron around the ring. The rings are isolated from each other so there is no charge transfer between rings however we consider the Coulomb interaction between nearest neighbors to be in effect. The Coulomb interaction scales inversely with distance, whereas the tunneling is exponentially suppressed. Indeed it would be experimentally difficult to achieve the limit where electrons *can* tunnel between rings. In the limit where electrons can tunnel from ring to ring the dynamics are much richer. While in principle the Coulomb interaction is long range, we assume that there is sufficient screening that next nearest neighbor interactions can be neglected. All the phenomena explained here only will show up in real experiments if the rings are sufficiently narrow, $\frac{\hbar}{2m^* w^2} \gg k_B T$ in which w is the width of the ring, so that electrons are effectively one dimensional. On the other hand as we mentioned before it is very important that electrons do not lose their quantum mechanical phase, i.e. the ring's perimeter has to be smaller than the electron's coherence length ($2\pi R < L_\phi$) and the temperature has to be lower than the dephasing temperature ($T < T_\phi$). Only in this conditions we can treat electrons as particles in a *periodic* one dimensional potential

even in presence of disorder. With these assumptions one can solve for the extended state solutions for the wave function of the electron. Major sources of dephasing are usually electron-phonon interaction and impurity of the system whose effects will be highly reduced in today's fabricated nano-rings .

In each ring the confinement energy of the electron scales as $E_q = \hbar^2/2m^*R^2$; this energy opposes localization of the wavefunction in the ring. The inter-ring Coulomb repulsion, which scales as $E_c = e^2/D$, tries to localize the wavefunction. Electrons are repelled from regions of the ring where it is too close to the charges on neighboring rings. The competition between these two physical scales creates a *quantum phase transition* in the array from a localized state to extended state.

5.3 Classical Charges

Before solving a quantum mechanical problem it is always helpful to look at the similar classical case which is usually easier to solve. The classical model considers one charged point particle per ring with only nearest neighbor Coulomb interaction. Unlike the quantum mechanical case there is only one energy scale in the classical problem which is the Coulomb energy $E_c = e^2/D$. The energy of a 1D array is given by $U_{1D} = \sum_{i=1}^{N} e^2/|\vec{r}_i(\theta_i) - \vec{r}_{i+1}(\theta_{i+1})|$, where θ_i is the location of the i-th electron as measured from horizontal axis. In the dipole approximation we can write this as :

$$\begin{aligned} U_{1D} - U_0 &\approx \frac{\epsilon^2 e^2}{2D} \sum_i [3\cos 2\theta_i + \cos(\theta_i - \theta_{i+1}) \\ &- 3\cos(\theta_i + \theta_{i+1})] \\ &= \frac{\epsilon^2 e^2}{D} \sum_i [\vec{s}_i \cdot \vec{s}_{i+1} + \frac{3}{2}(\hat{D} \cdot (\vec{s}_i - \vec{s}_{i+1}))^2]. \end{aligned} \tag{5.4}$$

where $\epsilon \equiv R/D$ and U_0 is a constant, $U_0 \equiv \frac{Ne^2}{D}(1 + \frac{\epsilon^2}{2})$. In the second expression we identify the position of each charge by a vector $\vec{s}_i$ in the 2D plane of the ring pointing from the center of the i-th ring to the charge on that ring. The unit vector $\hat{D}$ lies on the horizontal axis (see figure 5.3).

The $\cos 2\theta$ (or $(\hat{D} \cdot \vec{s})^2$) term explicitly breaks the rotational symmetry, driving the system from XY to Ising-like behavior. The Heisenberg term in the last line of equation (5.4) drives the system ferroelectric at zero temperature while the second and larger term favors states where neighbors point in opposite direction. Thus the system at zero temperature orders in an antiferroelectric (AFE) pattern (Fig.5.2)

in one dimension. Our numerical Monte Carlo simulations of the exact Coulomb interaction also verifies the existence of such a minimum energy configuration in the classical finite size arrays.

We can examine the stability of the AFE state by finding the higher energy modes of the system. We expand the energy function (5.4) to quadratic order in displacement angle around the AFE configuration using $\theta_i = (-1)^i \frac{\pi}{2} + \alpha_i$. The AFE configuration has a basis with two sites so we find two independent normal modes with frequencies:

$$\omega_{\pm}^{(1D)}(k) = 2\omega_0 \sqrt{4 \pm 2\cos\frac{kD}{2}}. \tag{5.5}$$

Where $\omega_0 \equiv \sqrt{e^2/m^* D^3}$. Both the modes are gapped since the Ising-like term provides the harmonic restoring force at each site. The modes are shown in Fig.(5.2). The normal modes are found to be independent of the ring radius.

Another interesting classical limit of our ring problem is when there is a classical *self-interacting* fluid of charge on each ring while the nearest neighbor fluids are still interacting with each other. A quantum mechanical wave function for a particle behaves to some extent like such a fluid although a wave function does not have self-interaction.

To find the minmum energy distribution of charge density on each ring we define an angular dependent charge density $\rho_i(\theta_i)$ on each ring where: $\int \rho_i(\theta_i) d\theta_i = 1$. We are looking for the minimal solution to the variational quantity :

$$I = \frac{1}{2} \int d\theta \int d\theta' \sum_{\langle ij \rangle} \frac{\rho_i(\theta)\rho_j(\theta')}{|\vec{r}_i - \vec{r}_j|} + \lambda \sum_i \int d\theta \rho_i(\theta). \tag{5.6}$$

For a 1D ring this expression is divergent due to infinite self energy. We can regularize this in several ways. One method is to introduce a short distance cutoff ζ to the Coulomb interaction, discretize the integral equation and then solve the problem numerically. An approximate analytic solution can then be obtained by Fourier expanding the distribution, keeping only the first three modes. For 1D array with periodic boundary condition we find that the amplitude of the non-trivial Fourier mode as a function of ζ and $\epsilon \equiv R/D$ for ρ is given by:

$$\hat{\rho}^{(2)} \approx \frac{-3\pi\epsilon^3(2 - 5\zeta^2)}{4(-2 + 4\log(\epsilon/\zeta))}. \tag{5.7}$$

We compare this analytic result with the numerical digitalization of (5.6) in Fig.(5.5). As we can see in Fig.(5.5) the minimum energy configuration of the 1D array of charge fluid does not break the up-down symmetry of the system.

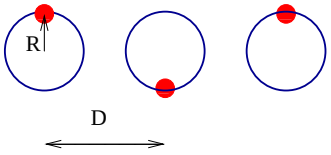

Figure 5.3: A schematic picture of the groundstate of classical point electrons for 1D array of rings. The ring radius is R and the separation is D. The 1D ordering is antiferroelectric and thus has a double degenerate groundstate.

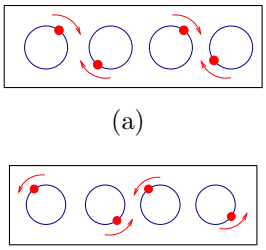

(a)

(b)

Figure 5.4: Normal modes of the 1D ring array with gaps of (a) $2\sqrt{2}\omega_0$ and (b) $2\sqrt{6}\omega_0$.

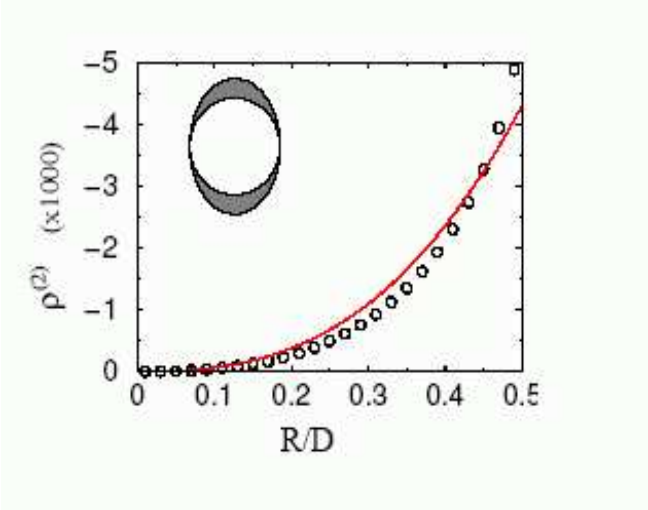

Figure 5.5: A plot of the second fourier amplitude of the classical charge distribution on a ring in a 1D horizontal array. The circles are numerical results, the solid line is a scaled plot of eq.(5.7). Scaling is required since the analytic result neglects all higher fourier modes. Inset: a sketch of the charge distribution that corresponds to this Fourier mode. Note that the symmetry of the array is not broken by the charge distribution.

5.4 Quantum Charges

At first glance the quantum mechanical wave function of a charged particle resembles the classical charge fluid. Although the wave function does not have self-interaction, the quantum particle has a kinetic energy which opposes localization, making the analogy to charge fluid even stronger. Unlike the classical case, the quantum problem has two competing energy scales: the quantum kinetic energy, E_q, preventing localization and the Coulomb interaction energy, E_c, trying to localize the charges away from each other. At $E_q \ll E_c$ we expect charge localization on each ring and at $E_q \gg E_c$ we expect no localization of charge, however it is not *a priori* obvious whether the charge localization pattern (system polarization) breaks the symmetry or not, exactly when this transition happens and the exact nature of this transition.

As a first step we can use a simple variational wave function to find the polarization behavior of the system in ground state. The dimensionless Hamiltonian of an array of one dimensional rings with radius R is given by:

$$\hat{H} = -\sum_i \frac{\partial^2}{\partial\theta_i^2} + \delta \sum_{\langle ij \rangle} \frac{1}{|\vec{r}_i(\theta_i) - \vec{r}_j(\theta_j)|}, \tag{5.8}$$

where $\delta = E_c/E_q$ is the interaction strength and the energy is measured in units of $E_q = \hbar^2/2mR^2$. To find the ground state energy of the 1D array we employ a simple ansatz for the wavefunction of each sublattice :

$$\begin{aligned} \psi_A(\theta) &= \frac{\sqrt{1-y^2}}{\sqrt{2}\pi} + \frac{y}{\sqrt{2\pi}}\cos(\theta - \phi) \\ \psi_B(\theta) &= \frac{\sqrt{1-y^2}}{\sqrt{2}\pi} - \frac{y}{\sqrt{2\pi}}\cos(\theta - \phi) \end{aligned} \tag{5.9}$$

The ground state values of y and ϕ is obtained by minimizing the energy (5.8) using dipole approximation for Coulomb interaction we find:

$$y(\delta, \epsilon) = \begin{cases} \frac{1}{4}\sqrt{11 - \frac{4}{\delta\epsilon^2}} & \text{for } \delta \geq \delta_c(\epsilon) \\ 0 & \delta < \delta_c(\epsilon) \end{cases} \tag{5.10}$$

and $\phi = \pi/2$, where the critical value of the interaction is given by $\delta_c(\epsilon) = \frac{4}{11}\epsilon^{-2}$. To find out the degree of polarization we define the *staggered polarization* vector as:

$$\vec{P}_s = \sum_i (-1)^i \int |\psi_i(\theta)|^2 \vec{r}_i(\theta) d\theta. \tag{5.11}$$

Using variational results the staggered polarization of the system is as follows:

$$\vec{P}_s(\delta,\epsilon) = \begin{cases} \frac{1}{8}(\frac{4+5\,\delta\epsilon^2}{2\delta\epsilon^2})^{\frac{1}{2}}(11-\frac{4}{\delta\epsilon^2})^{\frac{1}{2}}\hat{D}_\perp & \delta \geq \delta_c \\ 0 & \delta \leq \delta_c \end{cases} . \tag{5.12}$$

Where $\hat{D}_\perp$ is the unit vector perpendicular to the common axis of the rings and δ_c is defined in equation (5.10). A plot of this function is shown in figure 5.6 (see the discussion of next section). As we can see variational calculation suggests that the ground state of the 1D array of rings antiferroelecrically polarizes in perpendicular direction at high interaction strengthes while at lower values the wave functions are not localized, hence the system has no polarization. The validity of this result will be confirmed in next sections using more exact and reliable methods of calculation.

5.5 Hartree Approximation

The rings considered here are well separated with exactly one electron on each ring. Under this condition and because of strong Coulomb repulsion the effect of inter-ring transfer of electrons and overlap of wave functions is small. We can therefore neglect the inter-ring transfer from our calculations. Since without overlap the electrons do not have any exchange interaction, the Hartree approximation is exact for this problem. We can decompose the wave function in each ring into a limited number of Fourier modes:

$$\psi_i(\theta) = \sum_{n=-n_0}^{n_0} c_n e^{in\theta} \tag{5.13}$$

and then solve the system numerically in the Hartree approximation. We impose the periodic boundary conditions on the array and by an iterative self-consistent method we find the ground state wave function of the rings. In Fig.(5.6) we can see the numerical results of the polarization and energy change of the 1D array of rings for different number of Fourier modes using exact Coulomb interaction and also its agreement with the variational calculation when we restrict the number of Fourier modes to $n \in \{-1, 0, 1\}$. The results are little changed when we increase the number of Fourier modes mostly in the high coupling regime. All the above results suggest that there is transition from unpolarized to polarized state at zero temperature by changing the coupling. By looking at the behavior of polarization when the number of Fourier modes increases we realize that this transition tends to be sharper and sharper for higher number of Fourier modes suggesting a true phase transition in the system.If true, this transition would be a sudden change of ground state of the

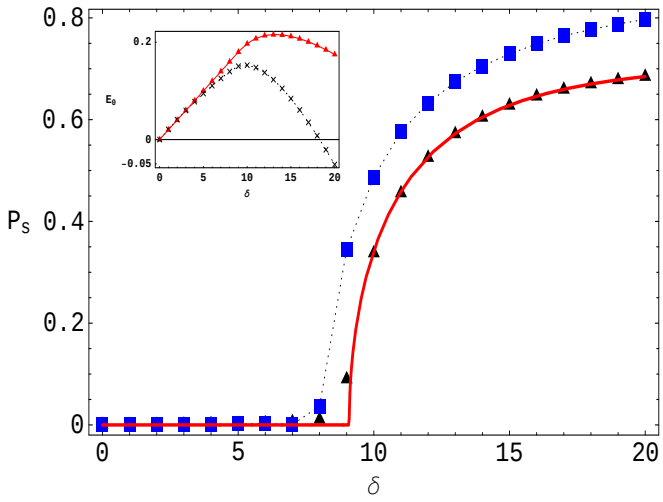

Figure 5.6: A comparison of numerical and analytical calculations of the staggered polarization and energy as a function of δ in a 1D quantum ring array obtained in the Hartree approximation. The numerical results are for the case include Fourier modes $|m| \leq 1$ (triangles) and $|m| \leq 6$ (boxes). The solid line is the analytic result assuming $|m| \leq 1$. The quantity δ is a measure of the competition between the Coulomb interaction and the quantum kinetic energy

quantum system at zero temperature, known as *quantum phase transition*.[11] We will find out if this phenomena happens and find out the universality class of the transition in the next section using the Monte Carlo simulation.

5.6 Monte Carlo simulation

It is well-known[11] that we can write the quantum partition function of a quantum system, $Z = Tre^{-\beta\hat{H}}$ as the sum over all paths taken by the system in an imaginary time defined by the scale $\hbar\beta$. If the quantum system is D-dimensional then the partition function will look like the path integral of a D+1-dimensional classical system in which the extra dimension is the time direction $0 < \tau < \beta\hbar$. At zero temperature $\beta \to \infty$ the classical system is truly D+1-dimensional. One can derive an effective Hamiltonian for such a classical system from the quantum Hamiltonian using a complete basis states. In this classical system the parameter of the quantum system (in our case δ) is a control knob like temperature.

We can use Monte Carlo simulation of such a classical system to find out the universal behavior of the quantum system. To develop a 1+1-dimensional classical

theory for our 1D ring array we first stagger the order parameter,$\theta_i \to (-1)^i\theta_i$ so that we can analyze the Monte Carlo results easily. We also use dipole approximation for the Coulomb interaction. Consequently we can write the Hamiltonian of the system as:

$$\hat{\mathcal{H}} = \frac{E_c}{2}\sum_{j=1}^{N}(-i\frac{\partial}{\partial\theta_j})^2 - E_J\sum_{j=1}^{N}\hat{V}. \tag{5.14}$$

In which $E_c = \hbar^2/mR^2$ and $E_J = e^2\epsilon^2/2D$. In a standard derivation[12] of the classical field theory one start with expanding the partition function by defining a time parameter $T = \beta\hbar$ and dividing it to $\mathcal{N}$ sections, $T = \mathcal{N}\delta\tau$

$$\begin{aligned} Z &= \sum_{\{\theta\}}\langle\{\theta\}|e^{-\mathcal{N}\delta\tau\hat{H}/\hbar}|\{\theta\}\rangle = \\ &= \sum_{\{\theta^{(1)}\}}\cdots\sum_{\{\theta^{(\mathcal{N})}\}}\langle\{\theta^{(1)}\}|e^{-\delta\tau\hat{H}/\hbar}|\{\theta^{(2)}\}\rangle\langle\{\theta^{(2)}\}|e^{-\delta\tau\hat{H}/\hbar}\cdot.. \end{aligned} \tag{5.15}$$

in which $|\{\theta\}\rangle = |\theta_1, \theta_2, ..., \theta_N\rangle$ and we used the fact that $1 = \sum_{\{\theta^{(a)}\}}|\{\theta^{(a)}\}\rangle\langle\{\theta^{(a)}\}|$ for all sets $a = 1, ..., \mathcal{N}$. We can approximate the exponential for $\mathcal{N} \to \infty$

$$e^{-\delta\tau\hat{H}/\hbar} \approx e^{-\delta\tau\hat{K}/\hbar}e^{-\delta\tau\hat{V}/\hbar} \tag{5.16}$$

in which $\hat{K}$ and $\hat{V}$ are the kinetic and potential energy of the Hamiltonian(5.14). We can use the eigenstates of the kinetic Hamiltonian $|m\rangle$ to find

$$\begin{aligned} \langle\{\theta(\tau_a)\}|e^{-\delta\tau\hat{H}/\hbar}|\{\theta(\tau_{a+1})\}\rangle &= \sum_{\{m\}}\langle\{\theta(\tau_a)\}|e^{-\delta\tau\hat{K}/\hbar}|\{m\}\rangle \times \\ &\times \langle\{m\}|e^{-\delta\tau\hat{V}/\hbar}|\{\theta(\tau_{a+1})\}\rangle. \end{aligned} \tag{5.17}$$

where we have parametrized the sets with $\tau_1, ..., \tau_{\mathcal{N}}$. Using $\langle\theta|m\rangle = e^{im\theta}$ for the above matrix element we find

$$\begin{aligned} &= \sum_{\{m\}}\exp\Big\{-(\delta\tau/2\hbar)E_C\sum_k m_k^2 e^{im_k[\theta_k(\tau_{a+1})-\theta_k(\tau_k)]} \times \\ &\times \ e^{+(\delta\tau/\hbar)E_J}\sum_k\cos[\theta_k(\tau_{a+1}) - \theta_k(\tau_a)]\Big\} \end{aligned} \tag{5.18}$$

Because $\delta\tau$ is small, the sum over the m is slowly convergent. We may remedy this by using the Poisson summation formula

$$\sum_m e^{-(\delta\tau/2\hbar)E_C m^2}e^{im\theta} = \sqrt{\frac{\pi\hbar}{\delta\tau E_C}}\sum_n e^{-(\hbar/2E_C\delta\tau)(\theta+2\pi n)^2}. \tag{5.19}$$

This periodic sequence of very narrow Gaussians is (up to an irrelevant constant prefactor) the Villain approximation[13] to

$$e^{+(\hbar/E_C\delta\tau)cos(\theta)}. \tag{5.20}$$

Strictly speaking, we should keep $\delta\tau$ infinitesimal. However, we may set it equal to the natural ultraviolet cutoff, the inverse of the $\delta\tau = \hbar/\sqrt{E_C E_J}$,without changing the universality class. This frequency is actually the frequency of a classical rotating particle in the ring that is under the influence of Coulomb force e^2/D. Substituting this result into Eq.(5.18) yields

$$\begin{aligned} Z &\propto \int \mathcal{D}\theta(\tau) \prod_{a=1}^{\mathcal{N}} \exp\Big\{ \frac{\hbar}{E_c \delta\tau} \sum_{k=1}^{N} \cos[\theta_k(\tau_{a+1}) - \theta_k(\tau_a)] \\ &+ \frac{\delta\tau E_J}{\hbar} \sum_{k=1}^{N} V_k(\tau_a) \Big\} . \end{aligned} \tag{5.21}$$

Where $\mathcal{D}(\theta) \equiv \prod_{a=1}^{\mathcal{N}} D\theta(\tau_a)$ and

$$\begin{aligned} V_k(\tau_a) &= 3\cos[\theta_k(\tau_a) - \theta_{k+1}(\tau_a)] + \cos[\theta_k(\tau_a) + \theta_{k+1}(\tau_a)] \\ &- 3\cos[\theta_k(\tau_a) - \theta_{k+1}(\tau_a)] \cos[\theta_k(\tau_a) + \theta_{k+1}(\tau_a)]. \end{aligned} \tag{5.22}$$

Because of the trace in the partition function the starting and final states are the same so $\theta(\tau + \beta\hbar) = \theta(\tau)$. We will also assume periodic boundary conditions in space direction all over the simulation. By defining the spin vector $\vec{S}_i = (\cos\theta_i, \sin\theta_i)$ we can interpret Eq.(5.21) as a two dimensional classical spin model. Our early calculations suggested that the system of 1D rings has a transition from the unpolarized to the AFE state. In this classical analogue because we have already staggered the order parameter we expect to see a transition from an unpolarized to a ferromagnetically polarized state (FE). Close to this transition the spatial variation of the order parameter $\vec{S}$ is smooth so we can approximate (5.22) as follows:

$$V_k(\tau_a) \approx 3\cos(\theta_k(\tau_a) - \theta_{k+1}(\tau_a)) - 2\cos 2\theta_k(\tau_a). \tag{5.23}$$

Using the above potential finally the classical partition function looks like:

$$Z \propto \int \mathcal{D}\theta(\tau) \exp\Big\{ K \sum_{\langle ij \rangle} \cos(\theta_i - \theta_j) - \frac{2K}{3} \sum_i \cos 2\theta_i \Big\}. \tag{5.24}$$

Where i and j run over an infinite 2D square lattice and we have determined $\delta\tau$ to identify the two couplings in eq.(5.21) as $K = \sqrt{\frac{3E_J}{E_c}}$. Equation (5.24) is a 2D XY

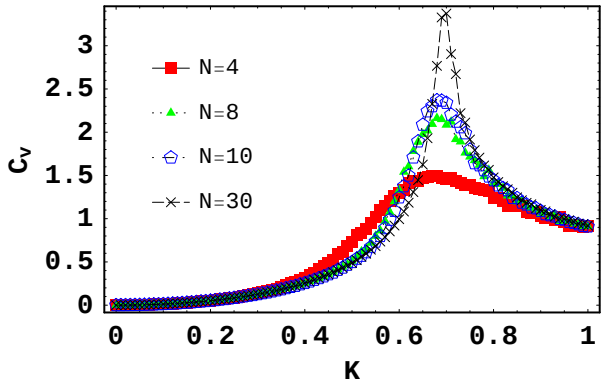

Figure 5.7: Monte Carlo results of the $C_v = \overline{\Delta E}^2$ for different system sizes. The system is a 1+1D classical equivalent of 1D quantum ring array at zero temperature.

model with a symmetry breaking field which is 2/3 the XY coupling. Our Monte Carlo analysis shows that this model has a continuous second order phase transition. The order parameter of this system is the total magnetization density equivalent to the total staggered polarization of the 1D ring array:

$$\vec{m} \equiv \langle \vec{S} \rangle \longleftrightarrow \vec{P}_s. \tag{5.25}$$

Where the average on the left hand side is the thermodynamic average over the infinite size lattice. The fluctuations in this system are controlled by K which is the analogue of $1/T$ in real classical systems. We can measure the analogue of specific heat of the system using:

$$C_v = \langle E^2 \rangle - \langle E \rangle^2 \tag{5.26}$$

in which $\langle . \rangle$ is the average over an ensemble and E is the total energy of the system. This quantity diverges at the critical point of the infinite system undergoing a continuous phase transition. Fig.(5.7) shows the change of the specific heat of our 1+1D system in terms of the parameter K for different lattice sizes. As we can see at K_c the peak gets sharper and sharper with increasing lattice size L. An extrapolation of the point of the maximum of C_v, $K_c(L)$ to $L^{-1} = 0$ determines the approximate critical point of the infinite lattice(Fig.5.8) . Also an extrapolation of $m(L, K)$ for different values of K in Fig.(5.9) shows that a real continues phase transition happens in the infinite size system. The effective classical system derived here does not fully explain all the physical aspects of the 1D quantum system mainly because of the approximations used to derive the path integral. However, we believe that, close to the critical region, these approximations do not play any role in the general behavior

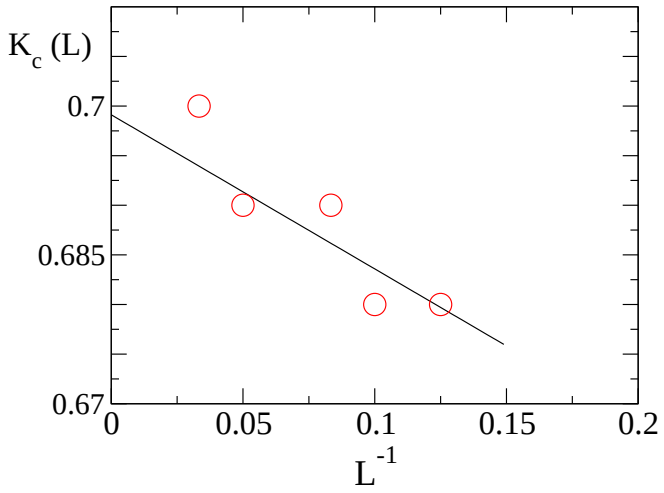

Figure 5.8: Plot of critical coupling $K_c(L)$ at different system sizes taken from the C_v plots.The solid line is a linear fit to the data indicating $K_c(\infty) \approx 0.699$.

of the system and the universality class remains unchanged. Hence using the finite size scaling method we can determine the critical exponents of the classical system and determine the universality class of the actual quantum system.

5.7 Finite size scaling of the 1+1D system

One of the best parameters for examining the phase transition and find the universal exponents with finite size scaling is the dimensionless Binder ratio [9]:

$$g_L = \frac{\langle m^4 \rangle}{\langle m^2 \rangle^2} \tag{5.27}$$

defined for a system with size L. In the disordered phase $K < K_c$ the correlation length ξ is finite so for $L \gg \xi$ the distribution of m is Gaussian around $m = 0$ with the width $\sim N^{-1/2} \sim L^{-d/2}$ so $g_L \to 0$. On the other hand for $K > K_c$ where $\langle m \rangle$ is finite, g_L approaches a constant as $L \to \infty$. The variation of g_L with K becomes sharper and sharper as L increases, however all the g's cross at the transition point K_c. The variation is given by the following finite size scaling function:

$$g_L(K) = \widetilde{g}(L^{1/\nu}(K - K_c)). \tag{5.28}$$

Where $\widetilde{g}$ is a scaling function which depends on L and K only in that particular form.

By using the finite size data we can try to find a data collapse and by calculating the standard deviation find the best exponent ν fitting to the collapsed function. Figure(5.10) shows the Binder ratio for different lattice sizes. For a correct exponent

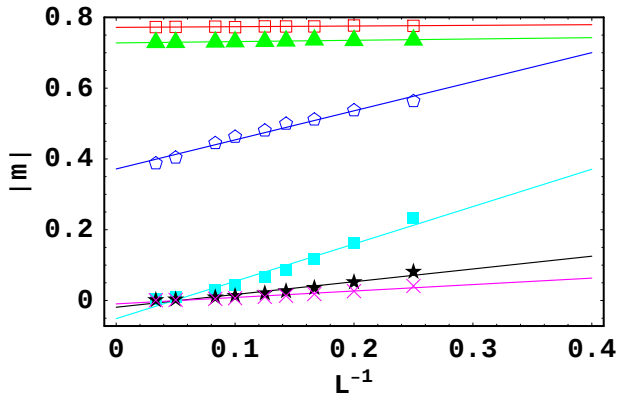

Figure 5.9: Extrapolation of the total magnetization density of the 1+1D classical system to infinite size at couplings $K/K_c(\infty)$=1.45(empty boxes), 1.32(triangles), 1.03(polygons), 0.74(filled boxes), 0.45(stars) and 0.16 (crosses). The solid lines are linear fit to each set of data.

all the scaling functions calculated for different sizes have to be equivalent when plotted against their argument. This can be achieved by minimizing the standard deviation of all curves. When the correct exponent is obtained all the curves will collapse on each other. Figure(5.11) shows the collapsed data and Fig.(5.12) shows the best exponent is $\nu = 1 \pm 0.01$. The scaling for the order parameter $|m|$ is:

$$m = L^{-\beta/\nu} X^0(L^{1/\nu}(K - K_c)). \tag{5.29}$$

Where X^0 is a function of $x = L^{1/\nu}(K - K_c)$ only and β is one of the universal scaling exponents of the system.To determine the universal exponent β we plot $L^{\beta/\nu}$ vs. x for different sizes.Fig.(5.14) and (5.15) show the the collapse of different data sets and the standard deviation for different exponents respectively which shows the best estimation is $\beta = 1/8 \pm 0.005$.

5.8 Universality Class

The universal exponents extracted from the finite size data indicate that our 1+1D classical XY model in the symmetry breaking field is in the universality class of 2D classical Ising model, hence the nature of quantum phase transition of our 1D quantum ring array is Ising. The Coulomb repulsion forces the electrons alternate staying on the top and bottom of the rings. However the quantum kinetic energy tries to avoid localization. This kinetic energy causes the electrons to tunnel from top into bottom of the ring hence destroying the antiferroelectric order. This ordering

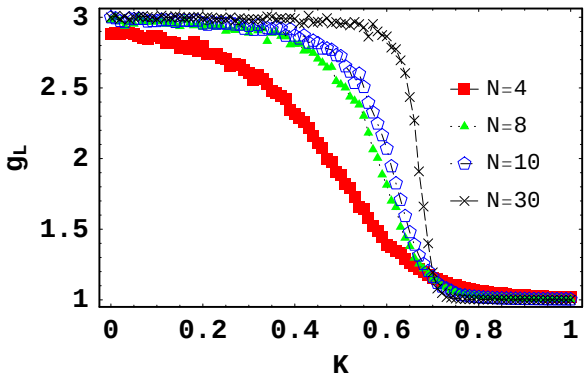

Figure 5.10: Plots of Binder ratio for different system sizes. The behavior is sharper at larger sizes.

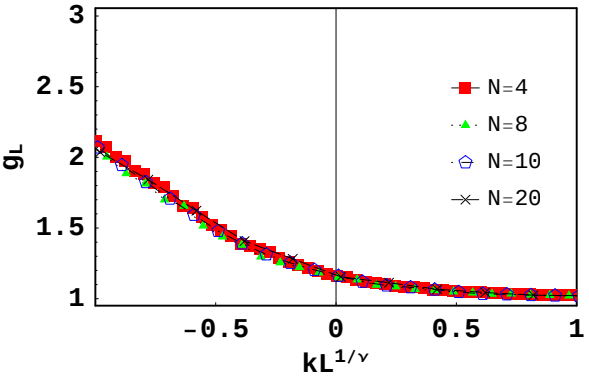

Figure 5.11: Collapse of Binder plots at the critical region.The best collapse is obtained for $\nu = 1 \pm 0.01$.

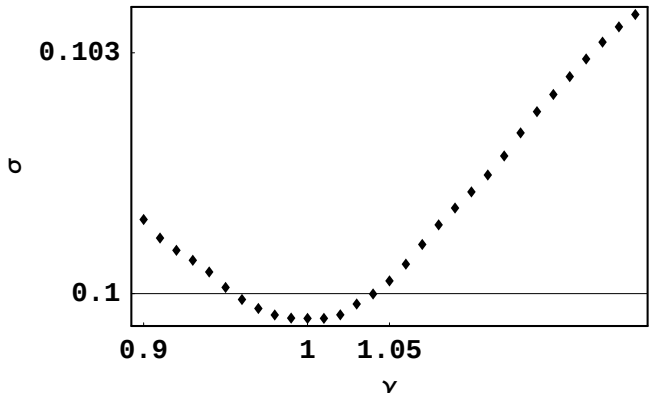

Figure 5.12: Standard deviation of the set of scaled plots of Binder ratio for different exponents.The case for $\nu = 1$ is the best choice which is plotted in Fig.(5.11).

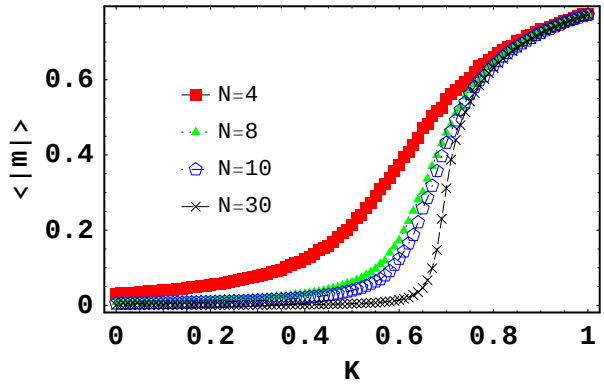

Figure 5.13: Monte Carlo results of average magnetization of the 1+1D classical system for different system sizes. The change of magnetization tends to be sharper as the system size grows.

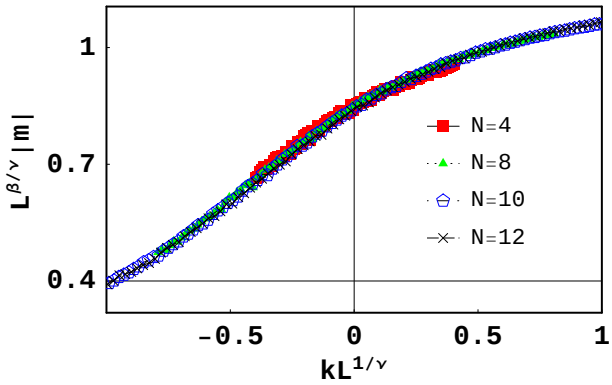

Figure 5.14: Collapse of scaled magnetization data sets for $\nu = 1$ and $\beta = 1/8$ in the critical region.

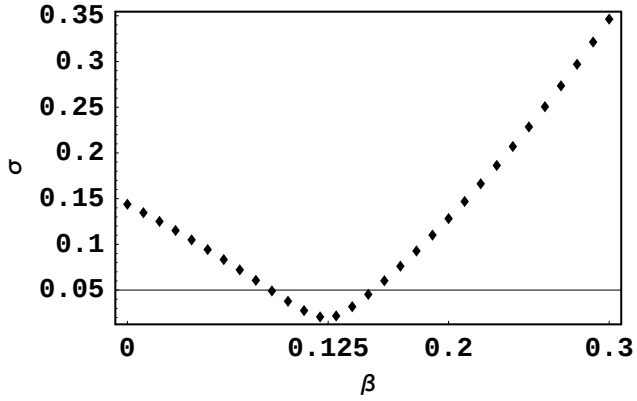

Figure 5.15: Standard deviation of the set of scaled plots of magnetization for fixed $\nu = 1$ and different exponent β. The case for $\beta = 1/8$ is the best choice which is plotted in Fig.(5.14).

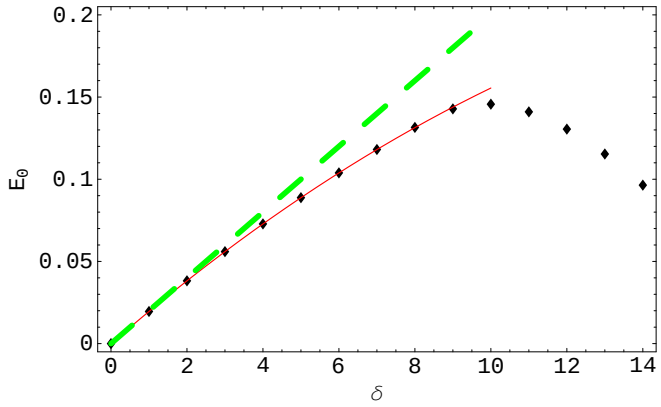

Figure 5.16: Plot of the energy of an interacting quantum ring array when all the wavefunctions are constant around the ring (dashed) or all are in the form of $\psi_d = a+b\cos 2\theta$(solid).The points are the actual results coming out of the numerical Hartree calculation indicating that ψ_d is the selected behavior for $\delta < \delta_c \approx 8$.

behavior shows up in the probability distribution on each ring. Fig.(5.16) shows the energy of each electron with the wavefunction $\psi_d(\theta) = x + y\cos(2\theta)$ compared to when the wavefunction is a constant all around the ring.The wavefunction ψ_d has two maxima on top and bottom of the ring which means the electron is fluctuating up and down. As we can see by increasing the coupling the lower energy state selected by the exact Hartree calculations (dots) gradually matches ψ_d instead of constant wavefunction. This behavior persists in a range of couplings close but smaller than the critical coupling i.e. in disordered region $\delta < \delta_c$. Needless to say that after transition point the ground state wavefunction is no longer ψ_d and the system starts to excite more angular momentum eigenstates (Fourier modes).

All the above discussion suggests that the nature of the antiferroelectric transition is not just the simple 2D Ising but is similar to *1D transverse field Ising*(TFI) which has a quantum phase transition at zero temperature in the same universality class as 2D Ising. We can develop an effective 1D TFI Hamiltonian for our ring array in the dipole approximation. In this approximation we can write down the Hamiltonian(5.14) as follows :

$$\begin{aligned} \hat{H} &= \hat{H}_0 + \hat{V} \\ \hat{H}_0 &= \sum_i [(-i\frac{\partial}{\partial\theta_i})^2 + 3\delta\epsilon^2\cos 2\theta_i] \\ \hat{V} &= -\delta\epsilon^2 \sum_i [3\cos(\theta_i + \theta_{i+1}) + \cos(\theta_i - \theta_{i+1})]. \end{aligned} \tag{5.30}$$

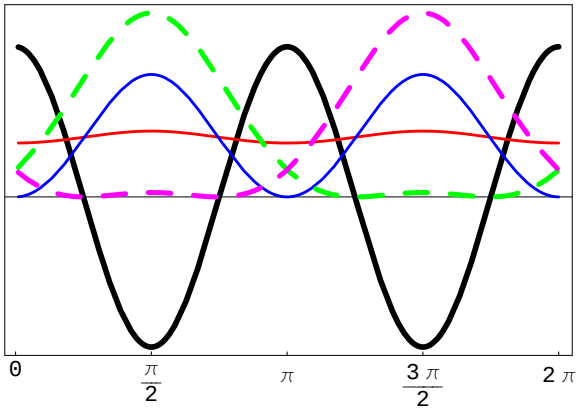

Figure 5.17: Plot of the $\cos 2\theta$ potential around a ring (the thick solid line), the ground and first excited state of this potential (thin solid lines) coming out of a simple numerical Schrodinger equation solver and the up and down states (dashed lines) constructed from the two eigenstates(see appendix).The scale of the potential is exaggerated for easier comparison.

The $\cos 2\theta$ term in the Hamiltonian $\hat{H}_0$ has minima at the top and bottom of the ring.

Fig.(5.17) shows the potential and the two lowest energy states of it with energies $E_0 < E_1$. The rate of tunnelling from top to bottom or vise versa is determined by $\Delta \equiv E_1 - E_0$. The potential $\hat{V}$ tries to align the electrons hence it acts like the Ising interaction. A more rigorous derivation using Holstein-Primakov bosons[8] shows that the projection of the Hamiltonian $\mathcal{H}$ into the subspace of the ground and first excited states of $\hat{H}_0$ can be written as:

$$\hat{H} \approx \Delta \sum_{i=1}^{N} \sigma_i^x - J \sum_{i=1}^{N} \sigma_i^z \sigma_{i+1}^z. \tag{5.31}$$

In which σ's are Pauli spin matrices and $J = 8\delta\epsilon^2$. Numerical diagonalization of $\hat{H}_0$ tells us that $\Delta \approx 1 - 0.1\delta\epsilon^2$ for small ϵ.

Close to transition the Coulomb repulsion is not strong enough to excite the electrons to higher states, consequently the TFI model in Eq.(5.31) is valid and indicated the nature of transition of the 1D ring array.

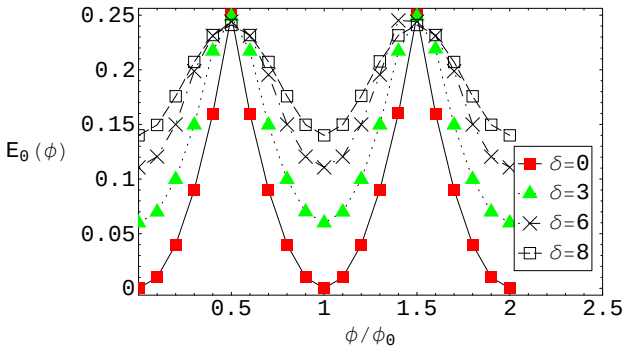

Figure 5.18: Plots of ground state energy of the interacting quantum ring array in the external magnetic flux threading each ring for different couplings δ. The physics is periodic because of Aharanov-Bohm induced phase that is proportional to the flux.

5.9 Effect of Magnetic Flux

Y. Aharanov and D. Bohm (AB) have predicted [10] that the wave function of an electron moving in a vector potential $\vec{A}(x)$ along the path C acquires a phase shift:

$$\Delta\Lambda = \frac{e}{\hbar c}\int_C \vec{A}\cdot\vec{dr}. \tag{5.32}$$

AB predicted that this phase shift can be observable.When an electron is confined on a closed path like the case of charged ring threaded by magnetic flux ϕ the phase shift after one 2π rotation would be :

$$\Delta\Lambda = \frac{e}{\hbar c}\oint \vec{A}\cdot\vec{dr} = \phi/\phi_0. \tag{5.33}$$

Where $\phi_0 = hc/e \simeq 4.135\times10^{-7}G.cm^2$ is the quantum of flux.

The phase shift above has been observed in numerous experiments and different devices including the experiments of persistent current and excitons in quantum rings. In this section we show how magnetic field changes the behavior of polarization.

The kinetic energy of an electron in a ring threaded by a constant uniform magnetic field $B\hat{z}$ (the ring is in the x-y plane) is as follows:

$$\hat{H} = \frac{1}{2m}(\vec{P} - \frac{e}{c}\vec{A})^2. \tag{5.34}$$

For the choice of gauge: $\vec{A} = \frac{B}{2}(-y, x, 0)$ the Hamiltonian (5.34) will look like:

$$\hat{H} = \frac{\hbar^2}{2mR^2}(i\frac{\partial}{\partial\theta} + \frac{\phi}{\phi_0}) \tag{5.35}$$

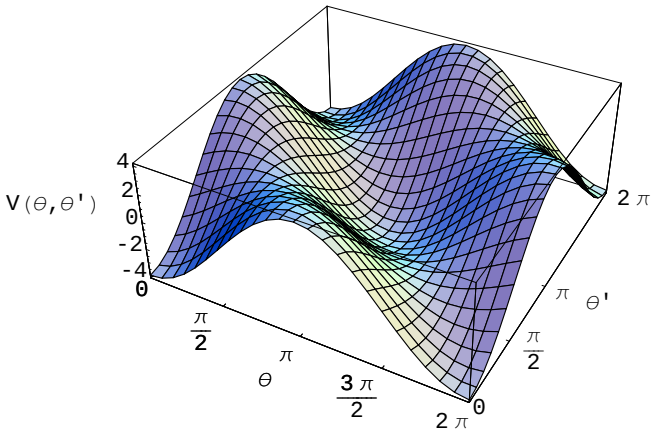

Figure 5.19: Plot of the two-body potential function in Eq.5.40. The interacting rings in magnetic field select the minimum of this potential for their ground state wavefunction at low couplings. The potential is in units of $\delta\epsilon^2$.

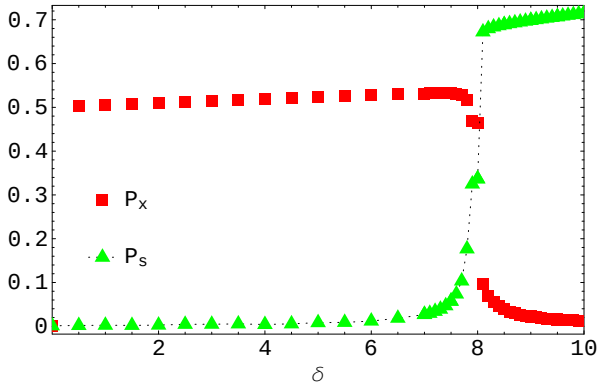

Figure 5.20: Results of numerical Hartree calculations of the polarization of a 1D quantum ring array threaded by half-flux quantum $\phi/\phi_0 = 1/2$.At $\delta < \delta_c$ before staggered polarization (P_s) starts to develop a finite transverse total polarization(P_x) appears in the system.

in which the momentum is in the polar coordinates:$\hat{p} = -i\frac{\hbar}{R}\frac{\partial}{\partial\theta}$ and the eigenfunctions are periodic: $\psi(\theta + 2\pi) = \psi(\theta)$. The eigenenergies of (5.35) will be:

$$E_n = \frac{\hbar^2}{2mR^2}(n - \phi/\phi_0)^2 \tag{5.36}$$

in which n is an integer. By changing the gauge $\vec{A} \rightarrow \vec{A} - \nabla\Lambda$ wavefunctions undergo a phase change $\psi \rightarrow e^{\frac{ie}{\hbar c}\Lambda}\psi$. For example we can use the gauge transformation with the choice of $\Lambda = (BR^2/2)\theta$ to remove the vector potential from (5.35) but at the same time we have to shift the phase of the wavefunctions to $e^{-i\frac{\phi}{\phi_0}\theta}\psi$. As the result the eigenfunctions change:

$$\psi_n(\theta) = \frac{1}{\sqrt{2\pi}}e^{i(n-\phi/\phi_0)\theta}. \tag{5.37}$$

This eigenfunction however has a different boundary condition than the previous one :

$$\psi(\theta + 2\pi) = e^{2\pi i\phi/\phi_0}\psi(\theta) \tag{5.38}$$

but as one physically expects the eigenenergies are not changed.

The ground state energy of the interacting quantum ring array in the magnetic flux ϕ can be written as:

$$\begin{aligned} E_0(\delta,\phi) &= \sum_{n=-n_0}^{n_0} |c_n|^2(n - \phi/\phi_0)^2 + \\ &+ \delta\sum_{\langle ij\rangle}\int d\theta d\theta' \frac{|\Psi_0(\theta)|^2|\Psi_0(\theta')|^2}{|\vec{r}_i(\theta) - \vec{r}_j(\theta')} \end{aligned} \tag{5.39}$$

where $\Psi_0(\theta) = e^{i\phi/\phi_0\theta}\sum_{n=-n_0}^{n_0} c_n e^{in\theta}$ is the ground state wavefunction expanded in the free Hamiltonian basis states.

As we can see in Eq.(5.39) the only part that is affected by the AB phase is the kinetic energy and the potential energy is not sensitive to the phase. When the magnetic flux changes the Eq.(5.39) changes with a period of ϕ_0 because for $\phi/\phi_0 = 1$ we can rearrange the sum and show that the value of the kinetic energy is equal to its value at $\phi = 0$. This is an evidence for the fact that the physics of quantum ring arrays in the presence of magnetic field doesn't change at integer flux quanta. For infinite n_0 this argument is true at any range of magnetic flux however in our numerical calculations where we have used a finite number of Fourier modes E_0 is periodic only at the range $0 < \phi < n_0\phi_0$ in Fig.(5.18) we can see the periodic behavior of the ground state energy of the ring array as magnetic flux changes. The results of our numerical Hartree calculations indicate that in a 1D ring array in which each ring is threaded by

a magnetic flux ϕ, the polarization pattern changes from unpolarized to ferroelectric at half-integer flux quantum. Fig.(5.20) shows the behavior of P_x , the component of the total polarization vector $\vec{P} = \sum_i \int_0^{2\pi} d\theta |\psi_i(\theta)|^2 \vec{r}_i(\theta)$ in the direction of the ring's common axis at half flux quantum. This plot shows that at $\delta < \delta_c$ the wave function has an unbalanced distribution around each ring. However the total polarization vanishes at higher values of interaction where the wavefunction distribution becomes antiferroelectrially polarized in the array. The finite polarization at small interaction strengthes has a ferroelectric pattern which is degenerate left or right. From this result we can see that the physics of quantum ring arrays changes at half integer flux quantum. The total staggered polarization in the $\hat{y}$ direction perpendicular to the common axis of the rings starts to build up at $\delta > \delta_c$ as in the case of no magnetic field. We can explain this phenomena of *finite transverse polarization due to magnetic field* in different approaches. We can use a simple perturbative discussion to understand this behavior qualitatively. The Eq.(5.30) which is the dipole approximation of the total Hamiltonian will modify in presence of a magnetic flux as follows:

$$\begin{aligned} \hat{H} &= \hat{H}_0 + \hat{V} \\ \hat{H}_0 &= \sum_i [(-i\frac{\partial}{\partial\theta_i} - \frac{\phi}{\phi_0})^2 + 3\delta\epsilon^2 \cos 2\theta_i] \\ \hat{V} &= -\delta\epsilon^2 \sum_i [3\cos(\theta_i + \theta_{i+1}) + \cos(\theta_i - \theta_{i+1})]. \end{aligned} \tag{5.40}$$

In the above equation the kinetic energy Hamiltonian has a degenerate ground state. For example at half filling, $\phi/\phi_0 = \frac{1}{2}$, $n = 0$ and $n = 1$ levels are degenerate unlike the case of zero magnetic field in which the ground state is unique and at $n = 0$. By adding the symmetry breaking term $\cos 2\theta$ in the zero flux the electron gains enough energy to excite to the next higher level. This excitation causes the electron to destroy any localization in the range where $\hat{V}$ is not strong enough yet. However when there is a finite magnetic field the $\cos 2\theta$ can not lift the degeneracy between $n = 0$ and $n = 1$ levels in the range of small δ's. That is why in this case the ground state of $\hat{H}_0$ remains degenerate(Fig.5.18). As long as δ is small the perturbative two body potential in (5.40) can not excite the electron to higher levels and the kinetic energy of the electron freezes. When this happens the electrons behave classicaly and choose a wavefunction that minimizes the potential $\hat{V}$. In Fig.(5.19) we can see a 3D plot of the two body potential V in which it has two stable minima at (π, π)

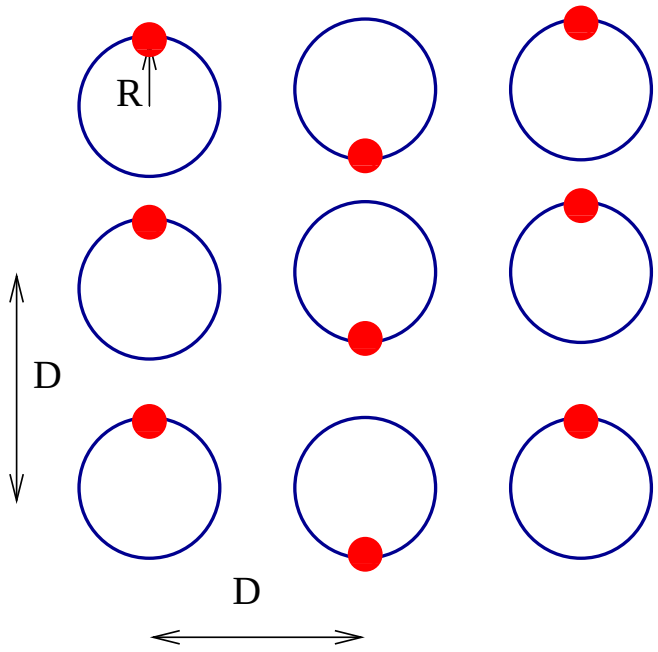

Figure 5.21: Schematic picture of the ground state of a 2D array of singly charged rings.

and $(0,0)$ indicating the preferred state of the quantum ring array at low δ being the ferreoelectric right or left state.

5.10 Two Dimensional Array

The fabricated structures of nanorings are mostly two dimensional arrays. From the analysis of the one dimensional array in the previous sections we can expect the ground state of the two dimensional array to have some sort of antiferroelectric order and indeed the results of numerical Hartree calculations for a square lattice shows that the order of the ground state is of the type of *striped antiferroelectric*, in which electrostatic polarization of rings in each column is aligned while the adjacent columns have opposite polarization. (Fig.5.21) In order to display the striped antiferroelctric order we define staggered polarization in the following way:

$$P_s = \frac{1}{N}\sum_{i,j}(-1)^i P_{ij} \tag{5.41}$$

In which P_{ij} is the polarization of the ring at the site (i,j) and N is the number of rings. In the calculations we used periodic boundary conditions and as before we have ignored the effect of inter-ring charge transfer. In fig.(5.22) we can see that the same behavior as the one dimensional array exists.

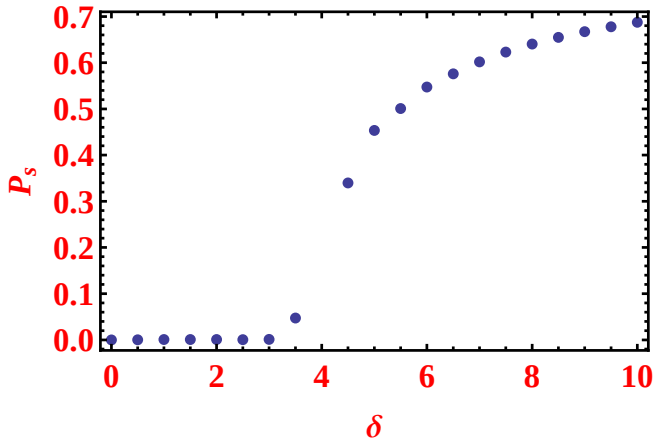

Figure 5.22: Staggered polarization as a function of δ in a 2D quantum ring square array obtained in the Hartree approximation. The numerical results are for the case include Fourier modes $|m| \leq 6$.

The obtained ground state of the 2D array is four-fold degenerate (the states obtained by flipping every spin and or rotating them all by $\pi/2$ yield the same energy) and the U(1) symmetry of unpolarized state has been broken.

In this chapter we reviewed phase transition phenomenon in a periodic array of electrons each confined to a 1D ring. The parameter δ determines if the array will spontaneously polarize; in 1D the transition is at $\delta \approx 10$. It is easy to achieve small values of δ simply by choosing the ring separation to be large. Thus the "quantum" limit where the kinetic energy dominates is simple to obtain. To obtain the antiferroelectrically ordered state we need large δ. We may write this as $\delta = (R^2/a_0 D) \times (m^*/m)$ where a_0 is the Bohr radius and m^* is the effective mass of the electron. If $\tilde{R}$ and $\tilde{D}$ are R and D measured in nanometers, and $\tilde{m} \equiv (m^*/m)$, then $\delta \approx 18.9(\tilde{R}^2/\tilde{D})\tilde{m}$. We require that the rings do not intersect, so that $\tilde{D} \geq 2\tilde{R}$. Thus the ability to achieve large values of δ in semiconductors will depend upon the value of the effective mass. If we set $\tilde{D} = 2\tilde{R}$, then for GaAs ($\tilde{m} = 0.06$) 1D arrays of rings with a radius greater than ~10nm will be polarized. For AlAs ($\tilde{m} = 0.4$) the crossover radius is about 70nm. Rings with a smaller radius will not spontaneously polarize, but instead be isotropic It is well known that in 1D there is no ordered state for $T > 0$ for the Ising model. However, for small arrays over finite time intervals the system can order. To observe this behavior we want the characteristic energies of the system to be greater than the temperature. For the Coulomb energy $kT < e^2/D$, which we may write as $\tilde{D}T < 1.8 \times 10^3$ where T is in Kelvin. For the kinetic energy this means $kT < \hbar/2m^*R^2$; if we measure $(m/m^*)\tilde{R}^2 T > 40$ in the

same units. For GaAs we can choose R to be about 14nm at 4K; choosing materials with a smaller effective mass or going to lower temperature allows us to increase the radius. A AFE polarized ring array will scatter light at a wavelength commensurate with the inter-ring separation, D. In 1D there is a gap $\sqrt{2}\omega_0$, which we may write as $2\sqrt{2\tilde{m}}(a_0/D)^{3/2}$. For GaAs rings with a separation $D = 1000$nm this gives $\omega \sim 6.0 \times 10^{10}$Hz. The 2D arrays have a similar sized gap at zone center, but the gap vanishes at one zone edge. The excitation spectrum can be probed optically, but scattering at the edge of the zone is difficult due to the constraints imposed by conservation of energy and momentum. Typically in such cases Raman scattering can be used to investigate the excitations. The 2D classical problem obviously has a finite temperature phase transition, as shown by our Monte Carlo simulations. The 2D quantum problem can be mapped on to the 3D XY model, which is known to order. Finally these calculations assume that each ring is singly occupied. This might be obtained by fabricating the rings upon a thin insulating layer covering a gate. By tuning the gate voltage we can bias the system so that it is energetically favorable for an electron to tunnel to the rings. The gate will also serve to cutoff long distance interactions between the rings, supporting the assumption of the nearest neighbor interactions used here. Moreover, this work serves to start investigation into a broad class of problems, such as rings occupied by an optically excited exciton/hole pair or perhaps by a small, varying number of electrons created by a random distribution of dopants.

The topic of quantum dot arrays and their correlations has obvious and useful analogies with solid state models of crystalline arrays of atoms. In this work we wish to point out that experimentalists have at their disposal a host of "unnatural atoms" analogs: rings, quantum dot quantum wells, quantum rice, etc. The electrons in these nanoscale constituents are confined to orbitals that may not have atomic analogs. Morever, it may be possible to tune the shape of the constituent to optimize some desired collective property such as frustration in electric or magnetic polarization, high susceptibility or sensitivity to optical polarization of light. Even more rich behavior will develop if we allow electrons to tunnel between these nanoscale periodic structures.

Chapter 6

Conclusion

In this conclusion I will summarize the above work, emphasizing what results are my own contribution to the field. I will also discuss possible future directions for this research.

6.1 Spin in bilayer quantum Hall systems

At total filling factor $\nu_T = 1$ the electron gas in bilayer system displays quantized Hall conductance. The Coulomb interaction in this electron gas has nonperturbative consequences as the kinetic energy of electrons at low temperatures is frozen out. In a quantum mechanical picture the electrons in this system can be in both layers at the same time or reside only in one. It is now a well established[27] fact that this new ground state can explain the quantization of Hall conductivity in bilayer system. In this new ground state the electrons have a new degree of freedom, the layer index or pseudo-spin. An electron in the upper(lower) layer has pseudo-spin up(down) or $+z(-z)$. Consequently the state in which each electron wavefunction is finite in both layers is a linear combination of the up and down states. At equal layer densities the pseudo-spin of electrons is a symmetric combination of up and down which corresponds to pseudo-spin in the perpendicular direction ($\pm x$).

By tuning the density above the $\nu_T = 1$ the extra electrons have to flip their pseudo-spin which costs exchange energy. This exchange energy however is minimized in a new many body state in which electrons smoothly change their pseudo-spin from the flipped direction (the minority direction) into the ground state direction (the majority direction). An illustration of this new excited state can be seen in figure 3.14. These excitations are of pseudo-spin nature and are called bimerons. The unusual physics of electrons confined in the lowest Landau level dictates the electron gas

charge density to change as the pseudo-spin distribution changes (see section 2.2.2). The bimeron pseudo-spin distribution has an associated localized charge density equal to one electronic charge. In fact as I argued in section 2.2.4 a topological charge is directly associated with an electrostatic charge for the electron gas confined in the lowest Landau level.

To minimize their Coulomb interaction a finite density of bimerons prefer to form a square lattice. In this dissertation using the Green's function equation of motion and Hartree-Fock approximation I was able to calculate the pseudo-spin and charge distribution of a state of bimeron lattice. At higher densities ($\nu_T > 1.02$) each bimeron prefers to split into two merons. Consequently at high densities the bimeron lattice rearranges into a meron-meron lattice. By calculating the energy of meron-meron lattice and bimeron lattice per electron separately I showed (fig. 3.15) for the first time that this is in fact true and the meron-meron lattice has the lower energy for square lattices.

Due to the fact that most of the experiments performed on bilayer systems use very low tunneling samples [50] it is generally believed that the lowest energy bilayer excitations are of pseudo-spin nature. The spin excitations are expected to be frozen because of the high Zeeman and exchange coupling. However this is not certain because of the nonperturbative nature of the quantum Hall liquid. In fact nuclear magnetic relaxation time measurements reveal a behavior similar to the results for single layers (compare figures 3.17 and 2.11). In this dissertation I was able to show that new types of topological excitations exists in which both spin and pseudo-spin are involved. These excitations, called CP3 skyrmions, are charged and form a lattice. Similar to skyrmion lattice states, the CP3 skyrmion lattice state support low energy Goldstone modes of spin waves which can couple to nuclear spin and change the NMR relaxation time. To calculate the charge, spin and pseudo-spin density of the new states I used the same numerical method of Green's function equation motion as in the previous works[24] and used the Hartree-Fock approximation.

For the first time I have been able to show that the CP3 skyrmion lattice is a vortex-antivortex lattice of spin and pseudo-spin which has the lowest energy among other types of bilayer excitations mostly at large layer separations ($d \sim \ell$) and small tunneling values. The combined spin, pseudo-spin state of the bilayer system has five adjustable variables: total filling factor, interlayer bias, tunneling amplitudes, Zeeman coupling and layer separation. Finally the five dimensional phase space of this system at zero temperature is not yet fully explored. In this dissertation I was

able to show that at large layer separations, small tunneling values ($\Delta_{SAS} < \Delta_Z$) and $\nu_T < 1$ the CP3 skyrmions exist as lowest energy excited state. At some other parts of the phase space I was able to show that there are other types of spin and pseudo-spin states: At $\nu_T > 1$ and large tunneling amplitudes, $\Delta_{SAS} > \Delta_Z$, spin and pseudo-spin states form a vortex-antivortex lattice I call the HCP3 state. This state has the lowest energy compared to other excited states. In this regime increasing the tunneling energy drives the system to select a state that has only spin texture and no pseudo-spin texture. However, this state is formed in the symmetric band (i.e. a linear superposition of the upper and lower layer states). This *symmetric skyrmion* state is a lattice of skyrmions in which the pseudo-spin of the electrons are all parallel.

In a CP3 skyrmion lattice the spin and pseudo-spin of electrons are entangled. This property is demonstrated in figure 3.29. The pseudo-spin of an electron determines the probability distribution of electrons in each layer. The inter-layer bias will change this distribution and consequently it changes the pseudo-spin distribution of the electron gas. At the same time, because of the entanglement of pseudo-spin and spin, the spin distribution of the electrons changes. This change in the spin distribution may affect the NMR time of the bilayer systems. This manipulation of the spin distribution of the electron gas in a bilayer system via an inter-layer bias is a unique feature of the new CP3 skyrmion lattice presented in this dissertation.

Future work in this area will include a thorough mapping of the five dimensional phase space and determining the nature of the transitions between the phases. Also as was mentioned, no CP3 skyrmion square lattice solution at zero tunneling was observed at filling factors $\nu_T > 1$. Since there are four spin and pseudo-spin single particle levels no particle-hole symmetry exists. Consequently absence of the CP3 skyrmion square lattice at $\nu_T > 1$ is not unexpected. However one needs to investigate possibilities of existence of such phase at $\nu_T > 1$. These possibilities include different lattice structure (e.g. triangular) and also a more flexible numerical method e.g. a method that includes very small temperature fluctuations in order for a better estimation of chemical potential (Eq. 3.54). Finally the numerical method used here can be useful in finding nonlinear solutions to many other low dimensional manybody systems like Graphine[73], quantum dot and quantum ring arrays, etc. This method specifically is able to find those topological states that are highly nonlinear and often very important in analyzing the observed properties of these systems.

6.2 Activated dissipation in bilayer quantum Hall systems

Activation energies are determined by longitudinal resistance measurements performed separately in each layer of the bilayer system. These activation energies must correspond to quasi-particles excited by temperature. However measurements indicated that the behavior of the activation energies is different for different layers as one changes the inter-layer bias. This is in clear contrast with the well established coherence interpretation of quantum gas as explained in chapter three. In this dissertation I have shown that the quasiparticles responsible for dissipation are in fact merons, topological excitations of the coherent bilayer system. Following the ideas in previous works by Fertig and Murthy [59] I assume that the disorder potential breaks up the $\nu_T = 1$ incompressible quantum liquid into equal number of puddles with $\nu_T > 1$ and $\nu_T < 1$. Each puddle is full of bimerons as lowest excited states. This disorder structure breaks the bimerons into merons and merons can move across the system.

However this motion is activated as each meron needs to cross a barrier of incompressible state in between puddles. Using the fact that merons have vorticity, charge and electric dipole moment and using a Chern-Simon theory I showed that their motion induces a voltage drop across the system. This voltage drop is induced through Faraday's law as merons are charged and carry a Chern-Simon flux and also through their vorticity in analogy to Josephson effect. I modeled the barriers as strip shaped interlayer biases imposed over meron lattices. Using this technique I was able to calculate the activation energies and show that their behavior is consistent with experiment as I vary the interlayer bias strength.

In the future I hope that experiments can verify the predictions of my theory. The presented theory is a new approach in analyzing the transport properties of the bilayer systems. This theory can be developed in so many different ways. The possible role of low but non-zero tunneling amplitude in activation energy of merons can be investigated using for example parallel magnetic field. As was discussed in chapter (3) in a sample with non-zero tunneling bimerons are lower in energy than merons. Bimerons on the other hand do not have an electric dipole moment and consequently they don't respond to the interlayer bias. This results in the disappearing of the asymmetric behavior in the activation barrier. It would also be interesting to know the response of a bimeron to a strip bias potential. Does the bimeron prefer to split

into two separate merons? This may illustrate why disorder can unbind merons. This response can be studied by varying interlayer bias, tunneling and separation. In addition we have assumed that the Zeeman energy is large enough so that the spin of the electrons are polarized. First of all one needs to find out what would be the response of the meron to strip potential when the Zeeman gap is low such that it allow the spin of electrons tilt away from majority direction in order to compensate for energy cost of the bias strip. On the other hand CP3 skyrmions are robust against interlayer bias as was illustrated in the previous chapter. The question then remains whether they are robust against the application of strip biases and how will their energy change. All these questions can be answered by extending this numerical work and also by studying a possible spin-pseudospin Chern-Simon theory for a bilayer system. These questions also may in principle be studied by experiments.

In addition the Chern-Simon theory and the meron-edge interaction theory must be united. The Chern-Simon theory neglects edges entirely and only assumes a balanced meron population. However this can only be true for a finite system if we allow for charge conversion as given in figure (4.16). Conversely, the edge picture does not predict the mobilities and transition rates implicit in eq.(4.38). These must be generated by a microscopic theory such as the Chern-Simon approach.

Finally it is worth exploring if the correlated behavior that lead to excitonic superfluidity can be pushed to higher temperatures for example by using different host material such as graphene [73]. While this may seem absurd, high T_c superconductivity was also absurd twenty years ago.

6.3 Nano-ring arrays

In the last chapter of this work I introduced a model of interacting ring arrays in order to illustrate the idea that confined geometry can give physicists a new path for creating new ideas to advance technology using nano-structures. In the model of interacting quantum rings arrays each ring in a square lattice is free to move on a one dimensional array but interacts with the electrons in its neighboring rings. The ground state energy and wave function of these electrons were calculated using an iterative Hartree approximation. I was able to show that these wave functions suddenly change from uniform distribution around the ring to localized state as one reduces the inter-ring separation. This localized state is distributed anti-ferroelectrically throughout the array. Using a Monte-Carlo simulation I also showed that this transition is a true

second order phase transition for the two dimensional array and a true quantum phase transition for the one dimensional array. In this simulation I showed that the observables of the system like the specific heat and polarization diverge as the system size diverges at the transition point. Then using a finite size scaling theory I showed that this transition is in the universal class of transverse field Ising model.

I also calculated the polarization of the one dimensional array in the presence of an external magnetic field. I showed that the external magnetic field threading each ring will change the polarization of the system from anti-ferroelectric to ferroelectric for large inter-ring separations through the induced Aharanov-Bohm phase.

Future work will include looking at 3D arrays of rings and 2D and 3D arrays of spherical shells. In addition it would be good to calculate the optical excitation spectrum of such arrays.

The collective excitations of these arrays will be another important part of analyzing these systems. The wave function distribution of these excitations can be of topological nature similar to the spin distribution in skyrmions or domain walls in spin lattices as the electrons try to minimize their Coulomb energy in a finite system. The numerical methods of finding these kinds of excitations in bilayer quantum Hall calculations may be useful in this context.

Bibliography

[1] *Modern Theory of Critical Phenomena*, Shang-Keng Ma (Westview Press, 2000).

[2] *The Physics of Semiconductors*, Marius Grundmann (Springer-Verlag, 2006).

[3] *Quantum Wells, Wires and Dots : Theoretical and Computational Physics of Semiconductor Nanostructures*, Paul Harrison (John Wiley and Sons, New York, 2005).

[4] M. Büttiker, Y. Imry and R. Landauer, Phys. Lett. A, **96**,365 (1983).

[5] R. Landauer and M. Büttiker, Phys. Rev. Lett., **54**,2049(1985).

[6] L. P. Levy et. al., Phys. Rev. Lett., **64**, 2074 (1990), V. Chandrasekhar et. al., phys. Rev. Lett., **67**, 3578(1991).

[7] Tarucha et. al., PRL **77**, 3613 (1996).

[8] B. Roostaei, K.J. Mullen, cond-mat/0605068, to be published in Phys. Rev. B.

[9] K. Binder, *Z. Phys.* B **43**, 119 (1981).

[10] J. J. Sakurai, *Modern Quantum Mechanics*, (Addison-Wesley Publishing Company, Inc. 1994).

[11] Subir Sachdev, *Quantum phase transition*, (Cambridge University Press 1999).

[12] M. Wallin, E. Sørensen, S.M. Girvin, and A.P. Young, *Phys. Rev.* B **49**, 12 115 (1994).

[13] 11] J. Villain, *J. Phys.* **36**, 581 (1975).

[14] Assa Auerbach, *Interacting electrons and quantum magnetism*, (Springer-Verlag New York, Inc. 1994).

[15] C.L. Kaneand M.P.A. Fisher, *Phys. Rev.* B **46**, 7268 (1992); *op. cit.* 15233 (1992); *Phys. Rev.* B **51**, 13449 (1995) C.L. Kane, M.P.A. Fisher and J. Polchinksi, *Phys. Rev. Lett.* **72**, 4129 (1994).

[16] M. Büttiker, *Phys. Rev.* B **38**, 9378 (1998).

[17] B. I. Halperin, *Helv. Phys. Acta* **56**, 75 (1983).

[18] *Perspectives in Quantum Hall Effects*, Edited by Sankar Das Sarma and Aron Pinczuk (Wiley, New York, 1997).

[19] T. Chakraborty and P. Pietiläinen, *The Fractional Quantum Hall Effect*, (Springer-Verlag, Berlin, New York, 1997).

[20] S.L. Sondhi, A. Karlhede, S.A. Kivelson, and E.H. Rezayi, *Phys. Rev.* B **47**, 16419 (1993).

[21] S.M. Girvin, T. Jach, *Phys. Rev.* B **29**, 5617 (1984).

[22] S. M. Girvin, *The Quantum Hall Effect: Novel Excitations and Broken Symmetries*, Les Houches, Springer Verlag, Edition 1999.

[23] A. Pinczuk, B. S. Dennis, L. N. Pfeiffer, and K.W. West, *Phys. Rev. Lett.* **70**, 3983 (1993).

[24] H. A. Fertig, L. Brey, R. Còte, A.H.MacDonald, *Phys. Rev.* B **50**, 11018 (1994).

[25] R. Rajaraman, *Solitons and Instantons* (North Holland, Amsterdam), 1982.

[26] See for example, D. Yoshioka, A.H. MacDonald, and S.M. Girvin, *Phys. Rev.* B **38**, 3636 (1988).

[27] K. Moon, *et. al.*, *Phys. Rev.* B **51**, 5138 (1995) and references therein.

[28] S.E. Barret, G. Dabbagh, L. N. Pfeiffer, K.W. West, and R. Tycko, *Phys. Rev. Lett.***74**, 5112 (1995).

[29] K. Yang, *et. al.*, *Phys. Rev.* B **54**, 11644 (1996).

[30] R. Tycko, S.E. Barret, G. Dabbagh, L. N. Pfeiffer and K.W. West *Science***268**, 1460 (1995).

[31] C.P. Slichter, *Principles of magnetic resonance*, 3rd Ed. (Springer-Verlag, Berlin, New York, 1990).

[32] A. Schmeller, J. P. Eisenstein, L. N. Pfeiffer, K.W. West, *Phys. Rev. Lett.***75**, 4290 (1995).

[33] E. H. Aifer, B. B. Goldberg, and D. A. Broido, *Phys. Rev. Lett.* **76**, 680 (1996); M. J. Manfra, E. H. Aifer, B. B. Goldberg, D. A. Broido, L. Pfeiffer, and K. W. West, *Phys. Rev.* B **54**, R17327 (1996).

[34] D. K. Maude, et al., *Phys. Rev. Lett.* **77**, 4604 (1996); D. R. Leadley, *et. al.*, *Phys. Rev. Lett.* **79**, 4246 (1997).

[35] Dimitri Antoniou and A. H. MacDonald, *Phys. Rev.* B **43**, 11686 (1991).

[36] A. H. MacDonald, H. A. Fertig and Luis Brey, *Phys. Rev. Lett.* **76**, 2153(1996).

[37] H. A. Fertig, *Phys. Rev.*B **40**,1087 (1989).

[38] R. Cote, A. H. MacDonald, Luis Brey, H. A. Fertig, S. M. Girvin, and H. T. C. Stoof, *Phys. Rev. Lett.* **78**, 4825 (1997).

[39] A. E. Rana and S. M. Girvin, *Phys. Rev.* B **48**, 360 (1993).

[40] cond-mat/0403512v1.

[41] R. Ct, D. B. Boisvert, J. Bourassa, M. Boissonneault, and H. A. Fertig, *Phys. Rev.* B **76**, 125320 (2007).

[42] R. M. White, *Quantum Theory of Magnetism* (Springer-Verlag, New York, 1970).

[43] S. Q. Murphy, *et. al.*, *Phys. Rev.* B **52** 14825 (1995).

[44] J.P. Eisenstein, L.N. Pfeiffer and K.W. West, *Appl. Phys. Lett.* **57**, 2324 (1990).

[45] L. Zhang, A. H. MacDonald, *Phys. Rev.* B **47**, 10619 (1993).

[46] J.P. Eisenstein, L. N. Pfeiffer and K. W. West, *Phys. Rev. Lett.* **74**, 1419(1995).

[47] S. Q. Murphy, J. P. Eisenstein, G. S. Boebinger, L. N. Pfeiffer and K. W. West, *Phys. Rev. Lett.* **72**, 728 (1994).

[48] L. Brey, H. A. Fertig, R. Cote and A. H. MacDonald, *Phys. Rev. Lett.***75**, 2562 (1995).

[49] I. B. Spielman, J. P. Eisenstein, L. N. Pfeiffer and K.W. West,*Phys. Rev. Lett.* **84**, 5808 (2000).

[50] I. B. Spielman, L. A. Tracy, J. P. Eisenstein, L. N. Pfeiffer, and K. W. West ,*Phys. Rev. Lett.* **94**, 076803 (2005).

[51] H. L. Störmer, *Physica* B **177**, 401(1992).

[52] S. Ghosh, R. Rajaraman, *Phys. Rev.* B **63**, 035304 (2000).

[53] M. Kellogg, J. P. Eisenstein, L. N. Pfeiffer, and K.W.West, *Phys. Rev. Lett.* **93**, 036801 (2004).

[54] B. D. Josephson, *Rev. Mod. Phys.* **46**, 251 (1974).

[55] M. Kellogg, I. Spielman, J. P. Eisenstein, L. N. Pfeiffer, and K.W.West, *Phys. Rev. Lett.* **88**, 126804 (2002).

[56] R. D. Wiersma, *et. al.*, *Phys. Rev. Lett.* **93**, 266805 (2004).

[57] L. Balents and L. Radzihovsky, *Phys. Rev. Lett.* **86**, 1825 (2001).

[58] A. Stern, S. M. Girvin, A. H. MacDonald, and Ning Ma, *Phys. Rev. Lett.***86**, 1829 (2001).

[59] H. A. Fertig, Ganpathy Murthy, *Phys. Rev. Lett.* **95**, 156802 (2005).

[60] H. A. Fertig and J. P. Straley, *Phys. Rev. Lett.***91**, 046806 (2003).

[61] Z. Wang, *Phys. Rev. Lett.* **92**, 136803 (2004).

[62] D. Sheng, L. Balents, and Z. Wang, *Phys. Rev. Lett.* **91**, 116802 (2003).

[63] D.H. Lee and C.L. Kane, *Phys. Rev. Lett.* **64**, 1313 (1990).

[64] M. Stone, *Phys. Rev.* B **24**, 16573 (1996).

[65] D. L. Huber, *Phys. Rev.* B 26, 3758 (1982); P.L. Christiansen *et. al.*, *Nonlinear Scienc at the Dawn of the 21st Century*, (Springer-Verlag, NY, 2000).

[66] Enrico Rossi, Alvaro S. Nunez, and A. H. MacDonald, *Phys. Rev. Lett.* 95, 266804 (2005).

[67] A. J. Leggett, *Quantum Liquids* (Oxford, New York, 2006).

[68] R. D. Wiersma, PhD dissertation (2006).

[69] Y. Joglekar, and A. H. MacDonald, *Phys. Rev. Lett.* 87, 196802 (2001).

[70] A. Efrös, *Solid State Commun.* **65**, 1281 (1988).

[71] A. Efrös, F. Pikus, and V. Burnett, *Phys. Rev. B***47**, 2233 (1993).

[72] N. Nagaosa, *Quantum Field Theory in Condensed Matter Physics*, (Springer, Berlin Heidelberg 1999).

[73] Y. Zhang, Y. W. Tan, H. L. Stormer, P Kim. *Nature* **438**, 201 (2005).

[74] P. Nozières, D. Pines, *Theory of quantum liquids* (Perseus Books Publishing, 1999).